Universidad de la República
Facultad de Ciencias

Incoherent Optical Image Processing with the Generalized Hough Transform

MSc. Ariel Fernández

Tesis presentada para completar los requerimientos del grado de Doctor en Física

Orientador: Dr. José Ferrari

defendida el 4 de noviembre de 2016 ante el tribunal integrado por:

presidente: Dr. Carlos Negreira, *Instituto de Física, FCien, UdelaR*
Dr. Gonzalo Abal, *Dpto. de Física, CENUR Litoral Norte, UdelaR*
Prof. Ing. Alicia Fernández, *Inst. de Ing. Eléctrica, FIng, UdelaR*
Dra. Silvia Ledesma, *Departamento de Física, FCEyN, UBA*
Dr. José Ferrari, *Instituto de Física, FIng, UdelaR*

Acknowledgments

I would first like to thank my thesis advisor Dr. José Ferrari. He introduced me to the fascinating discipline of Optics and allowed me to explore it and implement my own ideas.

I would also like to thank the members of the doctoral committee, who kindly accepted to revise this manuscript: Dr. Carlos Negreira, Dr. Gonzalo Abal, Prof. Ing. Alicia Fernández and Dra. Silvia Ledesma.

This thesis would not have been possible without the support of many people. I specially thank Dr. Jorge Flores for all his dedication in trying to make the experiments of my thesis work.

I would also like to thank my colleagues from the Applied Optics Group who have shared very interesting comments regarding this work.

My colleagues from the Physics Institute have also supported me in the course of this thesis. I specially thank Amelia, Liber, Antonio and Joaquín for their continuous help in everyday work.

Gala, my family and friends have helped me in keeping my feet on the ground, and I would like to thank them for that.

And finally I would like to thank my loving wife and best friend Julia for her intelligence, support and encouragement.

Abstract

The generalized Hough transform (GHT) is a well-established technique for detecting complex shapes in images containing noisy or missing data. Detection of a geometric feature under the GHT is digitally accomplished by mapping the original image to an accumulator space (Hough space); the large computational requirements for this mapping make the optical implementation an attractive alternative to digital-only methods. In general, the attractiveness of optical processors for image processing applications (e.g. pattern recognition, feature extraction) lies in their highly parallel operation and real-time processing capability. However, few approaches have been proposed for the optical implementation of the GHT and all of them working under coherent illumination, even when it is well known that incoherent processors are not sensitive to the phase variations in the input plane and also exhibit no speckle noise.

Starting from the integral representation of the GHT, we propose a correlator based on the point-spread function of a highly blurred optical system in which the focal setting along with the orientation of the pupil can be efficiently controlled. This correlator works under fully (i.e., both spatially and temporally) incoherent illumination and can handle orientation changes or scale variations in the pattern. Real-time operation (as limited by the frame rate of the device used to capture the GHT) is achieved, allowing -besides static images- for the processing of video sequences. Based in the previous system, we implement temporal multiplexing strategies for pattern recognition of geometrical features of different size and orientation. Besides, given the inherently convolutional nature of our system, we are able to simultaneously detect the same target at multiple locations. The robustness of our method against noise in the input, low contrast, or overlapping of geometrical features is also assessed. Finallly, through the nonlinear filtering of the GHT and subsequent inversion (which is optically achieved in the incoherent system under appropriate focusing setting), the previously detected features of interest can be segmented.

Keywords: *Hough transform, Optical image processing, Pattern recognition, Image segmentation*

Resumen

La transformada de Hough generalizada (GHT) es una técnica bien establecida para la detección de formas complejas en imágenes conteniendo información ruidosa o incompleta. La detección de una característica geométrica usando la GHT se consigue digitalmente mediante el mapeo de la imagen original a un espacio de acumulación; los grandes requerimientos computacionales para conseguir este mapeo hacen de la implementación óptica una atractiva alternativa a los métodos sólo digitales. En general, el atractivo de los procesadores ópticos para aplicaciones de procesamiento de imágenes (por ejemplo, reconocimiento de patrones, extracción de características) radica en su operación altamente en paralelo y su capacidad de procesamiento a tiempo real. Sin embargo, pocos acercamientos han sido propuestos para la implementación óptica de la GHT y todos trabajando bajo iluminación coherente, aún cuando es bien sabido que los procesadores incoherentes son insensibles a las variaciones de fase en el plano de entrada y no exhiben ruido de speckle.

A partir de la representación integral de la GHT proponemos un correlador incoherente basado en la respuesta al impulso de un sistema óptico fuertemente desenfocado, donde el ajuste focal así como la orientación de la pupila se pueden controlar eficientemente. Este correlador trabaja con iluminación completamente (es decir, tanto espacialmente como temporalmente) incoherente y puede tratar con cambios de orientación o variaciones de escala del patrón. Se logra además procesamiento a tiempo real (limitado por velocidad del dispositivo de captura de la GHT), lo que permite -además de imágenes estáticas- el procesamiento de secuencias de video. En base al sistema anterior implementamos estrategias de multiplexado temporal para el reconocimiento de características geométricas de diferente tamaño y orientación. Además, dada la naturaleza inherentemente convolutiva de nuestro sistema, podemos detectar simultáneamente el mismo objetivo en múltiples posiciones. La robustez del método frente a ruido en la entrada, bajo contraste o solapamiento de las características geométricas también es evaluada. Finalmente, a través del filtrado no lineal de la GHT y subsiguiente inversión (que se logra ópticamente en el sistema incoherente con un adecuado ajuste de foco), las características previamente detectadas pueden ser segmentadas.

Palabras clave: *transformada de Hough, Procesamiento óptico de imágenes, Reconocimiento de patrones, Segmentación de imágenes*

Index

Figure Index

Introduction

In comparison to purely digital methods, the attractiveness of optical processors for image processing tasks like edge enhancement, pattern recognition or feature extraction lies in their highly parallel operation and real-time processing capability.

In recent decades, the Hough transform (HT) has been established as an efficient pattern recognition technique that works well even in images with disconnected boundaries, noise, or occlusions. Initially proposed for the detection of lines in binary images (linear HT or LHT) [Hough, 1962], then extended to other simple parametric curves like circles or ellipses, and finally generalized to an arbitrary nonparametric feature (generalized HT or GHT) [Ballard, 1981], the HT has been successfully applied in object or motion detection, biometric authentication, medical imaging, remote data processing, and robot navigation among others.

The principal drawback for a standard HT or GHT-based shape recognition algorithm is its large computational requirements [van den Braak et al., 2011, Ujaldón et al., 2008], which makes its real-time implementation difficult even under dedicated architectures [Zhou et al., 2014].

In order to achieve real-time processing, optically based algorithmic architectures for the HT [Steier and Shori, 1986, Ambs et al., 1986] have been proposed, mostly working under coherent illumination. With the capability of achieving signals with less noise, the use of incoherent illumination was also suggested for the HT [Steier and Shori, 1986, Schmid et al., 1998].

For the optical implementation of the GHT, few approaches can be found in the literature and all working under coherent illumination. The use of lasers acousto-optically modulated and the piece-wise representation of the template through analytical curves was proposed in [Casasent and Richards, 1993]. The use of a matrix of holograms was proposed in [Shin and Jang, 2000] and the scale and rotation-variant detection were accomplished by spatial multiplexing. However, the implementation of the GHT under incoherent illumination had not been proposed, even when it is well known that incoherent processors have the advantage of not being sensitive to the phase variations in the input plane and also exhibit no speckle noise.

In the course of our work we try to answer the following questions concerning an optical implementation of the generalized Hough transform:

1. Which would be a suitable optical system for the implementation of the transform under incoherent illumination
2. The multiplexing strategies which may allow for the detection under variable scale or orientation
3. The feasibility of optical schemes for feature extraction

To address the first item above mentioned (Item 1) we propose an incoherent correlator [Fernández et al., 2015a] based on the point-spread function of a highly blurred optical system, in which the focal setting along with the orientation of the pupil can be efficiently controlled. We also prove the real-time capability of our system by means of the processing of video sequences. With the previous system as a starting point, we implement temporal multiplexing strategies (Item 2) for pattern recognition of geometrical features of different size and orientation [Fernández et al., 2015b]. Besides, given the convolution nature of our system, we are able to implement multiple target detection out of static images as well as video sequences. For the extraction of a given feature (Item 3) after detection, we also propose the nonlinear filtering of the GHT [Fernández et al., 2016].

Chapter 1 of this thesis is dedicated to a brief review of the optical processing of images in comparison to digital counterparts. Special attention is devoted to two particular tasks directly related to the rest of the work: (i) edge-enhancement, which is a common preprocessing stage that can be efficiently achieved by optical means and (ii) pattern recognition, where optics has played a key role and where Hough transform has proven to be efficient for geometric features. In Chapter 2 the HT and other transformations related to analytical features (e.g. circles and ellipses) are introduced along with a review on the optical approaches to these transformations. We also consider the definition of the GHT and the coherent optical approaches to this transformation. Chapter 3 is dedicated to the GHT and its optical incoherent implementation. Starting from the integral representation of this transform, and comparing it to the response of an optical system linear in intensity, the Point Spread Function (PSF) that allows for the implementation of the GHT in the incoherent regime is introduced and the preliminary results for detection using this incoherent GHT are presented. In Chapter 4 we present the pattern recognition applications that result from improvements over the previous setup. Continuous time variation of the scale and orientation parameters of the template in the GHT allows for varying scale or orientation detection under temporal multiplexing. Aside from recognition

tasks, in Chapter 5 we introduce the theory and implementation of extraction of geometrical features from an edge image. Finally in Chapter 6 the conclusions of the work and future perspectives are presented.

Chapter 1

Optical Image Processing

Optics plays a fundamental role in the acquisition, processing and transmission of information. Acquisition by optical means is present in microscopy, medical imaging, astronomy, surveillance applications and robot vision among others, while optical fibers have enabled data transmission at higher bandwidths and more robustly than wire cables. An important field of optical image processing consists of pattern recognition, localization and tracking. These tasks were from the beginning [McLachlan Jr, 1962] a prime choice for optical processing since they fully exploit the inherent parallelism of optical systems. Preprocessing by means of edge enhancement/detection needs also to be performed in order to improve the recognition capability of an optical system and can again benefit from the capability of optics to carry out information processing simultaneously over all the image input.

In comparison to digital methods, optics can be used for special-purpose processors in the aforementioned tasks due to the advantages related to simultaneous processing as well as the possibility of operation over continuous data offer. The higher space-bandwidth product (SBP) in comparison to digital processors is another advantage, but given the increasing power of computer processing the development of optical processors along with their commercialization have been limited. As pointed out in a review by Alfalou and Brosseau [Alfalou and Brosseau, 2009], one of the main concerns with the algorithmic developments in optical processing is to compare them side by side with the interfaces needed to implement them. An optical implementation can be considered successful when it achieves real-time processing (as required in a dedicated setup) and ease in its implementation.

In the next, a brief historical review of optical image processing will be presented to afterwards focus on the preprocessing of images by edge-enhancement and in pattern recognition applications, both under coherent and incoherent light.

1.1 A bit of history

One of the milestones in the development of optical image processing can be traced back to the work of Maréchal in the early 1950s (a comprehensive review on the history of optical information processing can be found in [Ambs, 2010, Goodman, 1996]). Maréchal and collegues [Maréchal and Croce, 1953] showed that by the use of spatial filters in a coherent optical system, image enhancement (deblurring and edge enhancement for example) can be achieved. A review on spatial filtering [O'Neill, 1956] from the same decade pointed out the relative ease of optical implementation of well-known electrical signals counterparts such as edge-sharpening and equalization. By that time, however, the idea was not completely new. The control of Fourier spectra of an image underlies Zernike's phase contrast technique for microscopy (1935) [Johnson, 2012] where the observed intensity is linearly related to the phase shift introduced by a specimen. Even earlier, the work of Abbe (1870s) on the image formation theory in microscopy set the path for the tools to be developed in the general analysis of imaging systems.

From an applications viewpoint, a major step toward establishing optical processing as a recognized branch of optics was the use of coherent optics to process data derived from a synthetic aperture radar (SAR) [Leith, 2000] (which indeed started with an incoherent source approximation in 1953).

With the development of laser sources in the 1960s, optical information processing began a rapid expansion. Major coherent optical correlation advances were accomplished by 1970 in parallel with the development of holography. Practical real-time implementations were only limited by the development of efficient Spatial Light Modulators (SLM). In the late 1960s the first electrically addressed SLM's based in Liquid Crystal were developed and by the end of the 1970s, optically addressed SLM's were also available. Despite these advances, no real-time useful processor was developed due to the lack of efficient SLMs. At the same time, digital computers achieved enough power to compete with some optical counterparts, like SAR.

By the early 1980s, although digital computers were not powerful enough, most of the optical processors developed still remained in prototypes mainly because applications that would benefit from the speed of optics were few and also because of the absence of efficient modulators. In spite of this, several different SLM technologies were developed, among which two survived and are commercially available in display devices: LCD and Digital Micromirror Devices (DMD). During the 1980s and 1990s several optical processing devices were realized taking advantage of the progress in SLM fabrication. In particular, many attempts at commercializing optical correlators date from this period (see [Ambs, 2010] and references therein). As it will be

discussed in detail in the next chapter, several optical implementations of the Hough transform date from those years.

The perspectives for optical computing by the late 1990s [Caulfield, 1998] were not to focus in replacing what was better done electronically. Instead, efforts were aimed at concentrating on the roles electronics cannot play and joining efforts to achieve better overall performance. In fact, no all-optical processor is desirable since at least in a final capture stage, electronics will be needed. Those roles at which optics plays best are for example the implementation of massive, arbitrary mapping from an $N \times N$ input array to an $N \times N$ output array. In this regard, operations that can be put in terms of a convolution -like the generalized Hough transform in which we are interested- are expected to perform very well under optical architectures. Optics is also free of "garbage" operations (there is no storage and later deletion of intermediate information to carry out an operation) which involve time and energy resources; in fact, driving power consumption down is a major engineering concern that has led research efforts towards the control of light flow at Ghz in silicon [Lipson, 2015].

The possibility to encode information in dimensions such as phase, wavelength or polarization is another unique feature of optics which has been exploited for information encryption applications [Javidi, 2005] and hyperspectral imaging for inspection and surveillance [Coffey, 2015], among others. However, the most interesting and complex optical systems still imply a combination of optical and digital processing.

A great example can be found in the field of adaptive optics [Tyson, 2011] in which optical methods are part of a preprocessing stage for wavefront sensing and are followed by digital methods for determining appropriate changes for an adaptive mirror.

Pattern recognition has also benefit from the joint design optimization of optical and digital domains [Awwal et al., 2010], usually obtaining an improvement in overall performance in comparison to only digital or optical methods.

Another recent example of combination of optics and electronics can be found in a physics-based signal transformation known as anamorphic stretch transform [Asghari and Jalali, 2013] that enables a digitizer to capture signals that would otherwise be beyond its bandwidth and at the same time, compresses the digital data volume, alleviating the storage and transmission bottlenecks associated with the big data. Based on a discrete approximation of the equations that govern this transformation, and coupling with standard JPEG compression, 56-fold reduction in data size has been accomplished.

In the same line of thought, optics may also offer inspiration for computational developments as can be found in the implementation of virtual spiral phase filtering

on a GPU [Zhong et al., 2014] or the digital implementation of phase encryption for a Joint Transform Correlator (see Section 1.2.1.2) [Alsamman, 2010].

Although not in the "golden era" when all-optical processors were expected to overcome their computational counterparts, and even when these counterparts have proven to be efficient in a great number of tasks, room is still available for optical implementations which prove to be efficient at real-time processing and ease in implementation. Recent proposals for beam-shaping by means of layered materials [Youssefi et al., 2016, Bykov et al., 2014, Doskolovich et al., 2014] are directed towards analog all-optical processing of information. This revival in analog optical computing is not based on trying to achieve an optical counterpart of a digital machine but in creating an analog machine capable of accelerating existing electronic computers [Solli and Jalali, 2015].

The role of an optical implementation of the Generalized Hough Transform in connection with real-time capability and implementation is to be discussed in Chapter 3. To place this transform in the correct context of optical image processing we will briefly review edge-enhancement (crucial as preprocessing step) and pattern recognition tasks under coherent and incoherent illumination.

1.2 Coherent and incoherent processors

The mode of illumination on the object plane of a system greatly determines its optical properties. The inclusion of a mutual coherence factor between the points that form the illumination source allows for treating the image formation in the optical system in a completely general way. The mutual coherence factor takes into account two types of coherence of an optical wave, namely temporal and spatial coherence [Born and Wolf, 2000, Goodman, 1985].

When we talk about *temporal coherence* we are dealing with the ability of a light beam to interfere with a delayed version of itself, as a result of amplitude splitting of the beam (for example, in a Michelson interferometer). *Spatial coherence* on the other hand is related to the ability of a light beam to interfere with a spatially shifted (but not delayed) version of itself, as a result of wavefront splitting of the beam (for example, in a Young double slit experiment).

In the following sections we will deal with the extreme cases of coherence. First we will consider coherent processors where the object plane is treated as being illuminated by a monochromatic (perfectly temporally coherent) plane (perfectly spatially coherent) wave. This is an idealization that to a good extent might be met by a laser source. But, as any real source has a finite bandwidth, temporal coherence should be relaxed, even up to the extreme case of white light sources. Non-perfect spatial

coherence should also been taken into account since real sources have also a finite size and the radiating points that give rise to the source might not emit in phase. In an extreme case, Chapter 3 deals with *totally incoherent* sources, i.e. both spatially and temporally incoherent light.

1.2.1 Fourier-based processing

In this section we will briefly review the operations that can be performed in coherent optical systems where linearity in the *complex* amplitude of light (characterized by its modulus and phase) can be considered.

One of the operations that an optical processor can easily perform is the two-dimensional Fourier Transform of information incoming in the form of a complex wave. Taking advantage of the basic laws of propagation and diffraction of light, Fourier transform is achieved in the propagation between the front and back focal planes of a converging lens [Goodman, 1996, Iizuka, 2008, Stark, 2012].

Following this principle, an optical system might be formed by arranging a sequence of lenses that gives a succession of Fourier transform planes. In the early 60's Van der Lugh (see 1.2.1.2) proposed a basic Fourier processing configuration known as 4f-processor (Figure 1.1). Between planes P_1 and P_2 lens L_1 performs the Fourier transform of the input.A second lens L_2 placed behind P_2 performs another Fourier transform, so the output of the system (with no filter applied over the signal) is the inverted image of the input. Control over the Fourier components of the image is achieved by acting on the Fourier plane. This basic scheme allows to perform the most important shift-invariant operations in image processing under coherent light: filtering and pattern recognition. The *paraxial* or first order [Alieva, 2008] optical systems like the 4f-processor constitute the basic analog optical information processing tools in Fourier Optics. More sophisticated processing arises from considering propagation through graded index media instead of simple lenses in order to achieve fractional Fourier transforms [Mendlovic and Ozaktas, 1993, Ozaktas and Mendlovic, 1993] or by the implementation of wavelet transforms [Sheng et al., 1992, Mazzaferri et al., 2003] in optical correlation (Section 1.2.1.2) architectures .

Next we explore the applications that arise from operating over the frequency components of an image in the coherent regime.

1.2.1.1 Edge-enhancement with coherent light

The enhancement of edges that serve as boundaries which delimit regions of the image with different properties is one of the most important pre-processing tasks in image processing. Given that the edges correspond to jumps in the derivative of a

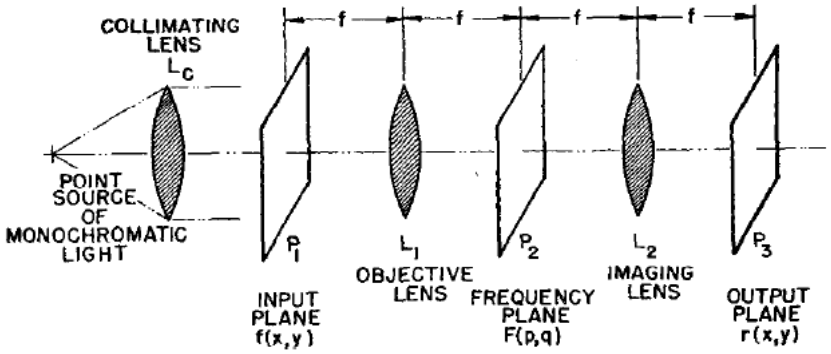

Figure 1.1: 4f coherent optical processor (from [Stark, 2012]).

certain property (intensity, color, texture) or equivalently, to zero crossings of the second derivative [Marr and Hildreth, 1980], coherent optical processing for edge-enhancement is primary oriented towards the realization of derivatives [Eguchi and Carlson, 1970]. It can be easily seen that the derivative of a signal can be obtained by multiplying the Fourier transform of the signal by $j2\pi f$, with j representing the imaginary unit and f the spatial frequency, and performing the inverse transform. In order to apply this idea on a 4f-processor we need to place a $j2\pi f$ mask in the Fourier plane of the processor. At the same time, and as it was common in the early stages of Fourier image processing, the mask is given by the product of an amplitude only and a phase only mask (Figure 1.2). A result for image differentiation through this method can be seen in the same figure.

Basic high-pass filtering of images can also be realized by means of amplitude only masks placed in the Fourier plane. In Figure 1.3 high-pass filtering is achieved by stopping the low frequency Fourier components of an image in the Fourier plane of a 4f processor, resulting in an image with omnidirectional (i.e., rotationally invariant) edge-enhancement. Similarly, in digital processing, working in the frequency space of an image is commonly used for high or low-pass filtering (i.e. edge enhancement or blurring of images), periodic noise removal, etc. [Gonzalez and Woods, 2002, Russ, 2011].

Other methods, based on a spiral filtering create a directional edge-enhanced image by the convolution of a complex function representing the sample with a vortex impulse response function of the optical system. Spiral phase plates with azimuthal structure can be used as a SLM in the Fourier plane of a 4f processor so that the output image corresponds to the convolution of the input image with a vortex PSF of the optical system. The final image corresponds to the edge-enhanced version of the input [Situ et al., 2009, Crabtree et al., 2004]. This approach to edge-enhancement

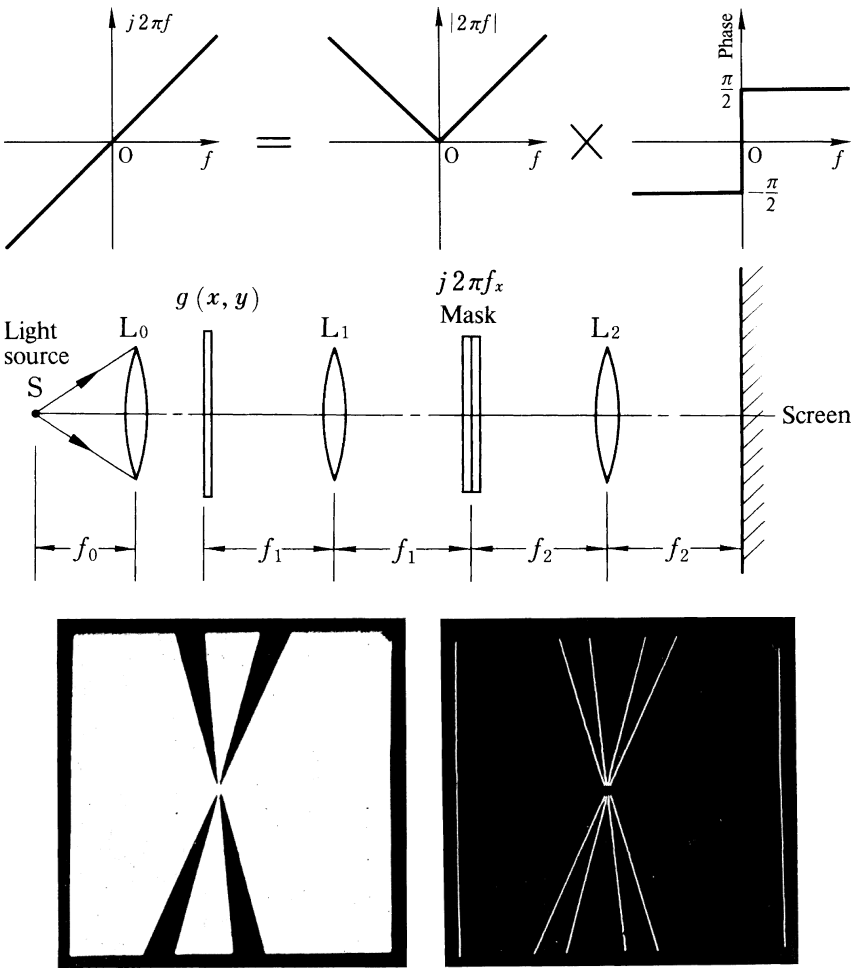

Figure 1.2: Image differentiation using coherent light (Top) Fourier mask synthesis by the product of phase only and amplitude only masks (Middle) Basic coherent setup for image differentiation (from [Iizuka, 2008]) (Bottom) Differentiation in the horizontal direction, original image (left) horizontal edge-enhanced image (right) (from [Eguchi and Carlson, 1970]).

Figure 1.3: High-pass filtering in a 4f-system at our lab. (a) original image (b) edge-enhanced image using an aperture stop at the Fourier plane

has proven to be useful in different applications in microscopy [Fürhapter et al., 2005, Jesacher et al., 2005] and it is also known as radial Hilbert transform processing [Davis et al., 2000] since the phase masks are radially symmetric. By considering a complex filter with radial dependence of the amplitude and spiral structure in the phase, the combination of a smoothing operation and directional first derivative can again allow to achieve omnidirectional edge-enhancement [Mazzaferri and Ledesma, 2007, Mazzaferri et al., 2010].

1.2.1.2 Coherent correlators

The highest SNR is achieved for a filter whose transfer function corresponds to the complex conjugate of the Fourier transform of the signal we are looking for [Das, 2012, Iizuka, 2008]. The correlation between observed and reference image is obtained by placing in the Fourier plane of the processor, a mask corresponding to the transfer function of this filter. In this case, a maximum in the ratio between image peak intensity and rms of noise (supposed additive and white) is achieved and the light meter at the output plane in Fig. 1.4 detects a maximum.

As we have seen for the case of edge enhancement, in the early developments of optical processors the transfer function was achieved by inserting independent amplitude and phase masks which only allowed for very simple patterns for matched filters. In 1963, van der Lugt synthesized frequency-plane masks that were able to control both amplitude and phase simultaneously. These masks were realized by means of a modified Mach-Zender interferometer where the complex input signal was combined with a known reference wave [van der Lugt, 1964] to render the *matched filter*.

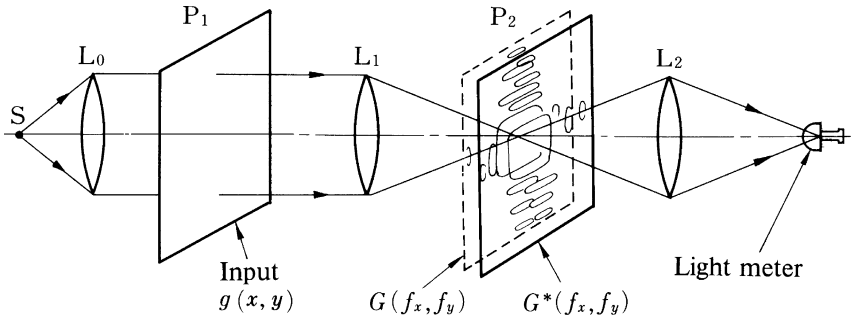

Figure 1.4: 4f processor with matched filter (from [Iizuka, 2008]).

Later, in 1966 Weaver and Goodman [Weaver and Goodman, 1966] presented a new correlator architecture know as Joint Transform Correlator (Figure 1.5) in which reference and signal images are presented side by side in the input plane before Fourier transforming and two peaks of cross-correlation of interest are present in the output plane, with the great advantage that no correlation filter is needed.

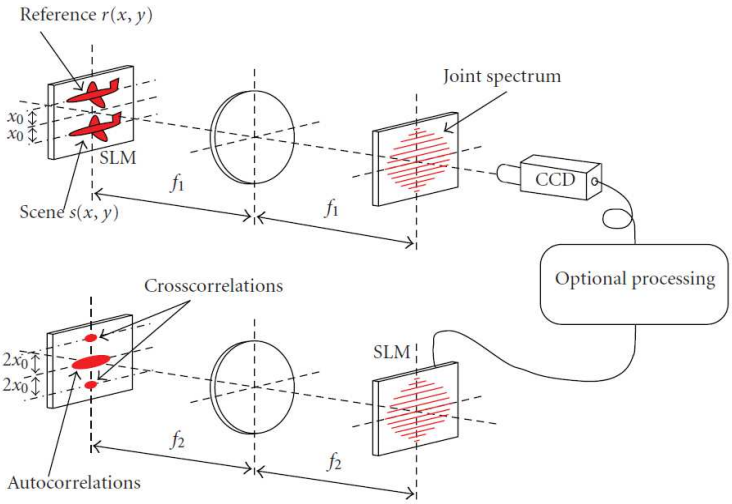

Figure 1.5: Joint Transform Correlator (from [Ambs, 2010]).

1.2.2 Incoherent architectures for image processing

We will now deal with completely spatially incoherent systems which are linear in light intensity [Rhodes and Sawchuk, 1981, Bartelt et al., 1982]. Image processing in incoherent systems cannot rely on the manipulation of Transfer function at Fourier plane. Those systems instead might be developed by the application of the Van Cittert-Zernike theorem [Goodman, 1985] to coherent systems operating on objects

which do not change the phase of the coherent beams that pass through them. Through this approximation it has been possible to develop devices such as entrance pupil filters and spatial frequency filters. The general approach would be to consider the response to each element of the extended source and, as the elements are mutually incoherent, their system responses add on intensity basis.

As a result of intensity adding, one of the main advantages concerning the use of incoherent sources in optical processing is the freedom from noise arising from speckle and dust specks on the optical components. Due to the extended nature of the incoherent source (LED arrays for example), light from a single pixel of the input passes through the optical system along many different spatial channels, and this redundancy is responsible for the absence of coherent noise in the system. However, the result of incoherent adding at imaging plane light scattered by specks is a reduction in image contrast.

By relaxing the requirements in spatial and/ or temporal coherence, the resulting increase of degrees of freedom [Lohmann et al., 1996] in the optical system may be an advantage. For example, as pointed out in [Bartelt et al., 1982] the gain in SNR in comparison to coherent counterpart is proportional to the square root of the number of optical channels, up to the limit of SBP of the object. For an SBP of 10^6 (typical number of pixels of a CCD sensor) an increase in 10^3 in SNR is to be expected.

Another advantage stems from the fact that the Optical Transfer Function of the system corresponds to the autocorrelation of the pupil function of the system (see Appendix A), so any defect in the pupil plane may be absorbed in the integration process.

1.2.2.1 Incoherent edge-enhancement

Based on quasi-monochromatic spatially incoherent light it is possible to achieve selective edge-enhancement. In a modified Fresnel incoherent correlation holography (FINCH) setup, Bouchal and Bouchal [Bouchal and Bouchal, 2012] use a LED source and an spectral filter to achieve the quasi-monochromatic source (see Figure 1.6). By means of optical scanning holography (OSH), isotropic [Pan et al., 2014] as well as anisotropic (directional) [Dobson et al., 2016] edge-enhancement has also been achieved.

An advantage of incoherent optical processors is that the nature of the input and the output is the same (intensity distribution). A coherent processor relies on a complex wave distribution processed through the system, but what we detect at the output is in the form of intensity. In incoherent processors information is carried by intensity wave distributions which constitute real, nonnegative signals.

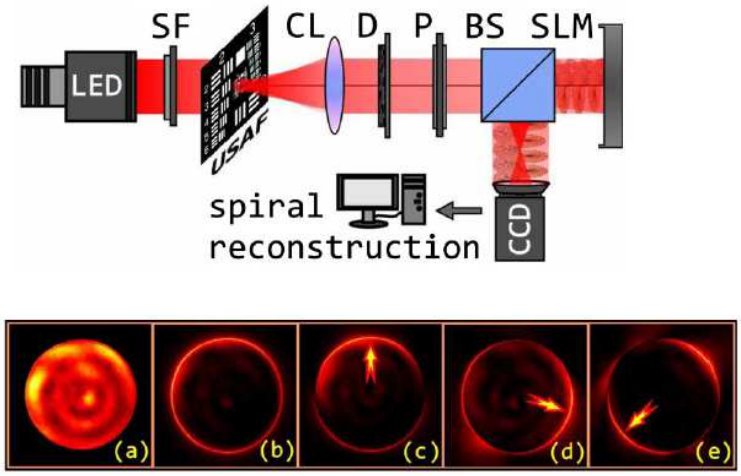

Figure 1.6: (Top) Experimental setup for edge-enhancement in modified FINCH. SF, spectral filter; CL, collimating lens; D, diaphragm; P, polarizer; BS, beam splitter; SLM, spatial light modulator. (Bottom) Isotropic and anisotropic edge contrast enhancement: (a) standard FINCH reconstruction,(b) isotropic spiral FINCH, (c)-(e) anisotropic spiral FINCH with preferred directions (from [Bouchal and Bouchal, 2012])

This gives rise to another source of contrast reduction in incoherent imaging since a bias needs to be added in order to achieve negative signals. Early attempts to spatial filtering with incoherent light might be found in the use of the photographic Herschel effect [Kelly, 1961] or bipolar aperture masks [Trabka and Roetling, 1964] where high-pass filtering of images is obtained by using the quenching characteristics of a fluorescent screen. Alternatively, the use of hybrid systems to perform electronically those coherent operations not available through incoherent illumination is suggested in [Stoner, 1978].

Most of the preprocessing efforts in incoherent optics are directed towards the enhancement of edges in images [Flores et al., 2010, Flores et al., 2011] rather than its detection on a zero background. This enhancement can be achieved by the combination of a *positive* input image and its *negative* shifted version; let us take as an example the directional enhancement worked out in [Fernández et al., 2011]. The positive image is the one observed in a Liquid Crystal Display (LCD) under its standard configuration, i.e. liquid crystal placed between an analyzer (in front of the LCD) and the back polarizer of the display in cross configuration with the analyzer. The orthogonally polarized replica of this image is the negative image or complementary color image which is absorbed by the front polarizer. If the analyzer is removed both

positive and negative images are available for processing. Figure 1.7 shows a setup for directional edge enhancement where a calcite prism is used to separate rays of crossed polarization. When both images are superimposed laterally displaced across the image plane, one obtains an image with enhanced first-order derivatives along a specific direction. Figure 1.8 shows, along with the positive and negative original images, the edge enhancement that results from a vertical displacement between them.

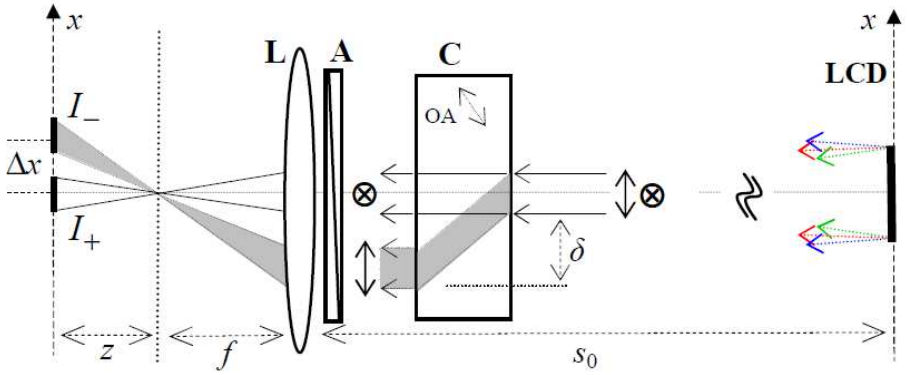

Figure 1.7: Directional edge enhancement setup. LCD, liquid crystal display (whose analyzer film has been removed); C, calcite prism producing a lateral separation δ between cross-polarized beams; A, analyzer (at 45° with respect to the polarization of positive and negative image, in order to give a superimposition at the image plane); L, lens system; $I_\pm$: positive (negative) image.

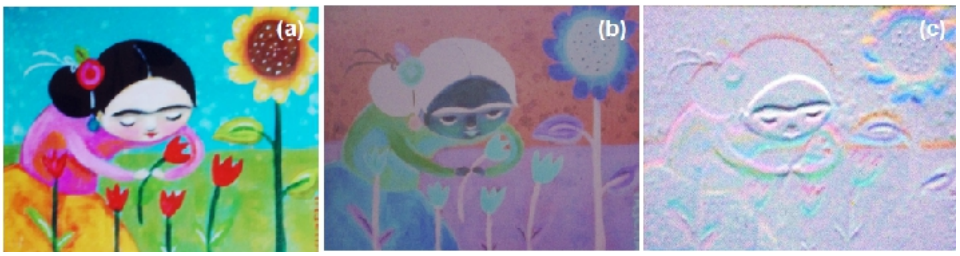

Figure 1.8: Directional edge enhancement with the setup from Figure 1.7. (a) Positive image (b) Negative image (c) Edge enhancement.

For non-directional edge-enhancement of images, in [Flores et al., 2011] a pupil mask formed with concentric apertures and orthogonal polarizers (Figure 1.9) is placed in front of the same modified LCD (i.e. with analyzer removed) allowing to simultaneously image a well-focused positive replica (due to the circular aperture) superimposed to a slightly defocused negative one (due to the annular aperture).

Through the combination of the positive input and a its blurred negative, a Laplacian (second derivative) edge-enhancement is obtained. Figure 1.10 shows the laplacian-enhanced image along with the original image and its defocused negative.

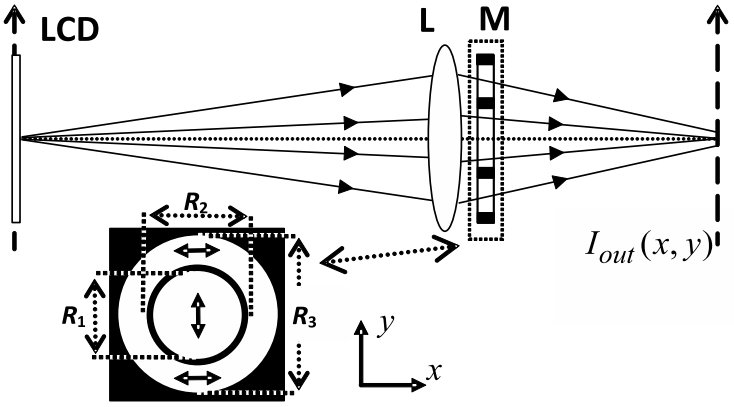

Figure 1.9: Setup for non-directional edge enhancement. The compound analyzer (M) has a central circular region of radius R_1 and an annular region (with inner and outer radius R_2 and R_3, respectively) with transmission direction orthogonal to that of the central region. The difference in depth of focus between central and annular regions allows to combine differently focused positive and negative images.

Figure 1.10: Laplacian edge enhancement with the setup from Figure 1.9. (a)Positive image (b)Defocused negative image (c)Non-directional edge enhancement

1.2.2.2 Incoherent correlators

Lohmann proposed the extension of coherent matched filters to the incoherent regime where monochromatic extended sources or self-luminous objects can be used in what is known as *quasi*-monochromatic correlation, since spatially incoherent light cannot be totally monochromatic for the relative phase of the light emitted by two different points of the source to change in time and yield spatial incoherence. As in the coherent case, the image forming system can be considerer linear but in the intensity

instead of the complex amplitude of the field. The matched filter is again the complex conjugate of the Fourier transform of the signal that we want to detect. Although the general synthesis problem [Lohmann, 1968] might result difficult, in character recognition applications [Armitage and Lohmann, 1965] the matched filters can be realized by means of binary masks at the pupil plane of the optical system.

For the use of totally incoherent light in optical correlators, achromatic compensation [Bouchal et al., 2014, Morris and Zweig, 1987] needs to be performed. Appropriate combinations of refractive and diffractive elements have resulted in achromatic Fourier processors in which it is possible to use white light input signals in correlation optics [Yu, 1987, Pe'er et al., 1999] or data encryption [Tajahuerce et al., 2001, Tajahuerce et al., 2005] (see Figure 1.11 where an incoherent encryption system using a white light source and dispersion compensators is depicted).

Aside from incoherent extensions of Fourier processors, optical correlation can be achieved in the geometric optics limit. Early attempts to obtain autocorrelation of random patterns can be found in [Kovasznay and Arman, 1957] while a review of incoherent correlators based in scanning or defocusing can be found in [Monahan et al., 1977] and [Knopp and Becker, 1978], respectively. Another type of geometric incoherent correlators are based on the shadow casting principle (Figure 1.12) and have been proposed for image segmentation by active contours [Hueber et al., 2001, Hueber et al., 2003] as well as for the parallel implementation of logic operations [Tanida and Ichioka, 1983] by means of a lensless technique.

Our proposal for an optical implementation of the GHT falls under the category of geometric incoherent correlators. In Chapter 3 we develop, based on linear optical systems theory, the idea that led us to implement the aforementioned transformation in a severely defocused system where scale and orientation parameters can be controlled. Previously, we would need to introduce in Chapter 2 the main concepts related first to the linear HT, then to its generalized version to treat arbitrary geometrical features.

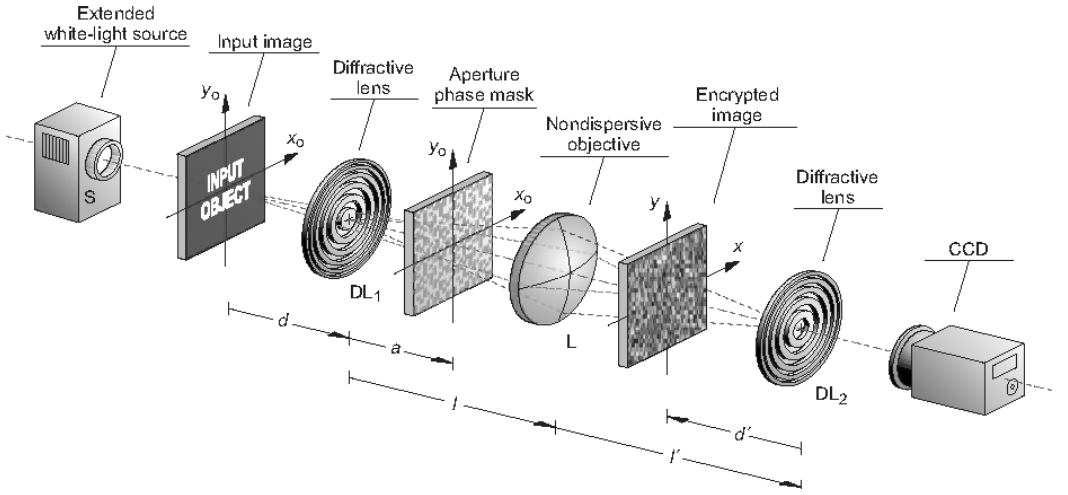

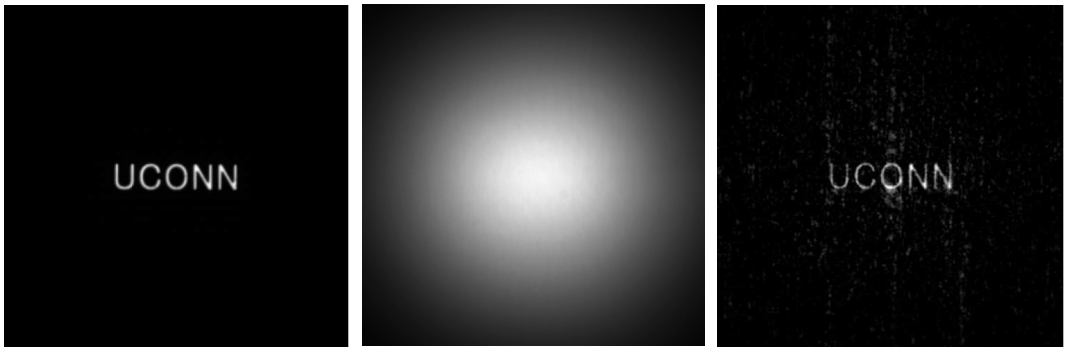

(a) (b) (c)

Figure 1.11: (Top) Dispersion-compensated processor for optical encryption with incoherent light (Bottom) (a) original image (b) encrypted image at the output of the processor (c) digitally decrypted image (from [Tajahuerce et al., 2005]).

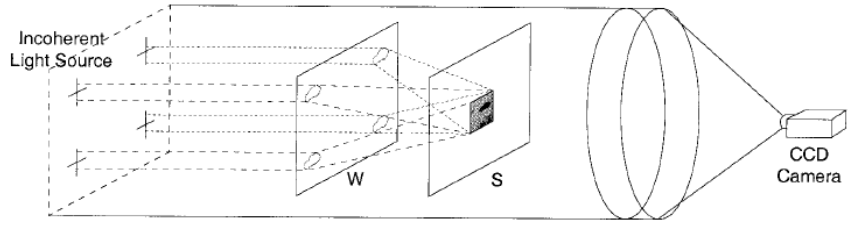

Figure 1.12: Multichannel incoherent shadow-casting correlator with four channels. Correlation is performed between scene (S) and window (W) (from [Hueber et al., 2003]).

Chapter 2

Hough transform and its optical implementation

One of the most important tasks in automated image analysis is the recognition of geometrical features. This *high-level* feature extraction task [Nixon et al., 2012] involves using shape information from the image (in comparison, *low-level* tasks like edge-enhancement are accomplished without any knowledge of the shapes involved). Even for the recognition of the simplest feature like a straight line, the direct search and detection in an entire image is computationally costly. While trying to detect the track of subatomic particles in bubble chamber photographs, Hough faced the problem of detecting the presence of groups of collinear dots on an homogeneous background. He devised and patented what nowadays is known as *Hough Transform* [Mukhopadhyay and Chaudhuri, 2015, Leavers, 1993, Illingworth and Kittler, 1988], a transformation that exchanges the global line detection for a more easily solved peak detection problem in a parameter space dual to the original binary image.

The resulting Linear Hough Transform and its extensions to other shapes (like the Circular Hough Transform) are among the most popular techniques for shape detection in images. A search on *Scopus* from 2000 to 2015 returns over 7000 articles related to Hough transform; its widespread use is due to its robustness against noise [Lu et al., 2015, Lu and Tan, 2008] , incompleteness of the target shape [Cauchie et al., 2008, Blanco et al., 2006] or low resolution of the image [Wang et al., 2009, Loce et al., 2013].

Applications of the Linear Hough Transform can be found in text line extraction from skewed document images [Shivakumar et al., 2005], detection of traffic symbols from low resolution images [Tai and Chen, 2014] or robust lane detection [Niu et al., 2015], line detection in large images [Song and Lyu, 2005], building detection in aerial imaging [Cha et al., 2006], surgical instruments tracking [Climent and Hexsel, 2012],

general recognition of lines in natural scenes [Fernandes and Oliveira, 2008] among others (Figure 2.1). Recent applications of the Circular Hough Transform include improvement in Shack-Hartmann wavefront sensing [Chia et al., 2016], detection of a common center in X-ray diffraction images [Cauchie et al., 2008] and detection of optical disk in fundus images [Blanco et al., 2006] (Figure 2.2).

The Generalized Hough Transform -an extension of the Hough Transform to nonparametric features- has in turn proven to be useful, for example, in automated satellite imagery navigation [Chen and Deng, 2015], medical imaging [Ricca et al., 2015], identification of chips [Ulrich et al., 2003] or tag devices [Yang et al., 2016] in assembly lines and fingerprint recognition [Qi et al., 2004] for biometric authentication (Figure 2.3).

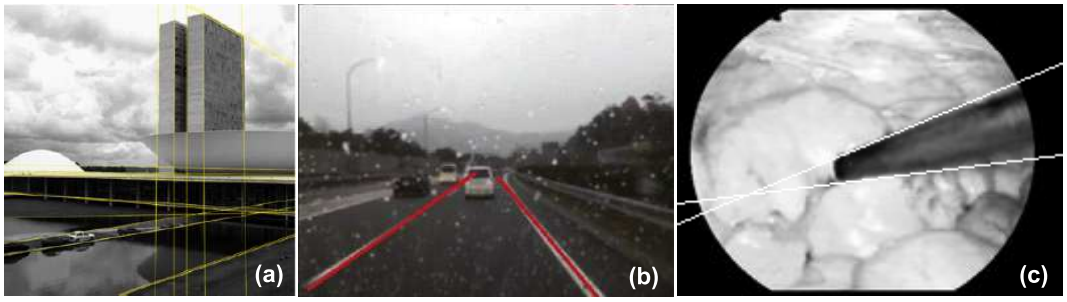

Figure 2.1: Applications of the Linear Hough Transform. (a) Line detection in natural scenes (from [Fernandes and Oliveira, 2008]) (b) robust lane detection in traffic images (from [Niu et al., 2015]) (c) surgical instruments tracking (from [Climent and Hexsel, 2012]).

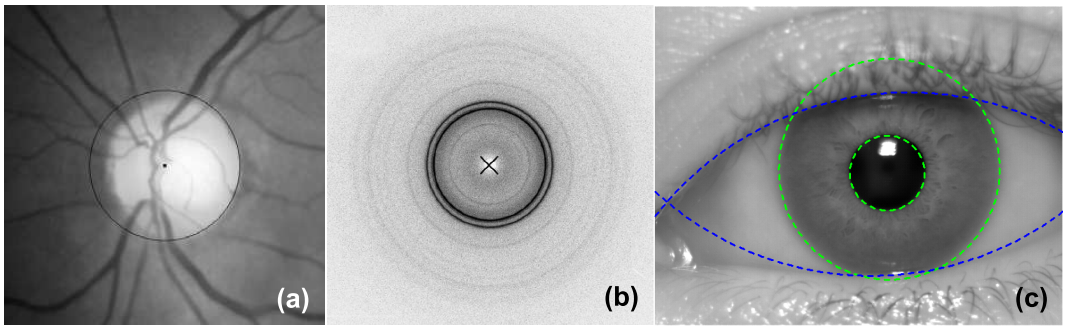

Figure 2.2: Applications of the Circle Hough Transform. (a) Optical disk extraction in fundus images (from [Blanco et al., 2006]) (b) Center detection in Debye-Scherrer rings in crystallography imaging (from [Cauchie et al., 2008]) (c) iris segmentation in infrared images (image from *UTIRIS* repository (https://utiris.wordpress.com/2014/03/04/university-of-tehran-iris-image-repository) processed by the author).

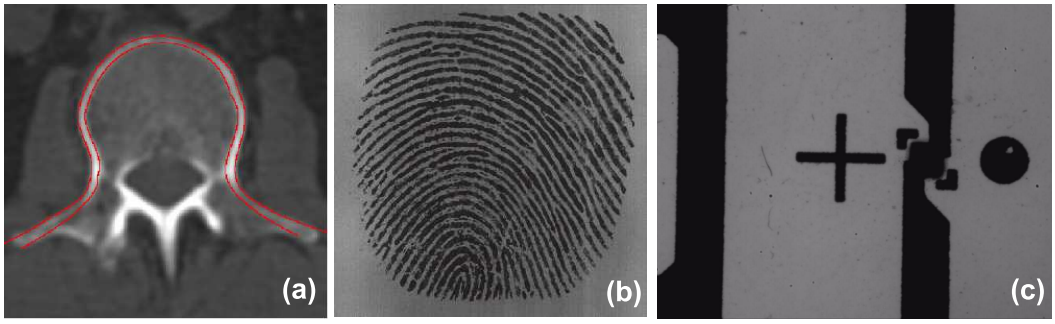

Figure 2.3: Applications of the Generalized Hough Transform. (a) Piece-wise approximation of vertebra in X-ray CT image (from [Ricca et al., 2015], template in red) (b) fingerprint authentication (from [Qi et al., 2004]) (c) radio frequency identification device tag positioning (from [Yang et al., 2016]).

We start this chapter by describing the fundamentals of the Hough Transform. In his patent [Hough, 1962] Hough disclosed a key idea that survives to the present formulation of the Linear Hough Transform: collinear points in a binary image can be identified by mapping them into geometric constructions that intersect in an *accumulator* space.

2.1 Linear Hough transform

In the original formulation Hough considered a geometrical construction [Hart, 2009] that was later put into analytical form as a point to line transformation using the slope-intercept parametrization of a line:

$$f(x, y) = y - mx - c = 0 \tag{2.1}$$

where m represents the slope parameter and c the interception of the line with the y axis. Equation (2.1) is symmetric in the role of (x, y) and (m, c) an so it can also be seen as the equation for a line in $\{m, c\}$ plane with slope $-x$ and intercept $-y$ so that we can map every point of the original image in $\{x, y\}$ space to parameter space $\{m, c\}$ under the dual of Equation (2.1)

$$g(m, c) = y' - mx' - c = 0 \tag{2.2}$$

where (x', y') is the coordinate of pixel being mapped. Collinear pixels in the image space are mapped to concurrent lines in the parameter space but this space is unbounded when considering mapping of points lying on a vertical line. Following the work of Duda and Hart [Duda and Hart, 1972] a straight line can be more use-

fully parameterized in terms of the algebraic length ρ and orientation θ of the vector normal to the line passing through the image origin (Figure 2.4)

$$f(x, y) = x\cos(\theta) + y\sin(\theta) - \rho = 0. \tag{2.3}$$

For this *normal* parametrization to define a unique line we need to restrict parameter θ: $\theta \in (-\pi/2, \pi/2]$. Besides, parameter ρ is bounded by the maximum point distance in the original image (for example, the diagonal of a $M \times N$ image). It is also noticeable that function $\rho(\theta) = x\cos(\theta) + y\sin(\theta)$ verifies $\rho(\theta + \pi) = -\rho(\theta)$.

Each point of the original image is mapped under Equation (2.3) to a sinusoidal curve in a bounded parameter space $\{\rho, \theta\}$ where the point cast a vote for every parameter combination that gives rise to a line passing through it. The intersection of this voting curves indicates points belonging to a common line in the original image. Accumulation of votes over the different parameter combinations gives rise to the *Linear Hough Transform* (LHT) of the original image. The computational complexity for the LHT of an $N \times N$ image is $O(N^4)$ [Feng and Fainman, 1992, Hollitt, 2013] since the transform needs to accumulate votes on a two-dimensional surface for every of the N^2 points of the image.

As a simple illustration of this parametrization consider the three point image of Figure 2.5(a) with the possible lines passing through two points marked in different colors. Figure 2.5(b) shows the accumulator space, where the coordinates of the intersection point of two sinusoidal curves are the parameters of two-point concurrent line in the original image. For binary images with n non null points we will have n different curves in the accumulator space and a threshold should be established in order to sort out the most voted lines.

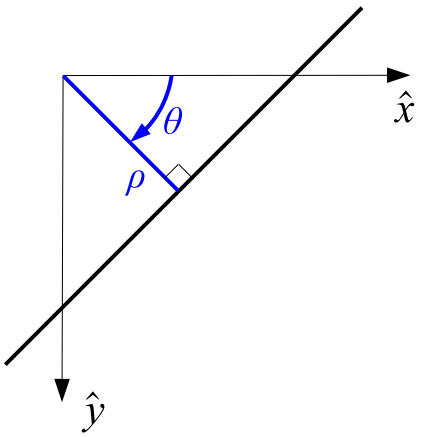

Figure 2.4: Normal Parameters (ρ, θ) for the representation of a line in the Hough transform.

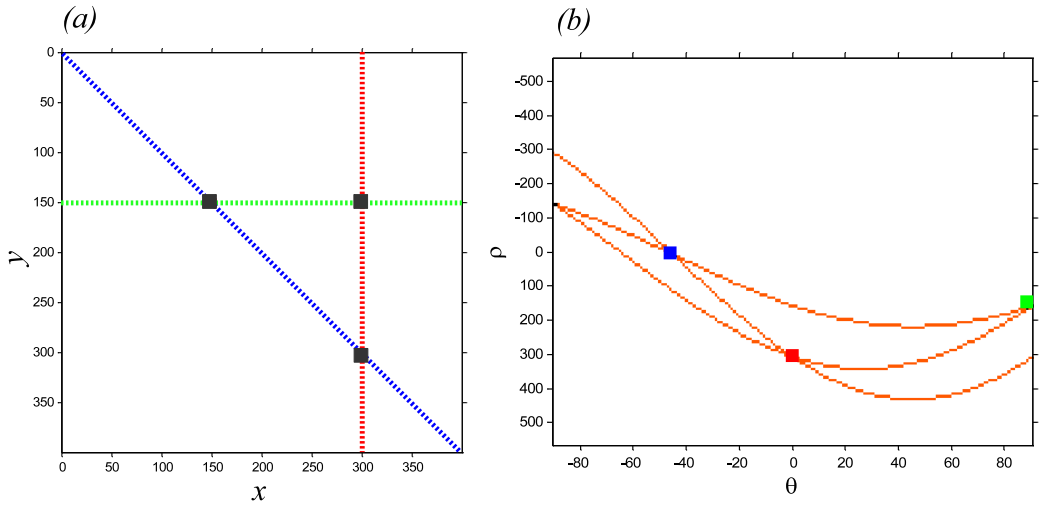

Figure 2.5: LHT of three point image. (a) Original image (b) Accumulator space $\{\rho, \theta\}$ (θ in degrees) where the intersection points follow the color of the corresponding line in the original image.

2.1.1 The Radon connection

Deans [Deans, 1981] pointed out the close connection between the HT and the *Radon Transform* -whose mathematical formalism will be presented in the next chapter (see Section 3.1)- which corresponds to the representation of an arbitrary (not exclusively binary) function over the $\{x, y\}$ plane by means of the integrals along different directions on the plane [Radon, 1986]. This type of image representation has proven to be useful in different pattern recognition tasks and especially in medical imaging [Herman, 2009], where the development of efficient methods for approximating the inversion of the transform is fundamental to computarized tomography. The connection is worth noticing since early attempts at optical Hough transform implementation (see Section 2.4) were based on rotating inputs and integrating along narrow slits in order to give the signal in terms of its line integrals.

2.2 Circle Hough Transform (and other analytic curves)

We can easily extend the ideas for line detection to other analytical curves for which we have a parametric representation. The points (x, y) that lie on a circle of center (x_0, y_0) and radius R satisfy this constraint equation

$$f(x, y) = (x - x_0)^2 + (y - y_0)^2 - R^2 = 0, \tag{2.4}$$

and the parameters $\{x_0, y_0, R\}$ span a three-dimensional accumulator space where each point of the original image cast a vote for every parameter combination giving a circle whose center coincides with it. In this way, a point under the *Circle Hough Transform* (CHT) is mapped to a cone in $\{x_0, y_0, R\}$ (accumulator) space, which can be easily seen by fixing x and y in (2.4) and letting x_0, y_0, R vary. For fixed values of R let us consider the 2D slices of the accumulator space spanned by the remaining parameters x_0, y_0; for a given value R every point of the original image is mapped under CHT to a circle with this radius. Consider for example the three point image depicted in Figure 2.6(a) corresponding to three of the vertices of a square of side L. In the corresponding accumulator space slice for $R = \frac{3L}{5}$ (Figure 2.6(b)) each of the original points is mapped to a circle of radius $R = \frac{3L}{5}$; the intersection of these circles in the accumulator space indicates the center of each of the four different circles passing through two points in the original image. For $R = \frac{L}{\sqrt{2}}$ (Figure 2.6(c)) the corresponding accumulator space slice (Figure 2.6(b)) shows, besides different two-circles intersection points- a triple intersection corresponding to the center of the circle that passes through every of the three points of the original image.

A variation of the basic mapping under the CHT to include scale invariant detection can be found in [Atherton and Kerbyson, 1999] while a convolution approach to the transformation is implemented in [Hollitt, 2013] with the advantage of reducing the computational complexity of the transform from $O(N^4)$ to $O(N^3 log(N))$.

Another analytical feature of interest is the ellipse, whose constraint equation reads

$$f(x, y) = \frac{(x - x_0)^2}{a^2} + \frac{(y - y_0)^2}{b^2} - 1 = 0, \tag{2.5}$$

where (x_0, y_0) is the center of the ellipse and a and b the semi-axis that we assume to coincide with the x and y axis. To handle the possible rotation of the ellipse we need to introduce a rotation parameter θ and the five-dimensional parameter space is $\{x_0, y_0, a, b, \theta\}$. Similar approaches can be introduced to other analytical, parametric geometrical features like parabolas where we need to span a four-dimensional parameter space.

2.2.1 Circle matching

For a given radius R we have interpreted the CHT as the mapping of each point of the original image to a circle of radius R in accumulator space, where votes accumulate over a given parameter space point according to the number of circles that intersect at this point. Alternatively, we can consider the *matching* of the circle of radius R to the complete original image by tracing the circle with its reference (x_0, y_0) over every point (x, y) in the image and computing the number of points of the image that lie on

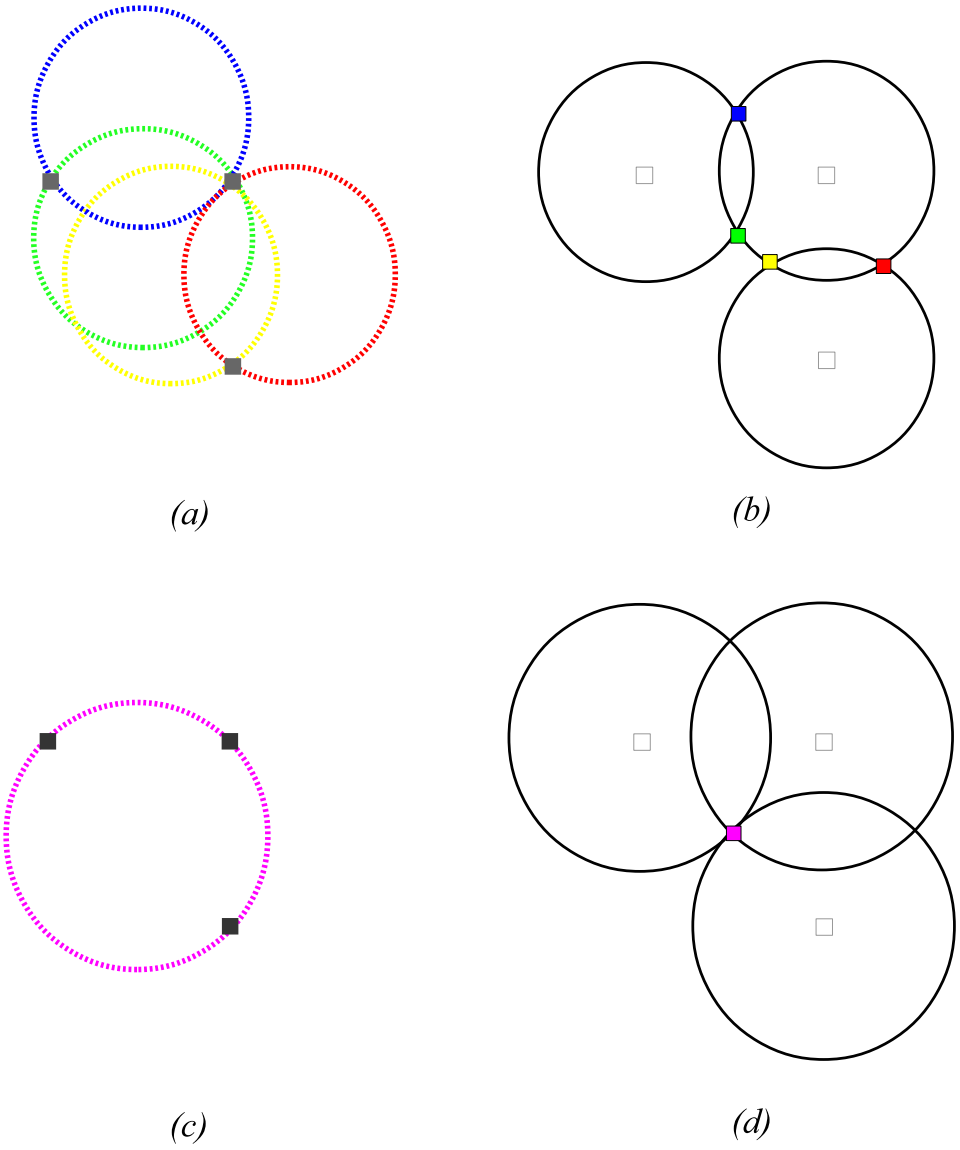

Figure 2.6: CHT of three point image. (a) Original image of 3 vertices of a square of side L (b) Slice of accumulator space for $R = \frac{3L}{5}$ where the intersection points follow the color of the corresponding circle in the original image (a) (silhouette of the original points superimposed). (c-d) same as (a,b) for $R = \frac{L}{\sqrt{2}}$

the shape. This gives the same vote sum and would prove to be an useful approach when we consider the matching of a non-analytical *template* in the next section. As an example, consider the image formed by three points in Figure 2.7 where for the center of a circle of radius $R = \frac{L}{\sqrt{2}}$ coinciding with $\left(x_0^{(1)}, y_0^{(1)}\right)$, $\left(x_0^{(2)}, y_0^{(2)}\right)$ and $\left(x_0^{(3)}, y_0^{(3)}\right)$ we obtain 1,2 and 3 votes, respectively.

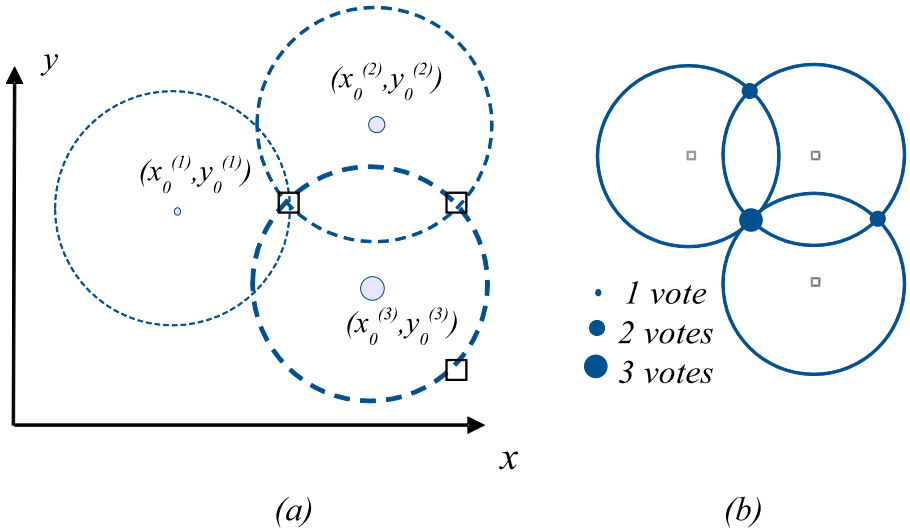

Figure 2.7: (a) Matching of a circle of radius $R = \frac{L}{\sqrt{2}}$ to a 3 point image of the vertices of a square of side L (the number of votes corresponding to the circle centers $\left(x_0^{(1)}, y_0^{(1)}\right)$, $\left(x_0^{(2)}, y_0^{(2)}\right)$ and $\left(x_0^{(3)}, y_0^{(3)}\right)$ has been superimposed in light blue) (b) Resulting CHT with the points of the original image superimposed.

2.3 Generalized Hough transform

Pattern recognition tasks involve in many cases the matching of a template of more general geometry than lines or circles to a given target image. Besides, this template can seldom be represented through an analytical constraint equation. In order to handle non-analytical features, Ballard [Ballard, 1981] proposed a four parameter space $\{x_0, y_0, s, \theta\}$ for an arbitrary figure (Figure 2.8), where (x_0, y_0) is a reference point, s is the (isotropic[1]) scale parameter and θ the orientation of the shape (as given for example by the gradient orientation at a certain point).

[1] a general treatment should include a scale factors vector $\mathbf{s} = (s_x, s_y)$ to take into account anisotropic transformations but the experimental implementation of the Generalized Hough Transform will consider isotropic scale variations and handle anisotropy by changing the template.

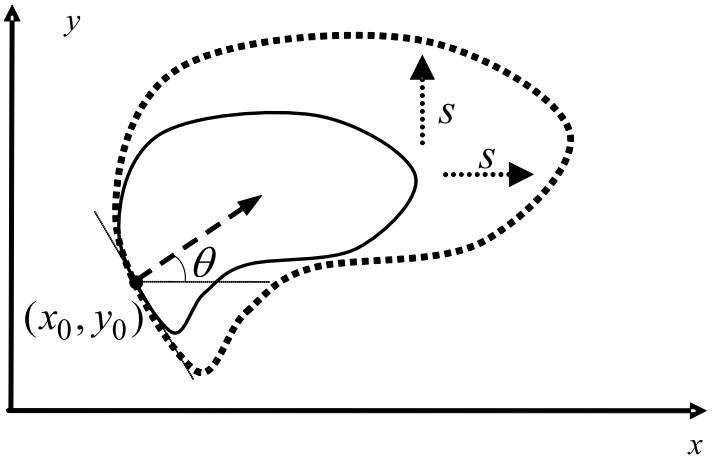

Figure 2.8: Parameters $\{x_0, y_0, s, \theta\}$ for an arbitrary shape.

The constraint equation for the shape of interest can be written as

$$f(x - x_0, y - y_0; s, \theta) = 0. \tag{2.6}$$

For a given orientation and scale (i.e. (s, θ) fixed), the *Generalized Hough Transform* (GHT) algorithm will proceed [Merlin and Farber, 1975, Sklansky, 1978] by tracing the shape with its reference (x_0, y_0) over every point (x, y) in the image, and computing the number of points of the image that lie on the shape (as it was previously introduced for the case of a circle in Section 2.2.1). Figure 2.9 shows a very simple example of the procedure for the shape depicted in Figure 2.8 traced over a four point image (depicted as squares) where for reference coinciding with $\left(x_0^{(1)}, y_0^{(1)}\right)$ (see solid line in Figure 2.9), the shape matches all the four points while for $\left(x_0^{(2)}, y_0^{(2)}\right)$, $\left(x_0^{(3)}, y_0^{(3)}\right)$ we get a partial matching.

The final step for pattern recognition is to find for which reference point we obtain the maximum coincidence. To account for a change in scale or orientation the corresponding parameters need to be varied and the procedure repeated, yielding a four-dimensional accumulator space. Alternatively to the previous algorithm, general shapes can be piecewise represented by means of line segments or composite figures including parametric features such as circles or ellipses [Ricca et al., 2015]. In the next section we will review optical approaches to the GHT which make use of such approximations.

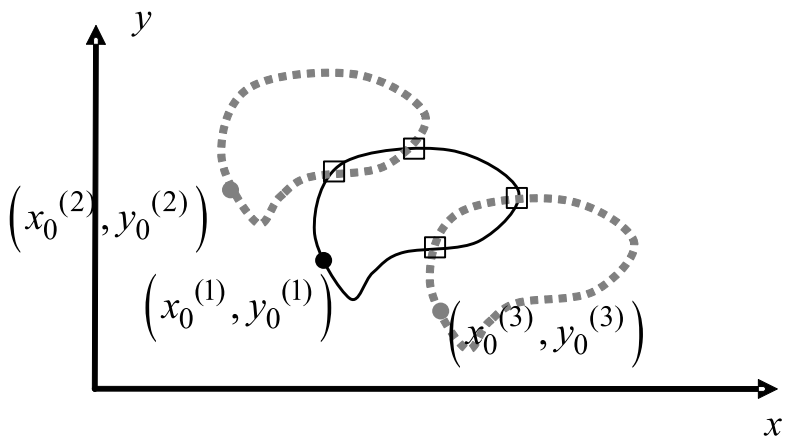

Figure 2.9: Matching of the arbitrary shape of Figure 2.8 to a four point image. Best fit in solid line.

2.4 A review of optical approaches

The principal drawback for a standard shape recognition algorithm based in the Linear Hough Transform (LHT) is its large computational requirements which makes its real-time implementation difficult. On the other hand, as we saw in Chapter 1, optical architectures offer parallel computing capability and are therefore inherently suitable for real-time applications.

2.4.1 LHT and CHT in the coherent regime

Steier and Shori [Steier and Shori, 1986] proposed an implementation of the LHT that takes advantage of the close relation of this transform to the Radon Transform (RT) (see Section 2.1.1). Using a Dove prism to rotate the input image (Figure 2.10) and projecting on a line detector by means of a cylindrical lens they were able to obtain the LHT of an image. A similar coherent approximation and rotating input to the LHT can be found in the work of Gindi and Gmitro [Gindi and Gmitro, 1984].

Following the same connection to the RT, Eichmann and Dong [Eichmann and Dong, 1983] proposed the use of a narrow slit at the Fourier plane (P_2 in Figure 2.11) of a 4f system while rotating the input image at P_1 and translating the output recording material in P_3. A more efficient implementation of the RT in a 4f system has recently been proposed in [Ilovitsh et al., 2014], where a vortex-like mask is placed at the Fourier plane and no rotation of the input is needed in order to obtain the transformation. Stern [Stern, 2007] explored the optical implementation of RT for few angular directions, which resulted suitable for real-time low-resolution tasks like

motion detection [Kashter et al., 2012] or image restoration when combined with super-resolution [Farber et al., 2013]. Seth and Datta [Seth and Datta, 1996] implemented the LHT also in a coherent setup via an optical matrix-vector multiplication technique combined with a two-layer neural network. The peak strength of a neuron in the Hough space is detected by a winner-take-all optoelectronic circuit.

Ambs et al. [Ambs et al., 1986] proposed the use of a 2D array of holograms with varying impulse response, constituting a space-variant filter. In their setup (Figure 2.12) each hologram of the filter reconstructs a different sinusoidal curve according to the parametrization given by Equation (2.1) or (2.3). Alternatively, they consider the detection of a circle of given radius (CHT) and include in each hologram the center coordinate. Mori and Ohba [Mori and Ohba, 1994] also explored the use of an array of computer generated holograms for the implementation of the LHT. Shin and Jang considered rotationally multiplexing holograms [Jang and Shin, 1996, Shin and Jang, 1998] of a line feature at discrete orientation angles for the implementation of the LHT under coherent light.

For the detection of the (five) parameters of a general ellipse, Feng and Fainman [Feng and Fainman, 1992] proposed an extension of the holographic method of Ambs et al. [Ambs et al., 1986] and consider the envelope of the sinusoidal lines that result from the mapping of the points of the ellipse under the normal line parametrization in Equation (2.3). The case of a line segment is also covered as a particular case with one of the semi-axis of the ellipse equal to zero.

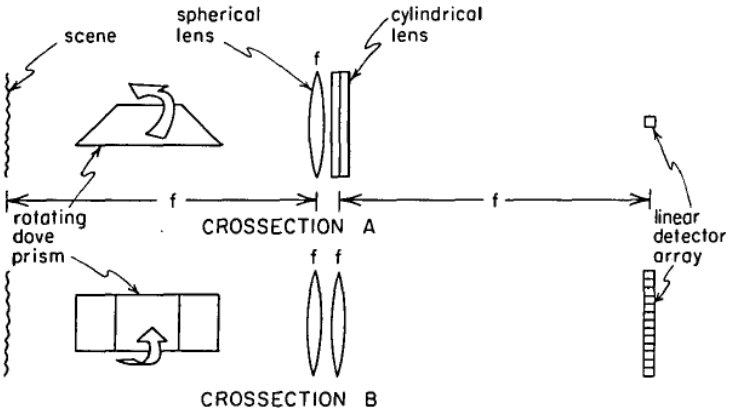

Figure 2.10: Setup for optical implementation of the LHT under coherent light and rotating input (from [Steier and Shori, 1986]).

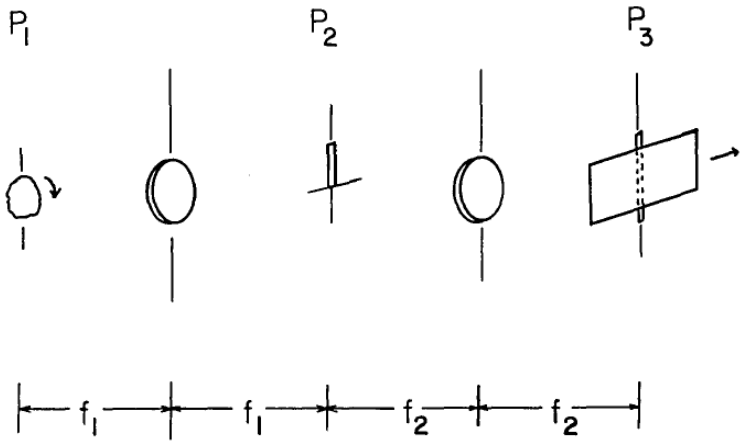

Figure 2.11: Setup for optical implementation of the LHT in a 4f-system (from [Eichmann and Dong, 1983]).

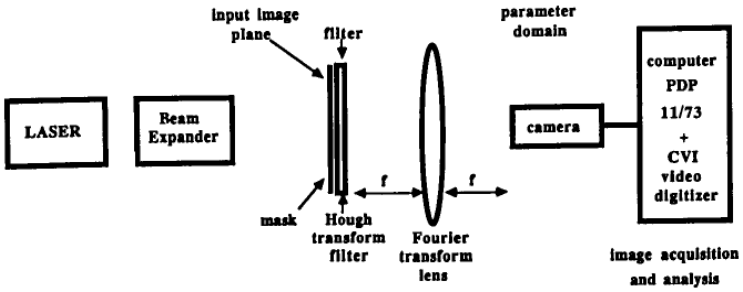

Figure 2.12: Setup for optical implementation of the LHT with a holographic array filter (from [Ambs et al., 1986]).

2.4.2 LHT in the incoherent regime

With the advantage of achieving larger signal-to-noise ratio, Steier and Shori proposed a variation of the scheme of Figure 2.10 that allows to obtain an incoherent transformation but again only for a line (LHT). In the same regard, Stern [Stern, 2007] proposed besides the coherent compressed RT, an incoherent variant whose setup is depicted in Figure 2.13. Koppelhuber and Bimber [Koppelhuber and Bimber, 2015] recently proposed a classification scheme based in the optical RT with incoherent illumination. They developed a thin film sensor capable of measuring the RT of an image focused on it and they later implemented a classification scheme in Radon space from few projections. Schmid et al. [Schmid et al., 1998] also made use of incoherent light but with a microlens array processor that can detect lines with different positions and orientations. Their optical architecture works indeed as a preprocessor for the LHT and a classification scheme based in neural network is implemented afterwards.

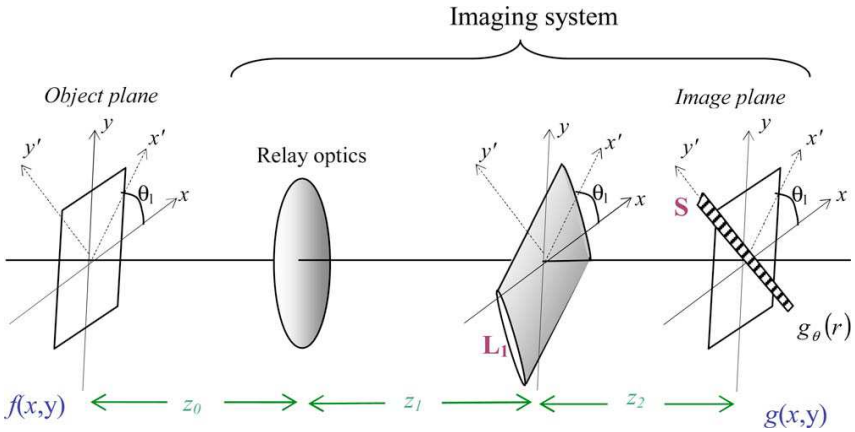

Figure 2.13: Setup for incoherent optical implementation of the compressed RT. L_1, cylindrical lens; S, vector sensor located in the image plane. The system performs an integral projection of the intensity distribution $f(x', y')$ on y'. The linear sensor S, aligned with the y' axis, captures the line integral $g(r = y')$ which can be recognized as a Radon transform (from [Stern, 2007]).

2.4.3 GHT in the coherent regime

For the optical implementation of the Generalized Hough Transform (GHT), the use of acousto-optically modulated lasers and the piece-wise representation of the template through analytical curves was proposed by Casasent and Richards [Casasent and Richards, 1993]. Javadpour and Keating [Javadpour and Keating, 2000] gener-

alized the method of Seth and Datta [Seth and Datta, 1996] to handle non analytical shapes by considering a look-up table that defines the shape and also speeded up the basic configuration introducing an acousto-optical implementation of the matrix-vector multiplication. Shin and Jang [Shin and Jang, 2000] proposed an implementation of the GHT with a matrix of holograms (Figure 2.14). They accomplished scale (for the CHT) and rotation (for the LHT) -variant detection by means of recording van der Lugt filters (see Section 1.2.1.2) with scale or orientation variations of the reference pattern. Although the shift-invariance of the van der Lugt processor allows to overcome the need of different references in the shape, non-analytical templates can be handled by this method but this issue was not proved in the experiments.

In the next chapter we will introduce our proposal for the implementation of the GHT in the incoherent regime.

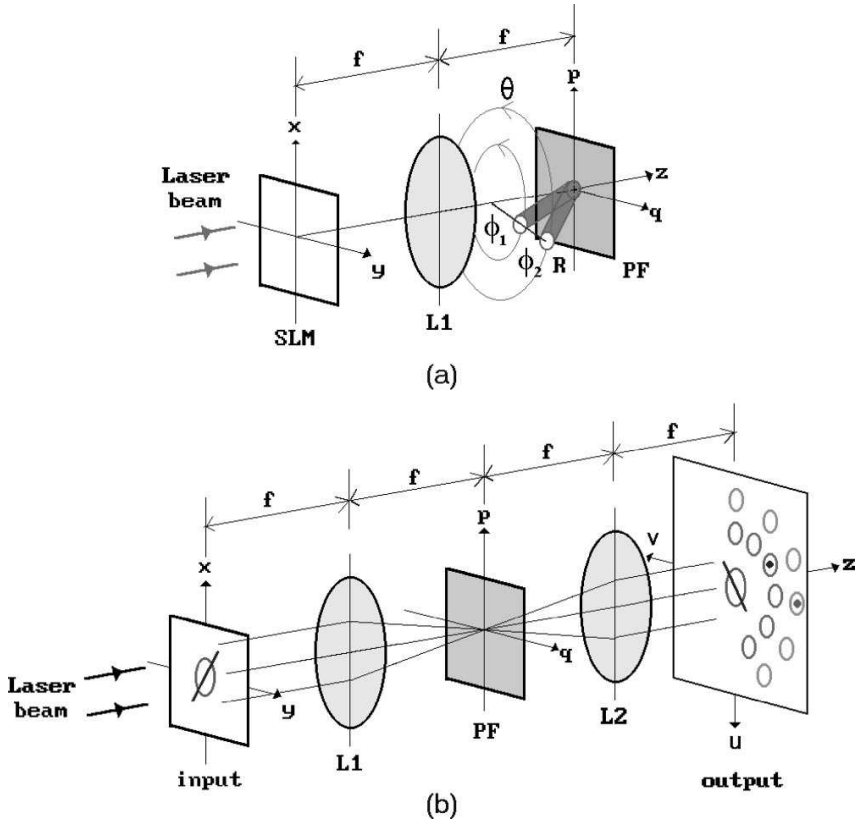

Figure 2.14: Coherent optical implementation of the GHT (a) Optical setup for recording; different van der Lugt filters are recorded in a holographic medium by use of rotational multiplexing; R, reference beam; PF, photopolymer film for hologram recording. L_1 lens performs the Fourier transform of the input pattern that is displayed in the spatial light modulator SLM. (b) When the input is applied to the multiplexed filters the cross-correlation terms between the input pattern and the stored patterns are obtained in parallel at the output plane (u, v) behind another Fourier transform lens L_2 (from [Shin and Jang, 2000]).

Chapter 3

Generalized Hough transform with incoherent light

The key of the proposed optical implementation of the Generalized Hough Transform (GHT) with incoherent light can be found in the integral representation of the transformation. In order to arrive at the integral representation of the GHT we start this chapter with a brief review of the Radon Transform (RT), closely related to the Linear Hough Transform (LHT). The RT is a representation of a given image in terms of integrals along different directions in the image plane (Radon projections). We can follow the generalization of this integral transformation to kernels corresponding to more complex shapes (see [Hendriks et al., 2005] and references therein) and connect this integral transformation for continuous functions with the GHT operating over binary images.

Based on this integral representation we propose a correlator [Fernández et al., 2015a] whose point-spread function corresponds to a highly blurred optical system. Focal setting along with the orientation of the pupil can be efficiently controlled by means of an electrical lens with variable focal length and a rotating pupil mask matching the pattern to be found. This correlator works under fully (i.e., both spatially and temporally) incoherent illumination and can handle orientation changes or scale variations in the pattern. Real-time is achieved (as limited by the frame rate of the device used to capture the GHT), allowing -besides static images- for the processing of video sequences.

3.1 Integral representation of the LHT: the Radon projections

Let $I(x, y)$ be an arbitrary function on the $\{x, y\}$ plane. The RT of $I(x, y)$ is defined as [Deans, 1981]

$$L(\rho, \theta) = R\{I\} = \iint_{-\infty}^{+\infty} I(x', y')\delta(x'\cos(\theta) + y'\sin(\theta) - \rho)dx'dy', \tag{3.1}$$

and one has a sample of the transform for each (ρ, θ) pair. To obtain the full transform we need to let (ρ, θ) vary so that L can be determined for arbitrary values of the normal parameters. It is worth noticing that the presence of the Dirac delta function forces the integration of $I(x, y)$ along a line whose normal form is given by (2.3): $\rho = x\cos(\theta) + y\sin(\theta)$, so a single point (ρ_0, θ_0) in Radon space is associated to a line in original space: $\rho_0 = x\cos(\theta_0) + y\sin(\theta_0)$. It is also easy to see from the definition in Equation (3.1) that for the case of a single point image, i.e. $I(x, y) = \delta(x - x_0, y - y_0)$, direct substitution gives a non-null value for L along the sinusoidal curve $\rho = x_0\cos(\theta) + y_0\sin(\theta)$. From these particular cases it is clear that when we deal with a binary image, the Radon Transform includes as a special case the Linear Hough Transform.

For the Circular Hough Transform (CHT) presented in Section 2.2 it is also possible to obtain an integral form. If $I(x, y)$ is the original binary image, its CHT $C(x, y, R)$ will be given by:

$$C(x, y; R) = \iint_{-\infty}^{+\infty} I(x', y')\delta((x' - x)^2 + (y' - y)^2 - R^2)dx'dy'. \tag{3.2}$$

As an example of this integral transform consider the three circle binary image of Figure 3.1 in which as the radius parameter R increases the maximum of the transformation is attained at the center of the different circles in the image.

3.2 Integral representation of the GHT

If we look at the integral representation in Equation (3.2) for the CHT and compare with the corresponding constraint Equation (2.4), a generalization for an arbitrary shape satisfying a constraint equation of the form of Equation (2.6) can be given by

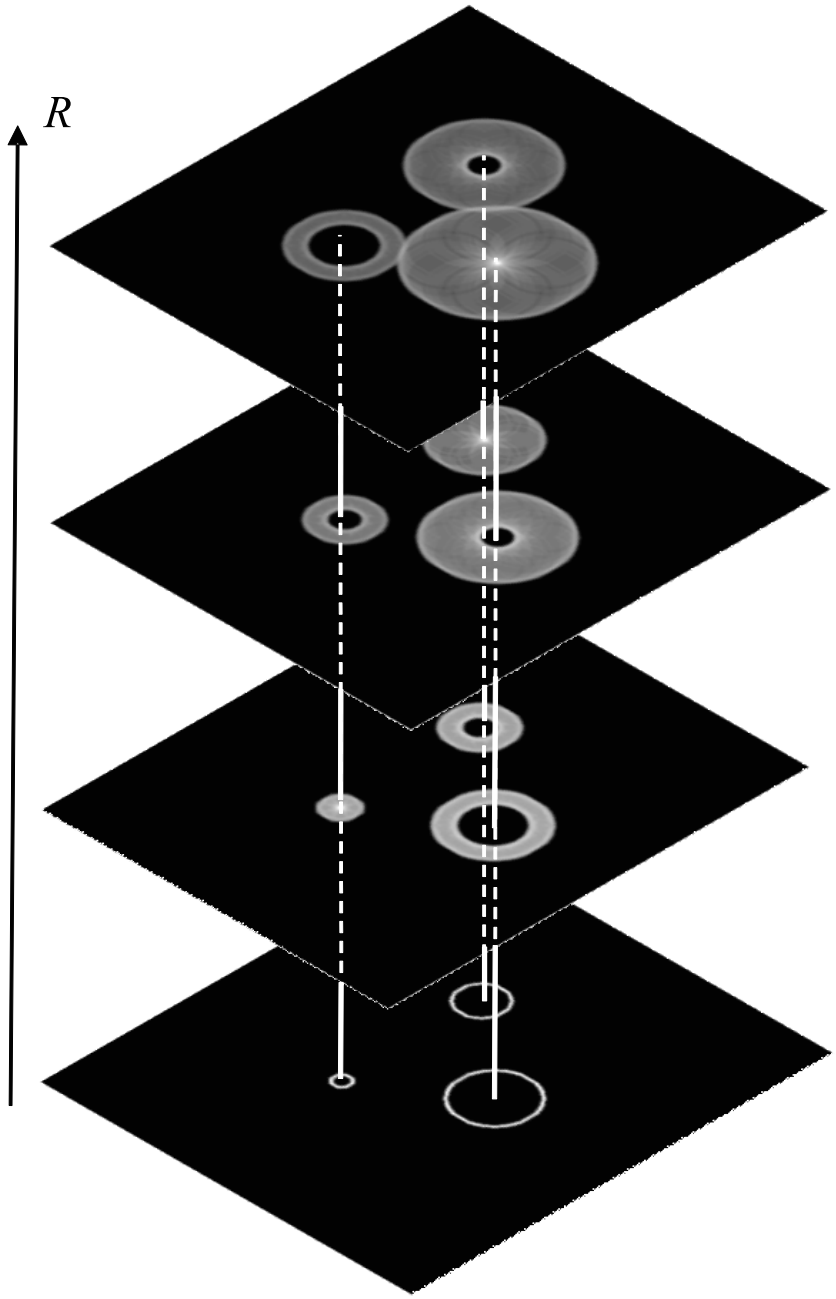

Figure 3.1: CHT of a three circle binary image for different values of parameter R.

[Hendriks et al., 2005]

$$H(x,y;s,\theta) = \iint_{-\infty}^{+\infty} I(x',y')\delta(f(x'-x,y'-y;s,\theta))dx'dy'. \tag{3.3}$$

Merlin and Farber [Merlin and Farber, 1975] and later Sklansky [Sklansky, 1978] noted the close connection between the GHT and the *template matching* algorithm as shown in the preliminary outlook of Section 2.3. A direct connection to this issue can be seen by noting that the integral representation of the GHT of a binary image $I(x,y)$ given in Equation (3.3), corresponds to a *correlation* whose kernel is given by the Dirac delta function $\delta(f(x,y;s,\theta))$. That is, the GHT corresponds to a correlation between the image and a template represented by the following constraint equation

$$f(x,y;s,\theta) = 0, \tag{3.4}$$

which only differs from the original Equation (2.6) in taking the origin as a reference point. In order to proceed into the optical implementation of the GHT, we consider a π rotation of the template, whose constraint equation is

$$f_\pi(x,y;s,\theta) = f(-x,-y;s,\theta), \tag{3.5}$$

and we can rewrite Equation (3.3) as

$$H(x,y;s,\theta) = \iint_{-\infty}^{+\infty} I(x',y')\delta(f_\pi(x-x',y-y';s,\theta))dx'dy', \tag{3.6}$$

which is exactly in the form of a *convolution* between the image $I(x,y)$ and the π-rotated template. As an example consider a simple test binary image of three points shown in Figure 3.2(a). For illustrative purpose, the triangle whose vertices are these points is overlaid in Figure 3.2(a-d) as dotted line. It can be clearly seen that for the kernel in the inset of Figure 3.2(d), corresponding to the π-rotated triangle, the GHT exhibits a maximum at the center of the dotted triangle, which corresponds to exact matching with the template. Figure 3.2(b-c) show partial matching cases corresponding to the π-rotated triangle but 1.5 times bigger and the triangle with the correct size but incorrect orientation, respectively.

The convolution form in Equation (3.6) is suitable for an optical implementation since the incoherent systems with which we will work are linear and invariant in the input intensity thus, by characterizing the response of the system to a point-like source, we will be able to obtain the overall response.

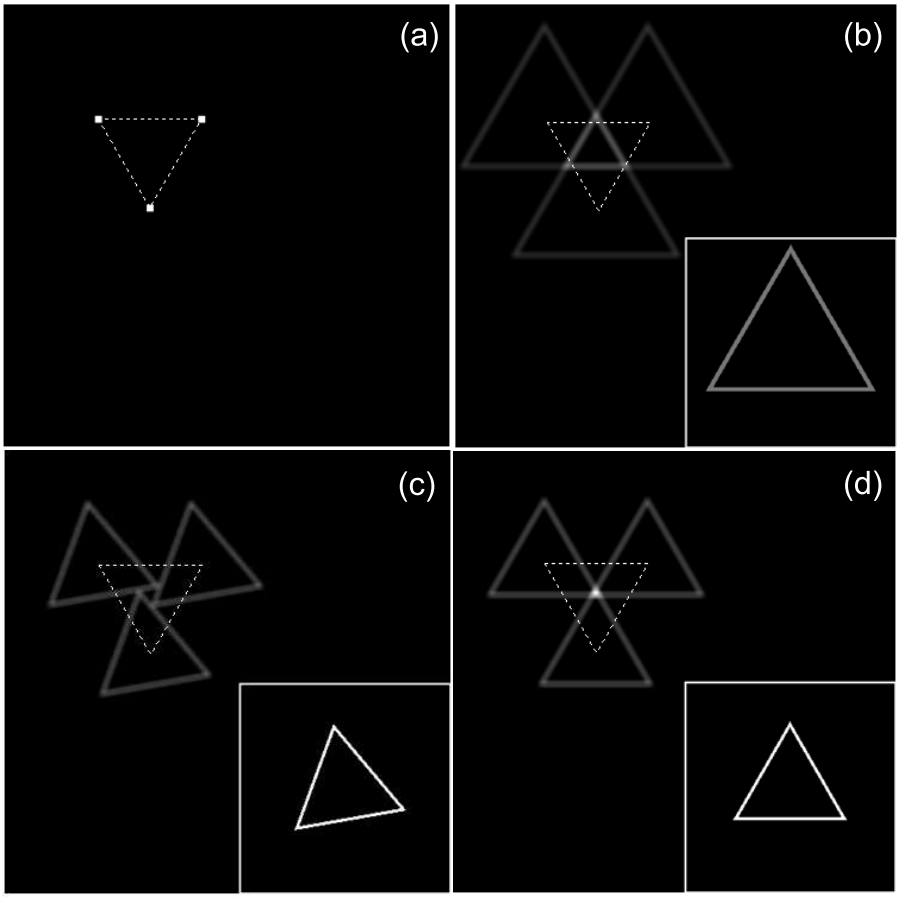

Figure 3.2: GHT of a three point binary image using a triangle template. (a) Three point test image. (b-d) GHT of (a) for the kernel shown in each inset. The triangle whose vertices are these points has been overlaid for illustrative purposes as dotted line in figures (a-d).

3.3 Shift invariant linear systems in optics

Analysis of optical systems in the space domain [Iizuka, 2008] is carried out considering the response $u(x_i, y_i)$ of the system to an input (in our case intensity input) in the object plane, where (x_i, y_i) are the coordinates in the image or capture plane and we will assume unit magnification, i.e. we will not take into account the possible inversion or change in scale (see further details in Appendix A). Consider an intensity point-like source placed at the origin of the input plane: $\delta(x, y)$ (Figure 3.3(a)). The response function or *Point Spread Function* (PSF) of the system is given by $h(x_i, y_i)$, that is

$$u(x_i, y_i) = h(x_i, y_i). \tag{3.7}$$

Consider now that the point source is moved from the origin to a point (x_0, y_0) in the object plane (Figure 3.3(b)). If the system is *shift-invariant* the response to this shifted source will only change its location but not its functional form, so the new response of the system is

$$u(x_i, y_i) = h(x_i - x_0, y_i - y_0) \tag{3.8}$$

(note that this condition does not generally hold for the entire input plane and we usually work in a small region of the input close to the optical axis, i.e. we work under the paraxial approximation). Let us finally consider an spatially extended source (Figure 3.3) g. This extended source can be regarded as a collection of point sources with an amplitude for the point at (x_0, y_0) given by $g(x_0, y_0)$. The response to this point source would correspond to

$$u(x_i, y_i) = g(x_0, y_0)h(x_i - x_0, y_i - y_0). \tag{3.9}$$

Considering that the system is *linear* in the input, the response to the complete source will be given by

$$u(x_i, y_i) = \iint_{-\infty}^{+\infty} g(x_0, y_0)h(x_i - x_0, y_i - y_0)dx_0dy_0, \tag{3.10}$$

which is exactly in the form of a convolution $(*)$ between the source $g(x, y)$ and the PSF $h(x, y)$

$$u(x_i, y_i) = g(x_i, y_i) * h(x_i, y_i). \tag{3.11}$$

Once the PSF of a shift-invariant linear system is known, the response of the system to an arbitrary source can be obtained through the convolution in Equation (3.11).

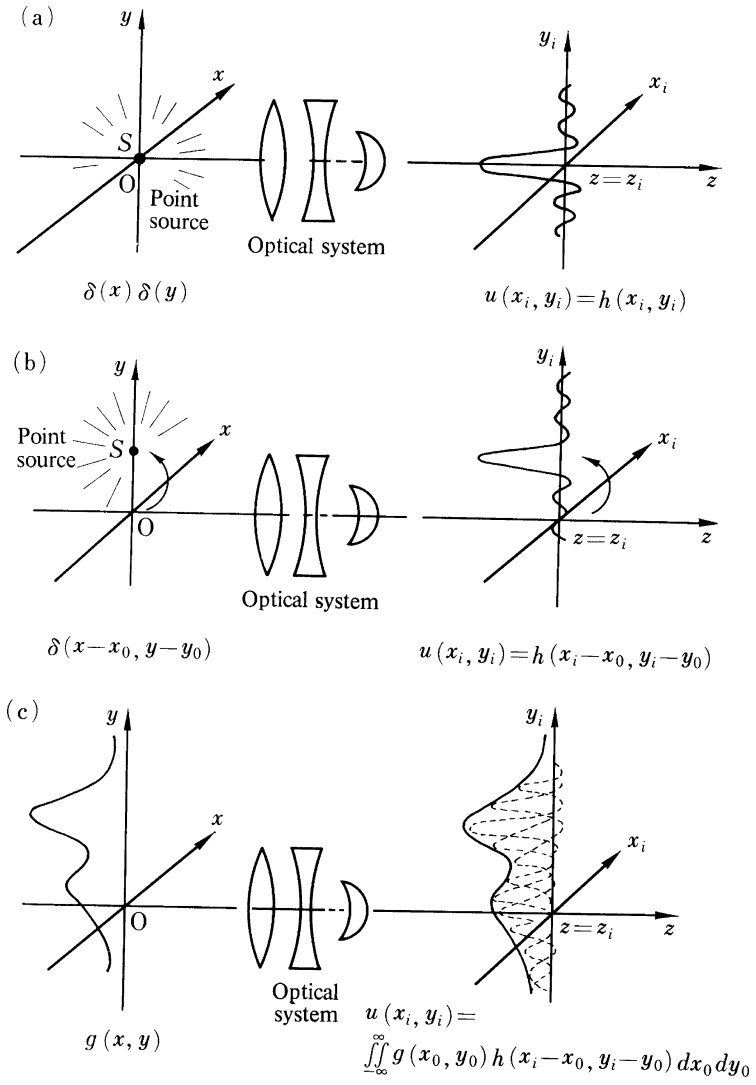

Figure 3.3: Point Spread Function of an Optical System. (a) Delta input at the origin (b) Shifted input (c) Spatially extended source (from [Iizuka, 2008]).

3.3.1 The search for a PSF

At this point, since the GHT for fixed scale and orientation can be expressed as a convolution, the comparison between Equation (3.11) and Equation (3.6) shows that that it is possible to achieve an optical implementation of the GHT by taking $h(x,y) = \delta(f_\pi(x,y;s,\theta))$ since in that case one generates an optical response $u(x,y) = H(x,y;s,\theta)$:

$$H(x,y;s,\theta) = g(x,y) * \delta(f_\pi(x,y;s,\theta)). \tag{3.12}$$

A physically reasonable approximation to the desired PSF can be achieved, for example, by means of a severely defocused optical system with a pupil whose transmittance is different from zero only along the desired template, since in a severely defocused incoherent system the (intensity) PSF is essentially the geometrical projection of the pupil onto the output plane (see Appendix A.2.2).

3.4 Incoherent Optical GHT

In order to obtain the desired PSF we propose the setup shown in Figure 3.4(a). The edge image to be processed is displayed in the object plane O and is illuminated by a totally (both temporal and spatial) incoherent source. The imaging lens system (L) is placed at distance d_1 from O. The aperture of this system is an opaque mask (M) with significant light transmission only across a thin curve emulating the desired (π rotated) edge template. The GHT is obtained at distance d_C from L on plane C which lies beyond the in-focus plane F.

As an example of the working principle, consider Figure 3.5(top) where the GHT of a three-point image (Figure 3.2(a)) is optically achieved. The triangle whose vertices are these points is overlaid at the object plane while its (in-focus) image is overlaid at the capture plane; note that the in-focus image is inverted (see Equations (A.2) and (A.3)) with respect to the object itself. As the capture plane C lies beyond the in-focus plane F, the geometrical projection of the pupil is also inverted with respect to the pupil itself, so it does not appear inverted to the in focus object over which the GHT is to be applied. Then, for Equation (3.12) to be valid we would need the pupil to represent the π rotated edge template.

Alternatively, we can work with a non-rotated pupil as shown in Figure 3.4(b) but the GHT is obtained before the in-focus plane as the example for a triangular pupil shows in Figure 3.5(bottom). An application of this configuration can be found in Section 5.1 and its implementation in Section 5.3).

In our experimental setup the O plane is a liquid-crystal display (LCD) illumi-

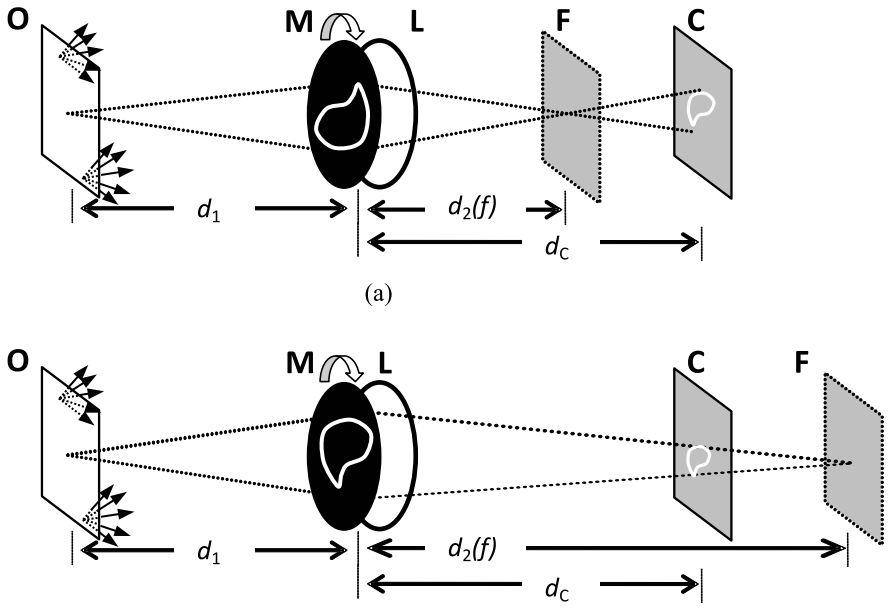

Figure 3.4: (a) Optical implementation of the GHT on plane C *after* in focus plane. O: object plane; M: rotating binary mask; L: imaging lens system; F: in-focus plane. (b) Alternative implementation of the GHT on plane C *before* in-focus plane F. Note that the pupil represents the desired template (no rotation).

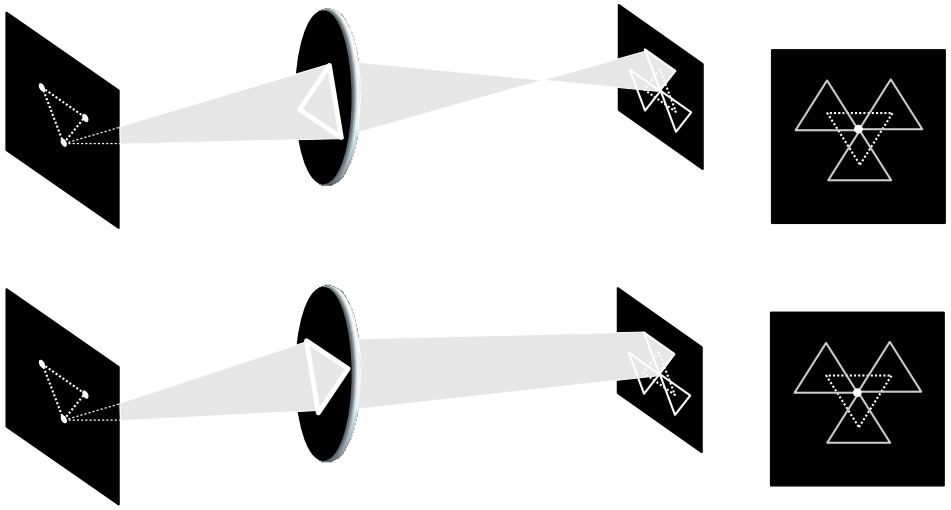

Figure 3.5: Optical implementation of the GHT of Figure 3.2(a) following the configuration of Figure 3.4(a) (top) and the configuration of Figure 3.4(b) (bottom).

nated by an array of white LEDs. The imaging system (L) is a doublet formed by an electrically tunable lens (Optotune EL-10-C[1] focal range $80-230mm$ for currents between $300mA$ and $10mA$) with variable focal length f placed in contact with a $f_C = 16mm$ fixed focal length lens. For an arbitrary focal length f the Gaussian imaging equation [Iizuka, 2008, Goodman, 1996] determines the in-focus plane position $d_2(f)$

$$\frac{1}{d_1} + \frac{1}{d_2(f)} = \frac{1}{f_{eff}(f)} \sim \frac{1}{f} + \frac{1}{f_C}, \tag{3.13}$$

where $f_{eff}(f)$ is the effective focal length of the doublet combination (see for example [Jenkins and White, 1957]). For the focal length f that verifies $d_2(f) = d_C$, the in-focus plane F coincides with C. For the capture plane to always lie beyond the in-focus plane (i.e. to always work under the configuration of Figure 3.4(a)) we choose $d_2(f_{max}) = d_C$ (which is achieved for the minimal current through the lens) so that for increasing currents the capture plane still lies beyond[2]. The effective size of the rotated template on the C-plane increases as $d_2(f)$ decreases (i.e. F moves towards L) so we can control the scale parameter s by varying the focal distance f.

Parameter θ is controlled by mounting the aperture mask M on a rotatory stage as shown in Figure 3.6(b) (or by using a rotating Dove prism placed in front of the LCD as in [Steier and Shori, 1986] or by displaying the rotated mask in a high contrast LCD as will be shown later in Section 4.3.2). The aperture mask M of the order of $5mm$ in size was printed as a binary pattern on a glass cover [alternatively it might be displayed on a high contrast LCD, see Section 4.3.1 and Section 4.3.2]. Images were acquired at fixed distance $d_C \sim f_C = 16mm$ with a digital camera DC310 (Thorlabs), 1024×768 pixels, $4.7\mu m$ pixel size.

3.4.1 Preliminary results

Although the proposed setup might be used for any template of interest (i.e. an arbitrary template including scale variation and orientation at the same time), in the next we show the working principle of the proposed method with circles and triangles.

3.4.1.1 Circle Hough transform

To test the feasibility of our optical approach we started by considering a simple, symmetric pupil and implemented the CHT [Fernández and Ferrari, 2015]. The

[1] http://www.optotune.com/products/focus-tunable-lenses/electrical-lens-el-10-30-c

[2] alternatively, we might allow the system to operate as in Figure 3.4(b) and take into account the change in pupil orientation when passing through the focal plane

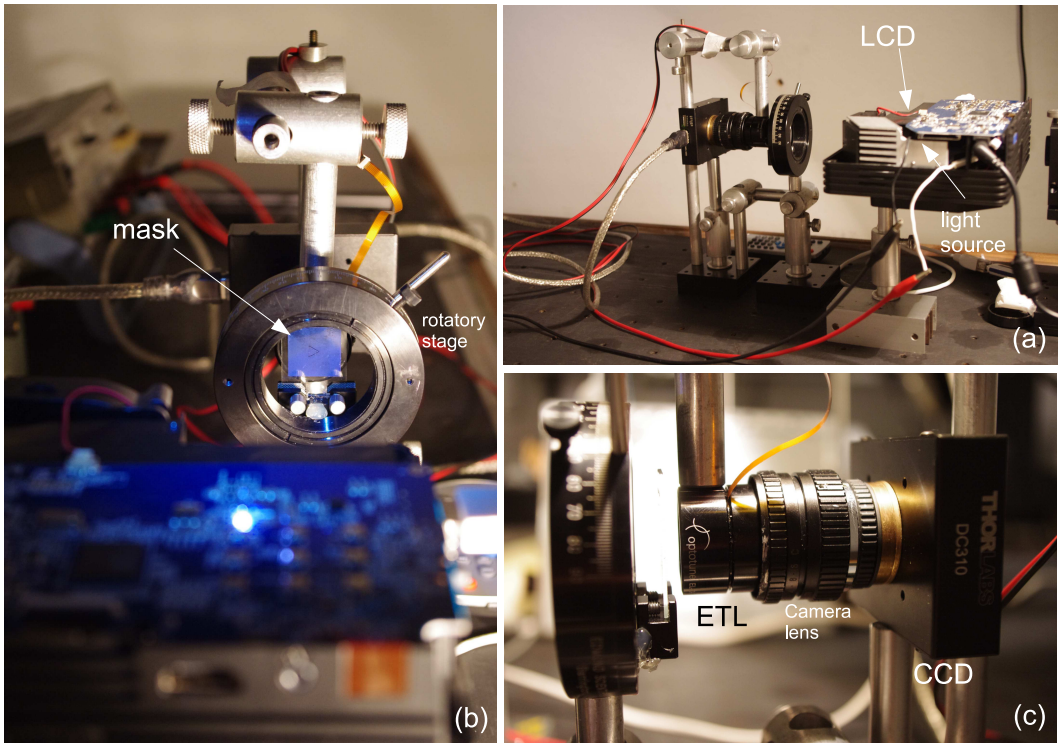

Figure 3.6: Pictures of the experimental setup (a) Lateral view of the setup with the LCD and its illumination source; (b) Front view of the setup where the rotating pupil mask M can be clearly seen; (c) detail of the imaging system L and CCD acquisition camera.

analytical expression for this transformation follows Equation (3.2). Figure 3.7(a) shows an image of three binary circles in which we want to detect a circle of specific radius (and rule out those with different radii) by applying the optical CHT. The results of transforming the image under CHT for different radii are shown in Figures 3.7(b-d) and represent the actual capture on the camera of the system with no post-processing. Note the close resemblance with the simulation results in Figure 3.1. It can also be clearly seen that the CHT exhibits an intensity peak at the center of the circle whose radius coincides with the radius R of the transformation template, which in turn can be varied by changing the focal length of the tunable lens, i.e. by changing the size of the projection of the pupil mask. By conveniently thresholding the GHT we can separate the center of any circle of radius R (within scaling error, see Section 3.4.2.2) from the original image, which could be potentially useful for segmenting (and eventually tracking) the desired contour.

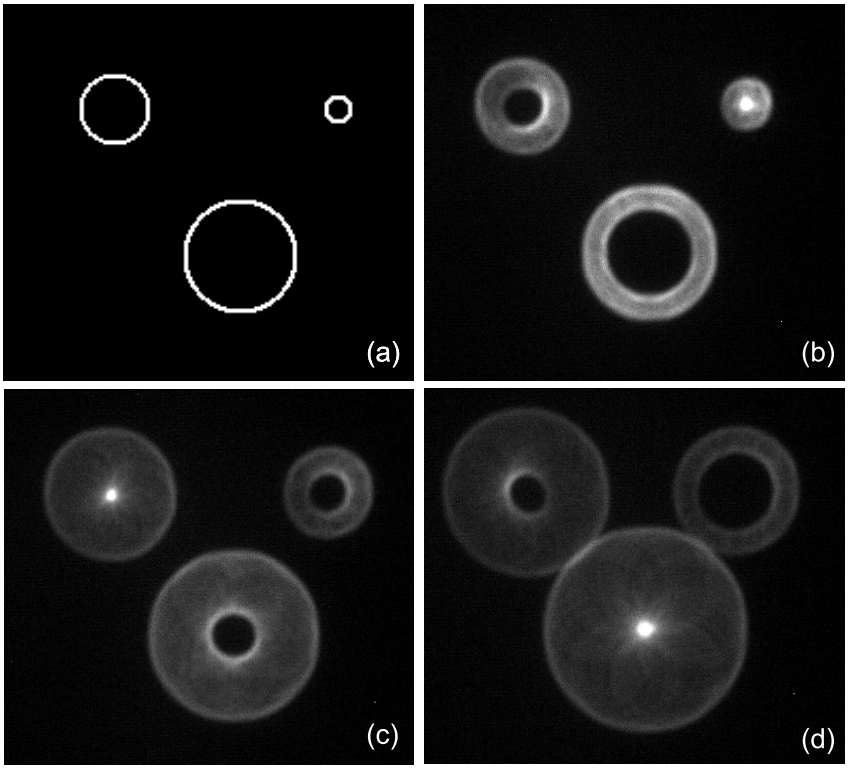

Figure 3.7: Recognition of a circle of given radius R in an image of three binary circles of radius R_1, $R_2 = 3R_1$, and $R_3 = 5R_1$. (a) original image; (b-d) transformed image on the plane C (as captured by the camera, no post-processing) detecting as bright points the centers of circles in original image with $R = R_1$, R_2, and R_3, respectively

3.4.1.2 Orientation variant detection

We tested our setup with an orientation-dependent template as it is the case of a triangle. Figure 3.8(a) shows the test image in which the desired template is to be found (all triangles considered are of the same size just to select a given orientation). The upper left corner of Figure 3.8(b-e) shows the orientation of the template (pointing down, up, right and left, respectively) used to detect a triangle pointing up, down, left or right in the original image. From the symmetry of the original image the GHT for each orientation is expected to be a rotation of any of the other. The results obtained in Figure 3.8(b-e) show that this is actually the case. The reference point of each triangle is a clear bright spot that might be easily thresholded. So, under the appropriate orientation, the system is capable of detecting an arbitrary template (within the error in orientation, see Section 3.4.2.2).

3.4.2 Performance study

We will firstly assess the real-time performance capability of our system. Then we are going to determine the error in scale and orientation parameters for a detected peak under an optimal input. Finally, we test the method for a real scene.

3.4.2.1 Real-time execution

A real-time demonstration of scale variation in GHT can be seen over the moving circles of Visualization: 3Circles, where we illustrated the possibility of varying the scale parameter and obtaining at the same time the GHT. The bottleneck for the real-time realization is imposed by the maximum acquisition rate of the camera used in the setup, which in our case is $30Hz$ at full resolution (1024×768). In comparison, the execution time for the circle HT implemented on a GPU [Ujaldón et al., 2008] is $123ms$ for a 1024×1024 image with optimum angle discretization (i.e. computation of votes at full resolution); thus, a real-time application based on this computationally implemented HT is limited at best to $8Hz$ video operation rate. Then, the proposed optical processor seems to be especially advantageous for real-time processing of high-speed video sequences.

3.4.2.2 Parameter error

Parameter θ is well defined within the precision $\delta\theta \sim 1^{o}$ of the rotatory stage. On the other hand, the primary source of error in our setup comes from the possibly incorrect determination of focal distance f which affects the scale parameter s. Following the geometric optics construction of Appendix A.2.2.1, the scale factor (i.e. the ratio

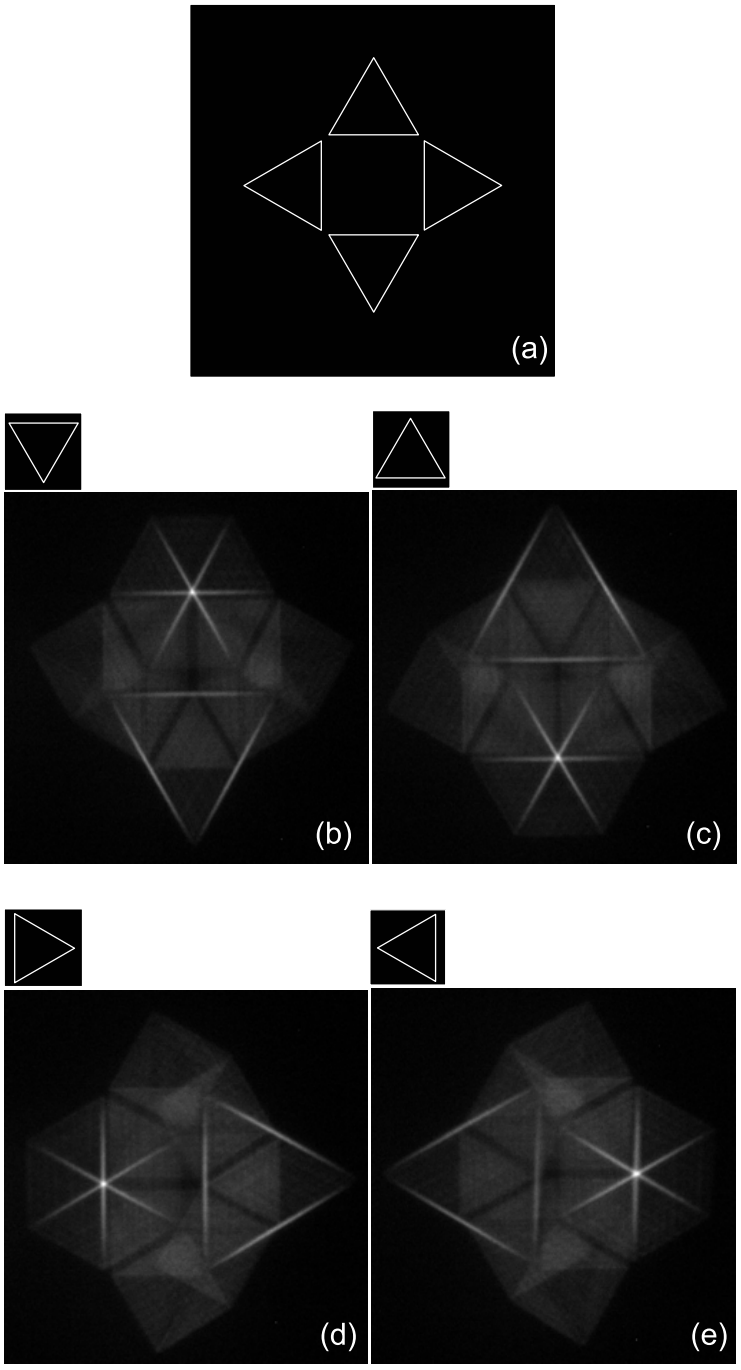

Figure 3.8: Recognition of a triangle in different orientations. (a) original image; (b-e) transformed image (as captured by the camera, no post-processing) detecting reference points of triangles pointing in the up, down, left and right orientations, respectively. Upper left corner of (b-e) shows the corresponding pupil mask.

between the size of the image of the pupil and its actual size) can be obtained from Equation (A.21)

$$s = d_C \left| \frac{1}{f} - \frac{1}{d_1} \right|, \tag{3.14}$$

so its relative error results

$$\frac{\delta s}{s} = \left| \frac{d_1}{d_1 - f} \right| \frac{\delta f}{f}, \tag{3.15}$$

e.g., for $f = \frac{d_1}{2}$ the relative error in the scale parameter is twice the relative error in the focal distance $\frac{\delta f}{f}$, which in our setup can be kept below 5% according to the manufacturer.

3.4.2.3 Natural scenes

To test the proposed method in natural images we considered next the circle detection in Figure 3.9(a). The circle we wanted to detect (a pencil holder viewed from above) is partially occluded and the background is textured. Over the luminance image we perform a previous edge enhancement transformation (Sobel operator [Sobel and Feldman, 1968]) which renders the grayscale image in Figure 3.9(b). In this regard, as the image itself is not binary, the transformation that we perform corresponds to a generalized Radon transform [Hendriks et al., 2005]. The result obtained on the plane C is shown in Figure 3.9(c), where the radius parameter was set to detect the circle with its center marked by a green arrow. A bright spot marks the center of the circle and might be easily separated from the image by thresholding in Figure 3.9(c).

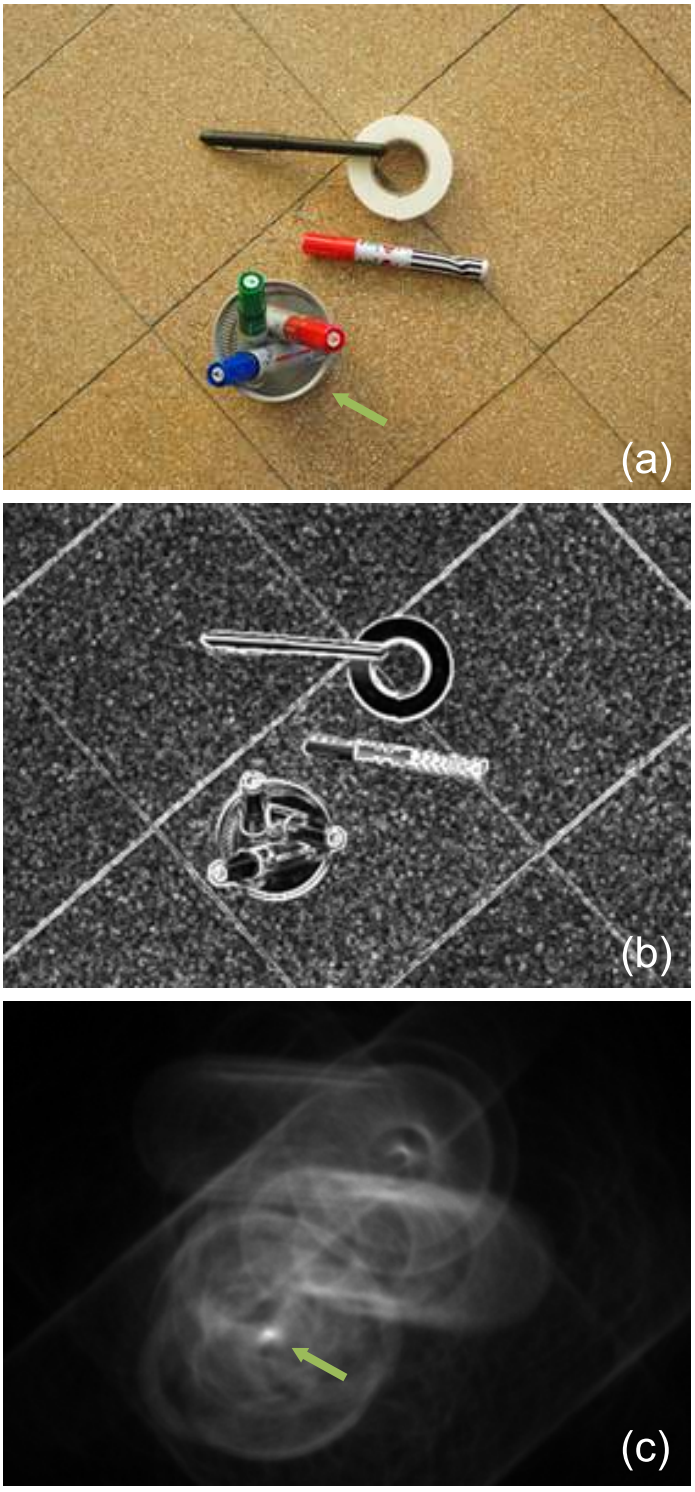

Figure 3.9: Recognition of a circle in a natural image (a) original image (partially occluded circle of interest marked by green arrow); (b) edge enhanced version of the gray scale image under Sobel operator; (c) GHT acquired on plane C: detection of the circle of interest (as captured on camera, no post-processing) with its center marked by the green arrow.

Chapter 4

Pattern recognition using the optical generalized Hough transform

It is expected from a pattern-recognition device to be able to recognize any given template, regardless of its position in the image, its orientation or its size or scale of magnification [Bone et al., 2006]. By combining the Fourier Transform capability of a 4f system and convenient geometrical transforms, Casasent and Psaltis [Casasent and Psaltis, 1976] were able to perform scale and rotation invariant detection in a coherent optical correlator. However, the result of this Fourier-Mellin correlator is independent of the form factor of the template, so a square appears to be the same as a rectangle to this transform.

As in any correlation optics application, the shift-invariance of the system presented in Chapter 3 allows for parallel processing of all the parts of an image at a time. However, the system is scale-variant and orientation-variant. So, research efforts should be directed towards the development of multiplexing (spatial, temporal) strategies to overcome these issues.

The robustness of our method under different perturbations of the input: noise, low contrast, and degradation of the feature of interest is another key point to validate its pattern recognition capability. We will so start by considering an ensemble of different perturbations over synthetic input images in order to study the performance of the Generalized Hough Transform (GHT).

4.1 Performance under noise, low contrast or image degradation

An intensity peak can be clearly seen at the center of the geometrical feature that coincides with the template in shape, size and orientation. To test the robustness of the detection capability of our method [Fernández, 2016b] we simulate noisy inputs at the object plane considering for example Additive White Gaussian Noise (AWGN) of null mean (see Figure 4.1). Even under strong noise conditions like in Figure 4.1(c) (where noise standard deviation is 40% of the maximum value of the signal) the intensity peak of the transformation can still be clearly seen. This is due to the incoherent nature of the implementation of the GHT for which noise at the input is averaged over the entire field of view of the image plane.

Besides noise we can also consider how the performance of the method would be affected by a contrast loss in the input. Figure 4.2 shows the effect of noise for an image with a contrast loss of 75% with respect to Figure 4.1(a).

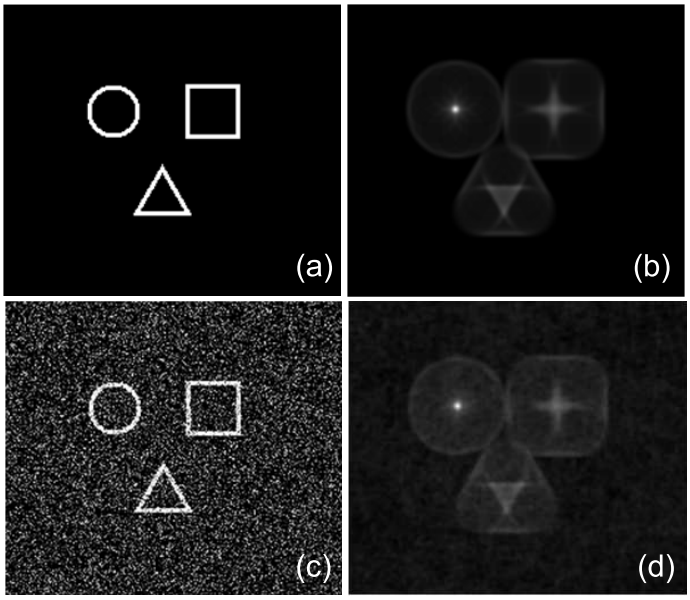

Figure 4.1: (a) Original binary image with no noise (black=0, white=1); (b) GHT of (a) with annular template; (c) degraded version of (a) with AWGN of null mean and $\sigma_{noise} = 0.4$; (d) GHT of (c).

Another issue to take into account in the assessment of robustness of the method is its performance under degradation in the input. We simulated this degradation by considering "pepper" noise, i.e. with probability p each edge (white) point is substituted by background (black). In Figure 4.3 the effect for $p = 0.2$ is shown.

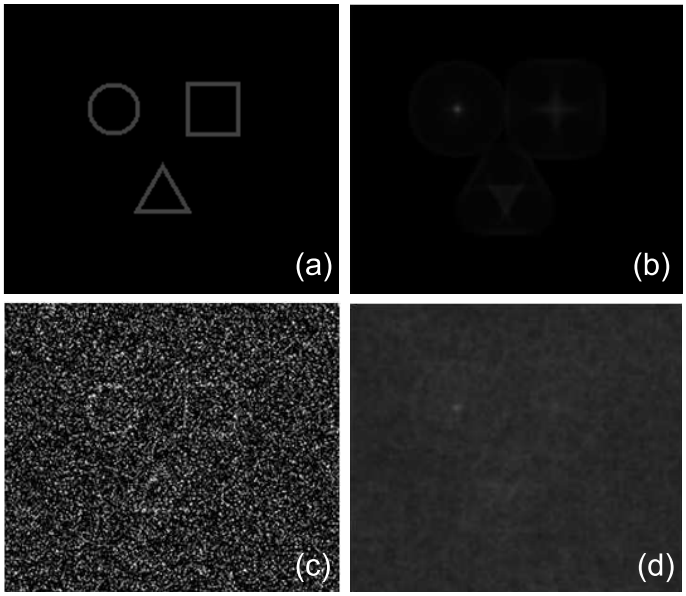

Figure 4.2: (a) Original binary image with no noise (black=0, grey=0.25); (b) GHT of (a) with annular template; (c) degraded version of (a) with AWGN of null mean and $\sigma_{noise} = 0.4$; (d) GHT of (c).

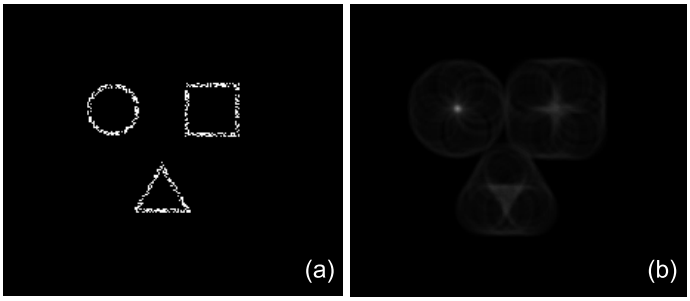

Figure 4.3: (a) Original binary degraded image with $p = 0.2$ (b) GHT of (a).

We can give a quantitative assessment of the previous issues by measuring the sharpness of the peak of GHT. This is done by means of the Peak-to-Correlation Energy (PCE) of the system [Kumar and Hassebrook, 1990]

$$PCE = \frac{max(GHT)^2}{\int_{-\infty}^{+\infty}\int_{-\infty}^{+\infty} GHT^2(x,y)dxdy}. \tag{4.1}$$

(alternatively, other indicators of correlation accuracy under matched filtering can be found in [Awwal, 2010]). The results for the PCE under different levels of noise in the input and full contrast are depicted in Figure 4.4. We can see that the performance of the method is almost invariant for noise levels up to roughly 20% of signal level. For a contrast loss of 75% (Figure 4.5) the performance is almost invariant for noise up to 15% of signal level. In Figure 4.6 the result for the performance under degradation of the input is shown and it can be seen that the performance is almost invariant for substitution probabilities up to $p = 0.5$ approximately (similar dependence of PCE against p holds for contrast loss up to 50%).

The robustness of the peak detection capability under different perturbations is a key step for its validation as a pattern recognition tool. In the following we present some pattern recognition applications [Fernández et al., 2015b] and temporal multiplexing strategies for dynamic scale and orientation- variant detection. For the sake of simplicity we show scale and orientation changes in separated examples but of course the strategies can be combined.

4.2 Multiple target recognition

4.2.1 Red blood cells counting

In a first series of experiments we show the capability of the proposed system to achieve multiple target detection. We used an image of red blood cells (RBCs) shown in Fig. 4.7(a) , with the purpose of obtaining automated cell counting. RBC counting is an important task [Tomari et al., 2014] since RBCs contain hemoglobin, which in turn carries oxygen to the body's tissues, so the number of RBCs (per liter blood) is a measure of how much oxygen the tissues are receiving. As input to our optical system we generated an edge image (see Figure 4.7(b)) by applying an edge enhancement operator, e.g. Sobel operator , to the original image (the preprocessing of the original image to achieve an edge-image is a necessary operation also for the computational implementation of the Hough transform). Normal RBCs have minimal anisocytosis, i.e., they have approximately the same size (normal RBCs are in the range $6.2 - 8.2\mu m$) and deviates slightly from a perfect round appearance.

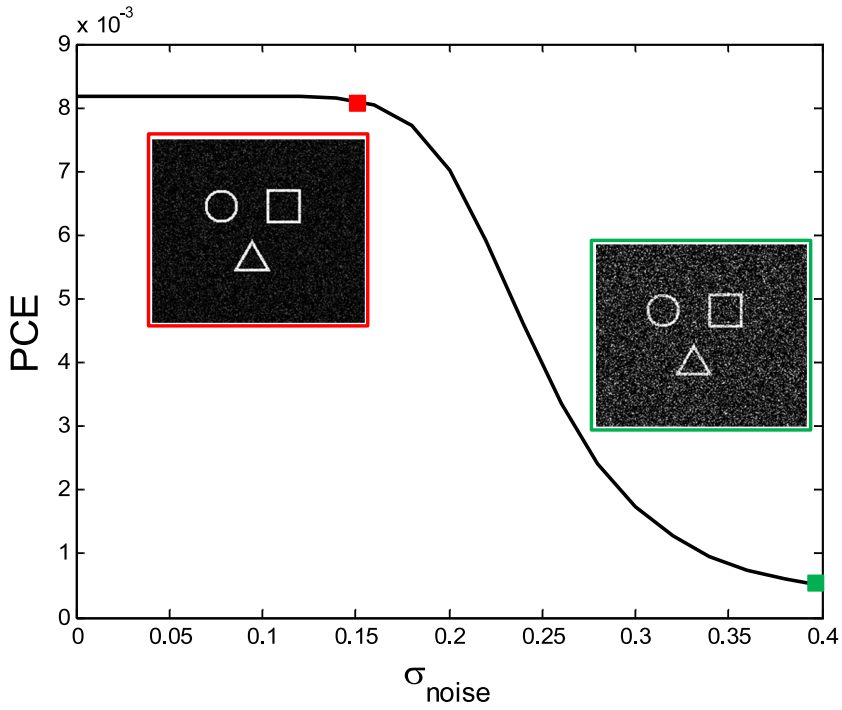

Figure 4.4: PCE against σ_{noise} for full contrast in the input (1000 rounds average)

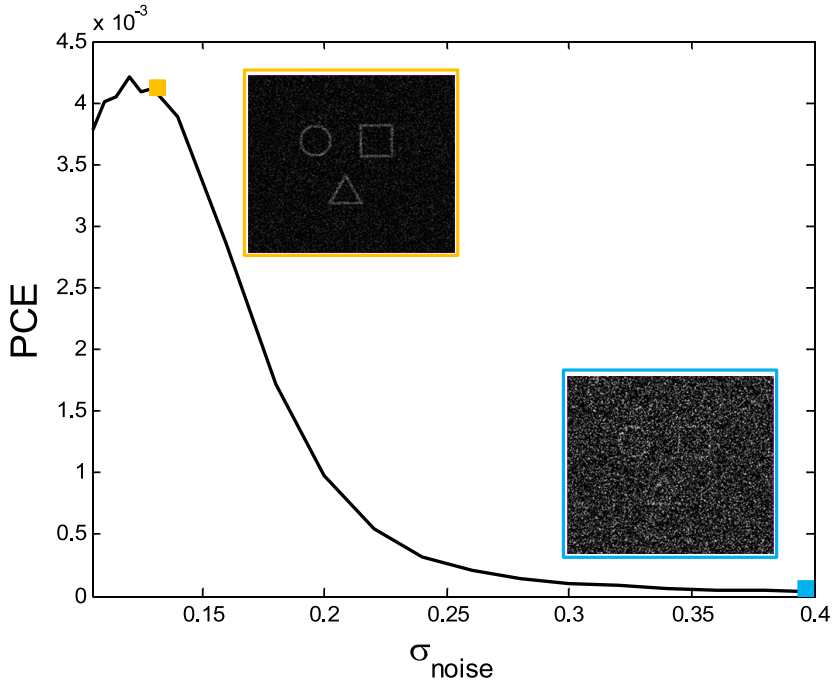

Figure 4.5: PCE against σ_{noise} for a 75% contrast loss in the input (1000 rounds average)

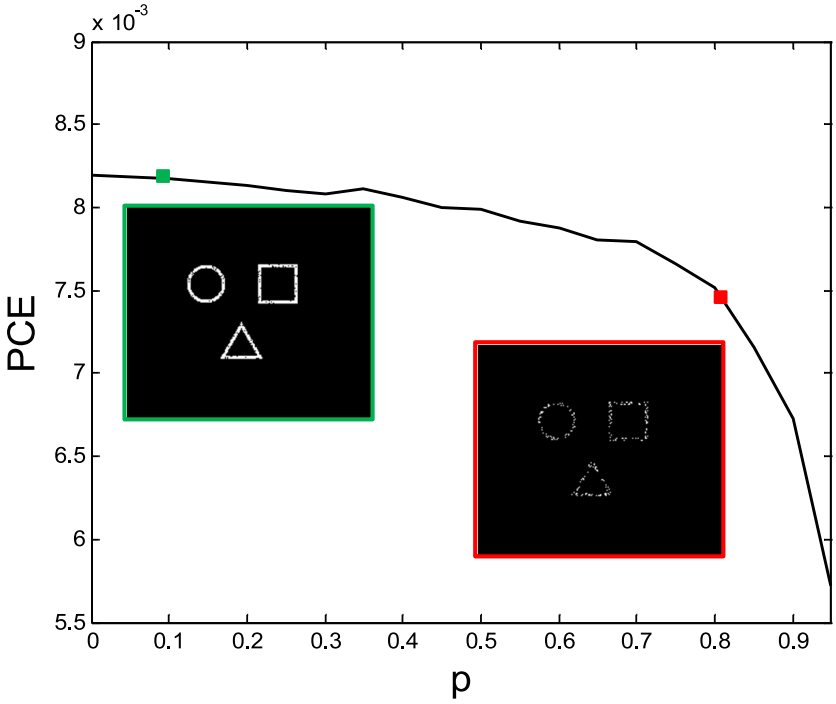

Figure 4.6: PCE against p (1000 rounds average)

Thus, for simultaneous detection of multiple RBCs we can utilize a single annular aperture whose diameter is adapted to the mean diameter of the RBCs under study. The required diameter of the projection of the pupil can be adjusted with the help of the Electrically Tunable Lens (ETL).

Figure 4.7(c) shows the optical Hough transform obtained with our setup and Figure 4.7(d) shows the binarization of the local maxima by using adaptive intensity thresholding. Since there is one local point-like maximum per cell, from the binarized image in Figure 4.7(d) it is easy to count cells utilizing standard image tools, e.g. by labeling the connected regions and counting the number of labels. In our case the cell counting gives 21 ± 2 units. The relatively large number uncertainty is due to the fact that some cells are at the borders of the image (and/or only partially included in the image) so their centers do not fall within the field of view of the system.

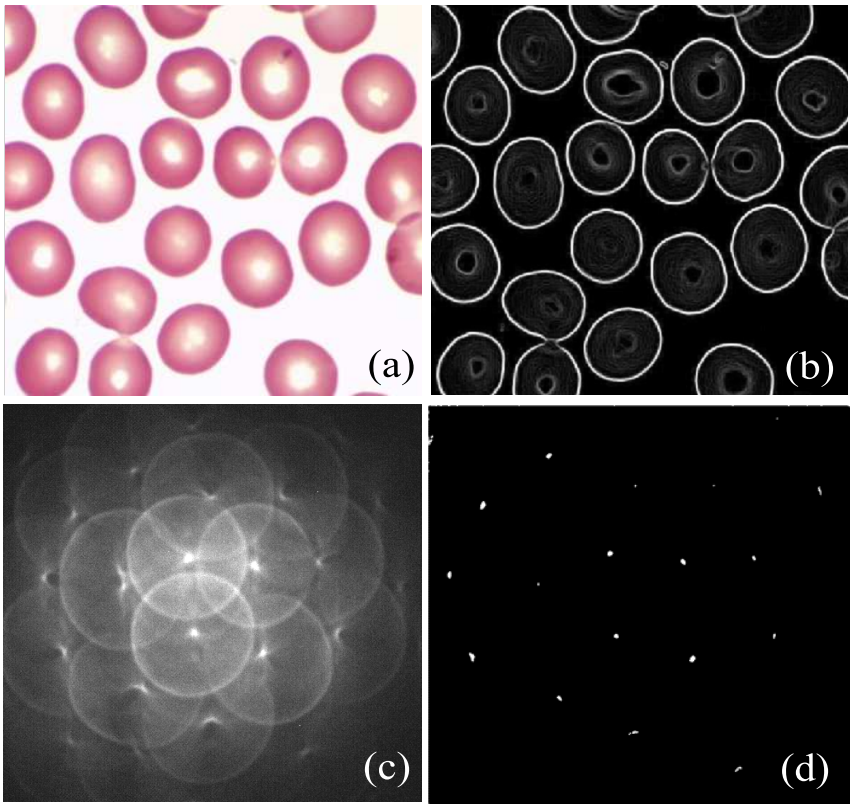

Figure 4.7: (a) Red blood cells; (b) edge image; (c) optical Hough transform; (d) binarization of the Hough transform maxima by intensity thresholding.

4.2.2 Real-time droplet velocimetry in microfluidics

The main advantage of an optical GHT in comparison with computational approaches is that it works in real-time (i.e. only limited by the frame rate of the acquiring camera). Thus, the proposed GHT is in principle a useful tool to study dynamic processes, e.g. droplets velocimetry in microfluidics. Figure 4.8(a) is an excerpt from the video kindly provided by Th. Cubaud which is related to the work described in [Jose and Cubaud, 2012]. It shows a train of droplets (with a characteristic diameter $250\mu m$) coming out from a microchannel that is connected to a diverging chamber. Droplets are made of a water/glycerol mixture and the continuous phase is composed of silicone oils. The complete microfluidic setup and an analysis of the droplets dynamic are described in [Jose and Cubaud, 2012]. Figure 4.8(b) shows an edge image obtained by applying an edge enhancement operator, e.g. Sobel operator, to the original image shown in Figure 4.8(a). Figure 4.8(c) (which is an excerpt from Visualization: Droplets) shows the optical Hough transform obtained with an annular aperture whose diameter (projected on the C-plane) matches the droplet diameter. In the same figure the inset depicts a plot of the mean light intensity (over the area enclosed by a white square) in terms of frame number. The peak of intensity in the plot indicates the passage of a maximum of the Hough transform (i.e. the center of a droplet). By obtaining the time delay between peaks we are able to give an estimation of the change in droplet flux in the chamber. The flux varies between 1 droplet every 23 frames at the beginning to 1 droplet every 13 frames at the end of the sequence. This roughly twofold increase in particle flux is in good agreement with the change in droplet fluid flow rate from 14 to $30\mu l/min$ reported in [Jose and Cubaud, 2012].

4.3 Temporal multiplexing strategies

We introduce some improvements (see Figure 4.9) over the optical setup originally presented in Section 3.4. These improvements allow for the continuous variation over time of the scale and orientation parameters of the template to be matched and consequently allow for the implementation of efficient schemes of varying scale or orientation detection under temporal multiplexing.

4.3.1 Scale variant detection

In the present experiment we controlled the electrical lens with a ramp generator, so that we generate a continuous change of the template scale. The control of the focal length of the ETL allows adjusting the scale of the pupil projected on the C-plane,

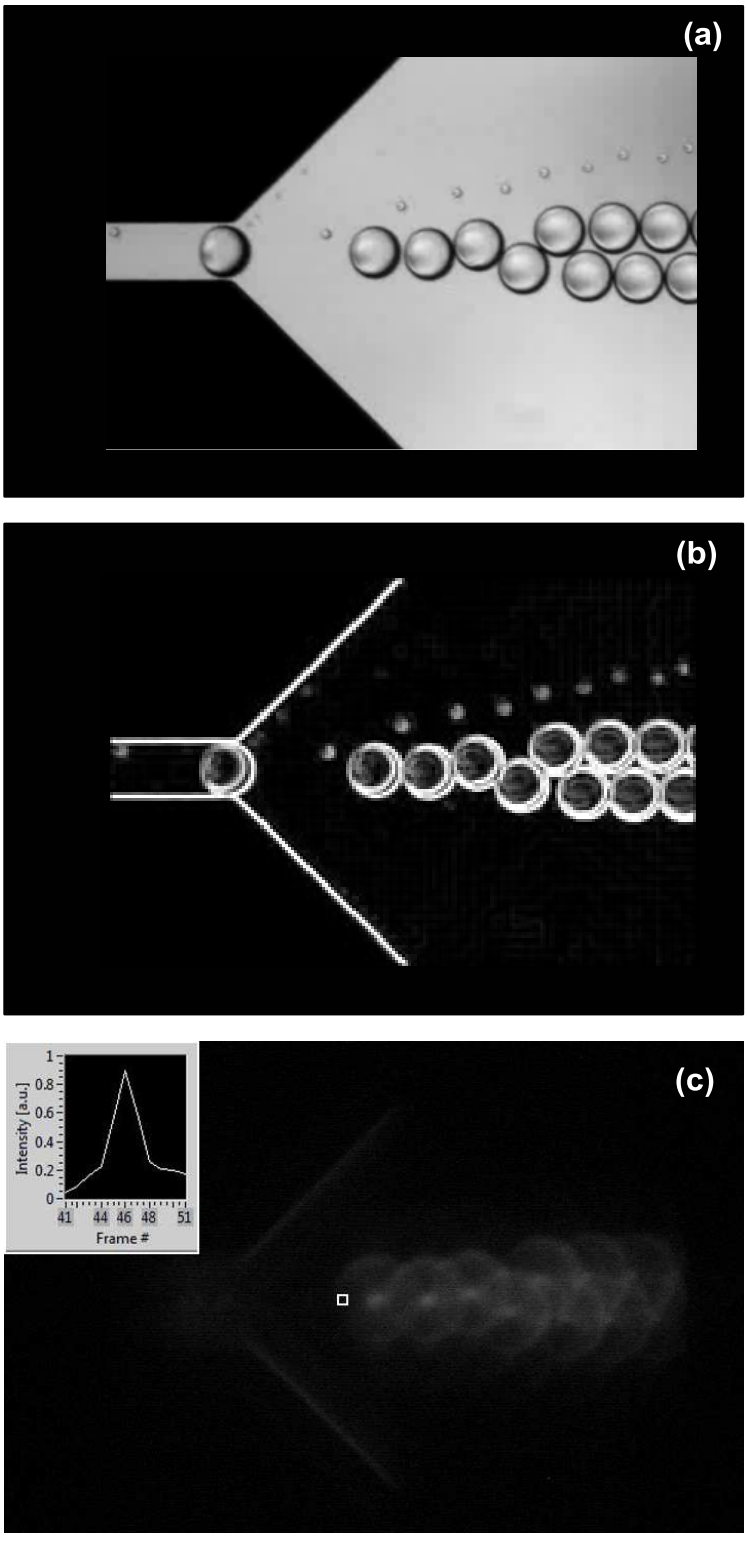

Figure 4.8: (a)Droplet chamber; (b)edge-image; (c)optical Hough transform and intensity peak detection (excerpt corresponding to frame N^o51 from Droplets).

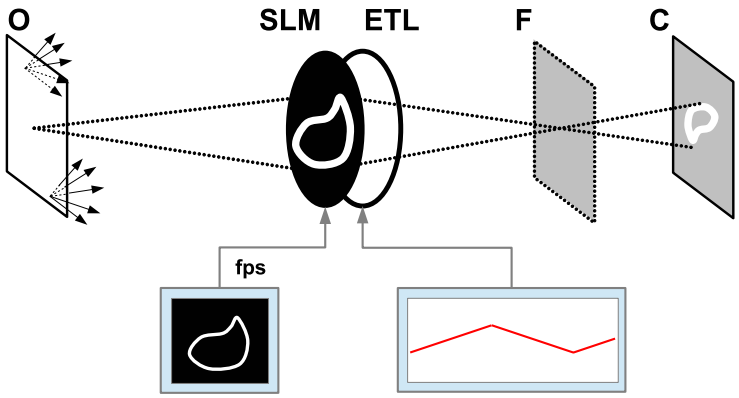

Figure 4.9: Modified setup in the optical implementation of the GHT on plane C. O: object plane; SLM: Spatial Light Modulator; ETL: Electrically Tunable Lens system; F: in-focus plane.

and the temporal variation of the template scale can be used to follow the evolution of a dynamic process, or equivalently, to determine the relative size of several targets at a fixed time.

In order to illustrate this application, we performed a series of experiments with an image of a cell-culture (bacteria) in presence of different antibiotics in a Petri dish. Several $6mm$ filter paper disks impregnated with a known concentration of different antimicrobial compounds are placed in the cell-culture. The purpose of the procedure called Kirby-Bauer disk diffusion susceptibility test[1] is to determine the sensitivity of bacteria to various antimicrobials by measuring the radius of the inhibition disks generated around the impregnated paper disks. The measure of the different radii is usually done manually.

The purpose of our experiment is to achieve an automated determination of the diameters of the different diffusion disks using the GHT with an annular pupil. Figure 4.10(a) shows the original image of the Petri dish with the cell-culture and the impregnated paper disks. Figure 4.10(b) shows the corresponding edge image (generated by Canny operator [Canny, 1986]) which is displayed in the LCD placed in the O-plane of our experimental setup. Figure 4.10(c) shows the GHT for the minimum radius considered, that is the paper disk radius. In the inset, the PSF (whose radius equals the minimum radius, i.e. the radius of the paper disks) is depicted. Bright spots in Figure 4.10(c) identify the centers of all the paper disks. As the pupil radius varies with time, one obtains a maximum of the Hough transform

[1] http://www.microbelibrary.org/component/resource/laboratory-test/3189-kirby-bauer-disk-diffusion-susceptibility-test-protocol

at the center of the culture whose radius matches the radius of the PSF at that time. Figure 4.10(d) shows the result for the biggest inhibition disk (in the inset, PSF with the corresponding radius). As this match corresponds to a PSF four times bigger in radius than the minimum, we inferred that the culture has a $24 - mm$ inhibition disk. In this way, different measures over a given image are codified in the time sequence of the experiment (Visualization: Disk Diffusion), i.e. we achieve scale variant detection through temporal multiplexing.

4.3.2 Orientation variant detection

We can also vary the orientation of the template in order to obtain orientation variant detection as a function of time. This is achieved by displaying a video sequence (with a different orientation of the target in each frame) on the LCD which acts as pupil in the setup of Figure 4.9.

To illustrate this application we consider a static image of 3 unicellular organisms called diatoms, of nearly triangular shape and similar size but different orientation (Fig. 4.11(a)[1]). Figure 4.11(b) shows the result of applying Sobel operator to generate the edge image. The scale parameter is set to match the size of any of the diatoms and we vary the orientation of the template in the different frames of a video sequence. The inset of Figure 4.11(c) shows the PSF of the system for a given orientation, which matches the diatom in the upper right corner of Figure 4.11(a). The video in Visualization: Diatoms includes a temporal sequence covering the matching of every diatom of the original image. The matching orientations give a bright spot at the center of the corresponding object in different frames of the sequence. In this way, rotation-variant detection can be achieved by extracting the different matches from the video.

Through the previous series of experiments, it can be clearly seen the applicability of the optical generalized Hough transform in pattern recognition tasks. By temporal multiplexing, we are able to achieve scale and orientation changes and we can extract the matching results for different parameters from a video sequence which is only limited by the frame rate of the display and capturing devices.

[1] http://ancientpoint.com/imgs/a/g/c/i/j/3_x_early_diatom_microscope_slides_4_lgw.jpg

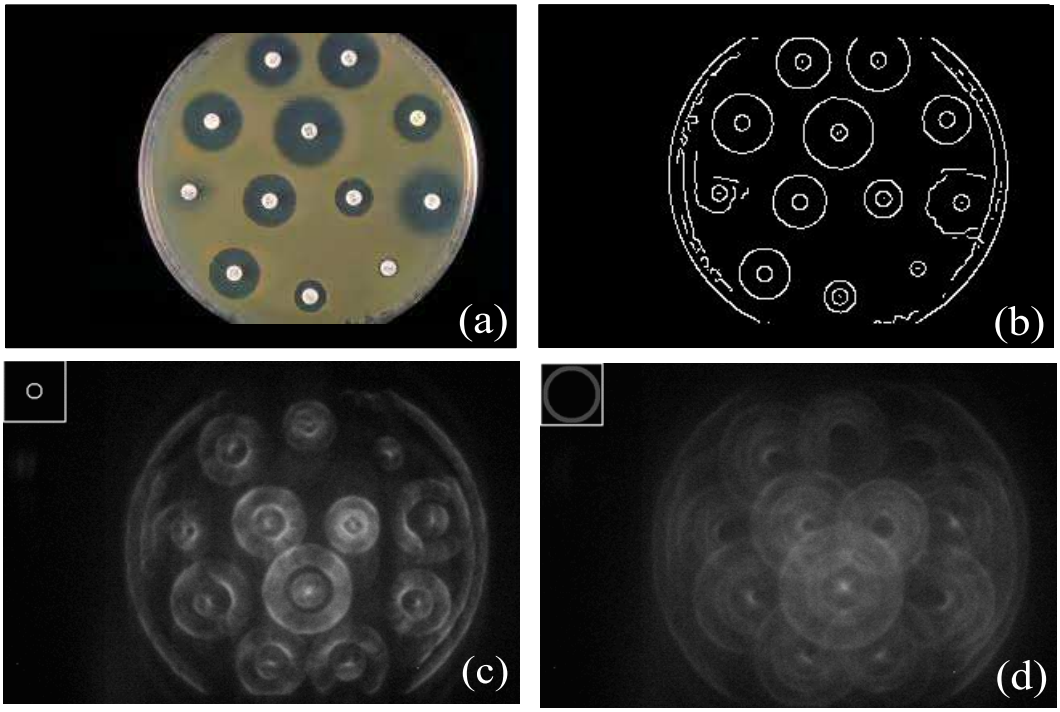

Figure 4.10: (a) Disk diffusion original image; (b) edge-image; (c-d) optical Hough transform for the minimum and maximum radius in the image (excerpts from Visualization: Disk Diffusion).

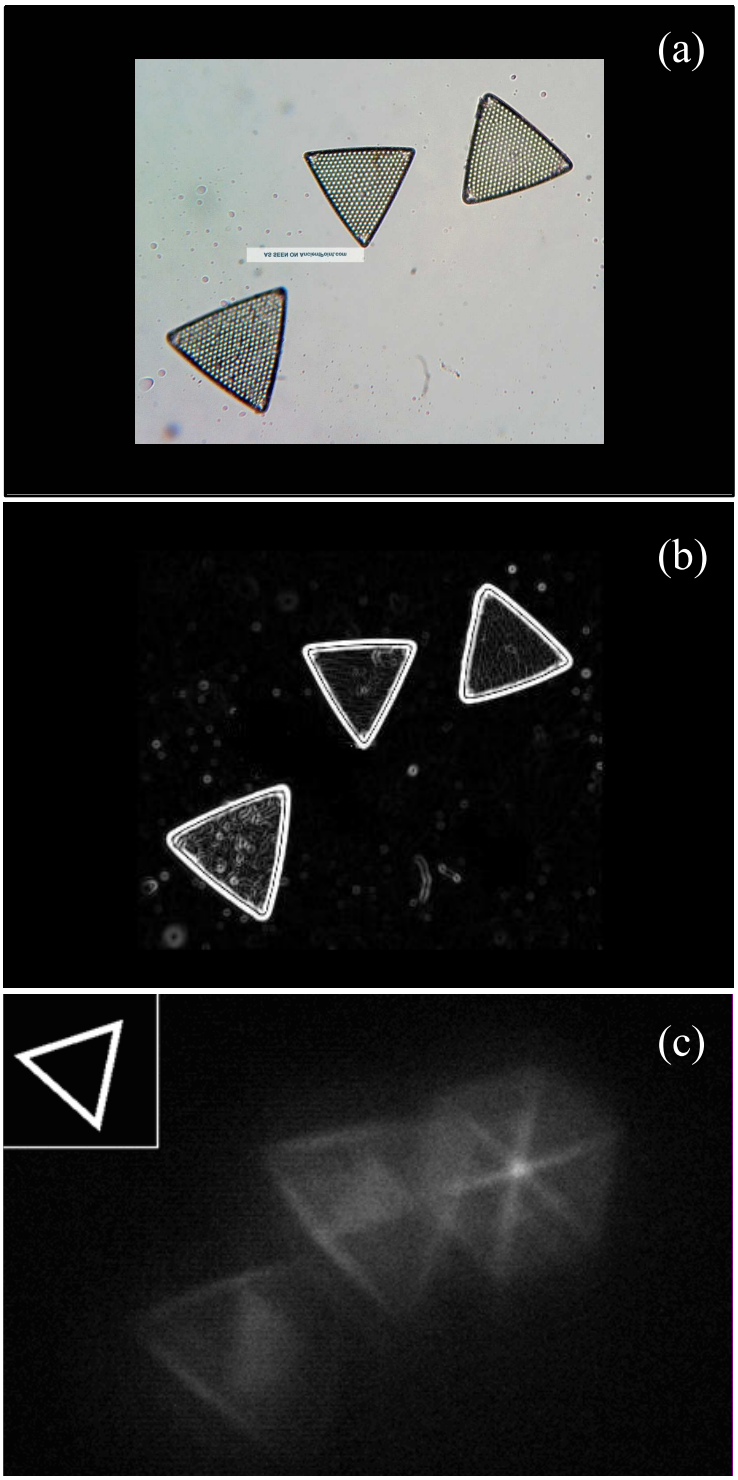

Figure 4.11: (a) Diatoms' original image; (b) edge-image; (c) optical Hough transform for a given orientation of the pupil (excerpt from Visualization: Diatoms), detecting the center of the diatom in the upper right corner of (a).

Chapter 5

Image segmentation by nonlinear filtering

The identification and extraction (i.e. segmentation) of geometrical features is crucial in many areas such as computer vision, microscopy, medical imaging, automatic defect inspection and surveillance applications. Segmentation procedure is often preceded by an image contouring stage, i.e. the identification of edges that serve as boundaries which delimit regions of the image with different properties (e.g. levels of gray, textures or colors). This can be performed, for example, by the use of simple edge detection algorithms (e.g. Canny, Sobel [Gonzalez and Woods, 2002]) or variational methods [Mitiche and Ayed, 2010] among which active contours are one of the most widely used [Chan and Vese, 2001, Blake and Isard, 2012].

In order to accelerate time of processing, several optical approaches have been proposed, which include the opto-electronical implementation of active contours [Ambs et al., 2004], high-pass filtering of images using coherent optical processors (see Section 1.2.1.1) [Situ et al., 2009, Shih et al., 2001, Yelleswarapu et al., 2006] and contouring by the use of incoherent optical processors (see 1.2.2.1) [Fernández et al., 2011, Flores et al., 2010]. For the separation of a specific feature from the edge image, a classification scheme may follow. For example, active contours have been modified to take into account a stopping condition over a specific shape [Chen et al., 2002].

Alternatively, mapping geometrical features to points in a parameter space provides a good means of classifying and extracting a given feature. As we have seen, the Linear Hough Transform (LHT) has proven to be an efficient technique for pattern recognition on edge images but for the final extraction/enhancement of a geometrical feature of interest, the inverse LHT has to be implemented [Casasent and Krishnapuram, 1987, McKenzie and Protheroe, 1990]. That is, peaks in the transformation

need to be mapped back to image space however this peaks represent the most voted parameter combinations but not the pixels that gave rise to them.

For the inversion of the LHT, an algorithm that is capable of recovering those pixels of a grayscale image which gave rise to the highest peaks in LHT space has been proposed [Kesidis and Papamarkos, 1999]. In the closely related Radon Transform (RT) (see Section 2.1.1), the inverse transformation is implemented in order to recover an image from its projections along different directions in the plane. This is a common operation, based on the Fourier Slice theorem, which has been successfully applied, in particular in medical imaging. In [Nishimura et al., 1978] an inversion method for the RT using coherent light is presented.

In the next we will present the optical extraction of a geometrical feature based on the nonlinear filtering of the Generalized Hough Transform (GHT) [Fernández et al., 2016, Fernández, 2016a]. We start by considering the theory behind the method along with an assessment of the robustness of the proposal considering synthetic images with noise, contrast degradation and overlapping. Finally, the experimental setup and the results obtained are presented.

5.1 Segmentation by nonlinear filter: theory

5.1.1 Convolution inverse

Let us start by considering the convolution form of the GHT given by Equation (3.12)

$$H(x,y;s,\theta) = I(x,y) * T^{(\pi)}(x,y;s,\theta) \tag{5.1}$$

where the input to the system is given by $I(x,y)$ and the Point Spread Function (PSF) by $T^{(\pi)}(x,y;s,\theta) = \delta(f_\pi(x,y;s,\theta))$. As pointed out in Section 3.3.1, a good approximation to the desired PSF is achieved under severe defocus (i.e. a system where the dominant aberration is defocus, see Appendix A) where the PSF essentially corresponds to the normalized geometrical projection of the (rotated) pupil onto the output plane. The convolution kernel associated to the projected pupil may be given by [Bracewell, 2004]

$$T(x,y;s,\theta) = \frac{1}{\ell(s)\tau} rect\left(f(x,y;s,\theta)\right), \tag{5.2}$$

which represents a narrow strip of width τ around the contour of the template of length $\ell(s)$ defined by Equation (3.4). This unit-area response approaches $\delta(f(x,y;s,\theta))$ in the limit $\tau \to 0$ and when rotated through π serves as PSF in Equation (5.1).

A schematic representation of the optical system implementing the GHT is given

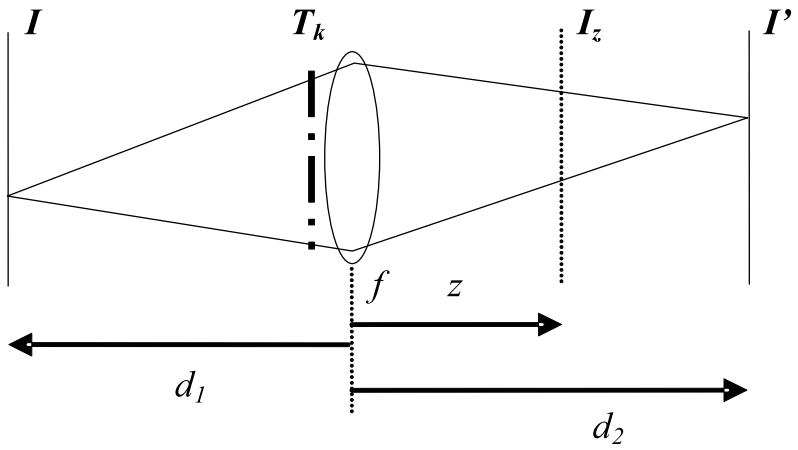

Figure 5.1: Optical setup for GHT and segmentation. f is the lens focal length; I is the edge enhanced binary image at the object plane; T_k is the pupil and I' is the output image at the in-focus plane. I_z is the GHT obtained at an intermediate plane z.

in Figure 5.1. The edge-enhanced binary image I to be processed can be considered as the sum of different unit intensity features T_i (placed at reference points (x_i, y_i)), among which the pattern of interest T_k -of given orientation and scale and located around reference point (x_k, y_k) - can be found

$$I = T_k(x - x_k, y - y_k) + \sum_{i \neq k} T_i(x - x_i, y - y_i) \tag{5.3}$$

(where for simplicity we have consider only one copy of the pattern of interest, but the generalization to an arbitrary number of copies is straightforward). Aside from magnification and inversion, geometric optics predicts that at the in-focus plane (at distance d_2 from the lens system, which verifies $d_1^{-1} + d_2^{-1} = f^{-1}$) we will essentially recover -regardless of the selected pupil- the original image I (see Appendix A)

$$I' = I. \tag{5.4}$$

If the pupil of the imaging system resembles T_k one obtains at an intermediate plane between the lens and the in-focus plane ($z < d_2$) the GHT given by Equation (5.1)

$$I_z = I * T_k^{(\pi)} \tag{5.5}$$

with a scale factor for the GHT given by $s = 1 - \frac{z}{d_2}$ in accordance with Equation (3.14). Between the intermediate plane and the in-focus plane a linear shift-invariant transformation holds, so the image I' at the in-focus plane can be given by

the convolution of I_z with an operator (A) to be determined

$$I' = I_z * A. \tag{5.6}$$

By means of equation Equation (5.5) the previous expression can be rewritten as

$$I' = \left(I * T_k^{(\pi)}\right) * A. \tag{5.7}$$

From Equation (5.4), it is easy to see that operator A needs to satisfy

$$T_k^{(\pi)} * A = \delta. \tag{5.8}$$

Consider now $T_k^{(\pi)(-1)}$ the convolution inverse element of $T_k^{(\pi)}$, which satisfies

$$T_k^{(\pi)} * T_k^{(\pi)(-1)} = \delta. \tag{5.9}$$

and which is commonly found -in its Fourier domain form- in the inverse filter theory of image restoration [Gonzalez and Woods, 2002, Goodman, 1996]. Operator A can so be identified with the convolution inverse element of $T_k^{(\pi)}$

$$A = T_k^{(\pi)(-1)}, \tag{5.10}$$

and I' in Equation (5.6) now reads

$$I' = I_z * T_k^{(\pi)(-1)}. \tag{5.11}$$

Between the GHT plane and the in-focus plane, convolution with $T_k^{(\pi)(-1)}$ acts as an inverse GHT that allows to recover the original image.

5.1.2 Thresholding

Let us now recall the GHT and write it in its explicit form, which results from the substitution of Equation (5.3) into Equation (5.5):

$$I_z = T_k(x - x_k, y - y_k) * T_k^{(\pi)} + \sum_{i \neq k} T_i(x - x_i, y - y_i) * T_k^{(\pi)}, \tag{5.12}$$

and consider the superposition of a mask across the GHT plane in order to filter the region around the maximum of the transformation. According to the normalization of the PSF as given by Equation (5.2), this maximum of the GHT equals the unit intensity and will be located at reference point (x_k, y_k) (the region around this maximum is determined by those points whose GHT value is above a certain intensity

threshold). Let I_z^{th} be the result of thresholding I_z, so from Eq. Equation (5.12) we keep only the term corresponding to (x_k, y_k) and its vicinity:

$$I_z^{th} = T_k(x - x_k, y - y_k) * T_k^{(\pi)}. \tag{5.13}$$

Considering I_z^{th} instead of I_z , Equation (5.11) results in

$$I'^{th} = T_k(x - x_k, y - y_k) * T_k^{(\pi)} * T_k^{(\pi)(-1)}, \tag{5.14}$$

and using the inverse defined in Equation (5.9), the previous equation simplifies to

$$I'^{th} = T_k(x - x_k, y - y_k). \tag{5.15}$$

Thus, the image I'^{th} at the in-focus plane only retains from the original image the template we wish to segment. As an illustrative case of the proposed segmentation method, consider the synthetic example of Figure 5.2. The feature of interest to be segmented is the circle in Figure 5.2(a). Figure 5.2(b) is the result of the GHT of Figure 5.2(a), using an annular pupil resembling the target. Figure 5.2(c) corresponds to thresholding of Figure 5.2(b), and finally Figure 5.2(d) shows the result of inverse filtering of Figure 5.2(c).

5.2 Segmentation under noise, contrast loss and overlapping

In order to provide an assessment of the robustness of our proposal we study how the performance of our method would be affected by

(i) presence of noise in the input,

(ii) low contrast of the binary image,

(iii) overlapping between the feature of interest and other features

To address Item (i) we consider the degradation of an ideal synthetic image [see Figure 5.2(a)] with strong additive white Gaussian noise of null mean and standard deviation of noise $\sigma_{noise} = 100$ [Figure 5.3(a_1)] with the ideal binary image between 0 (black) and 255 (white). We then perform the GHT of the noisy image using the circle in Figure 5.2(a) as a template and obtain the result of Figure 5.3(a_2) where is worth noticing that original noise has been averaged over the entire field of view (as might then be expected in a system linear in intensity). Finally, after thresholding

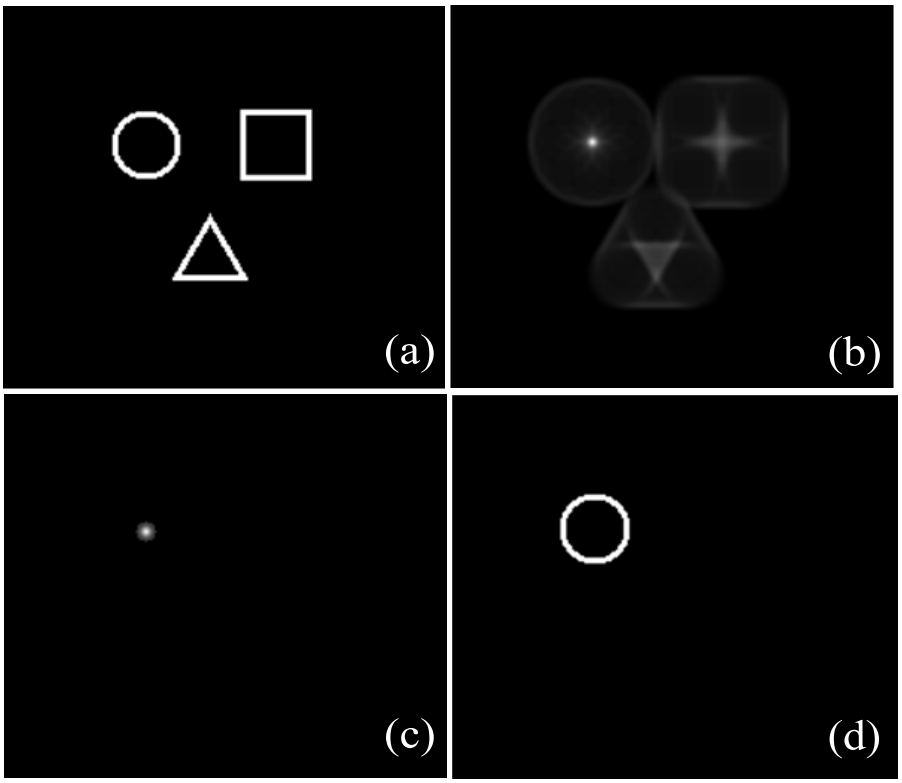

Figure 5.2: Segmentation method. (a) Edge-enhanced binary image I (the feature of interest is the circle); (b) GHT of (a); (c) Thresholding of (b); (d) result obtained after inverse filtering of (c).

and inverse filtering, the segmented circle is obtained (Figure 5.3(a_3)). If we normalize this result by the highest intensity and compare it to the expected normalized template we obtain a Root Mean Square Error (RMSE) of 0.0457, i.e., even under strong noise the system is capable of segmenting a figure that only differs in roughly a 5% from the expected one. We also perform the same study for different levels of noise and an ensemble of 100 sample realizations of the noise process (Figure 5.4). The results show that the performance is almost independent of the degree of noise in the image due to the averaging -under the GHT- of noise over the entire field of view. The selection of a maximum even under great amount of noise is a robust operation (see the bright spot in Figure 5.3(a_2)).

We also test the robustness of the method against a contrast loss in the original image (Item (ii)). Figure 5.3(b_1) shows a version of Figure 5.2(a) where the intensity of edges has been reduced in 70%. In spite of this reduction, the RMSE for the reconstructed circle in Figure 5.3(b_3) is still around 5%.

Finally we test the robustness against overlapping of the feature of interest with other features in synthetic images. We address Item (iii) in two parts: first we consider the overlapping with features of different shape and same size and then we consider the same feature with different size. Figure 5.3(c_1) shows the feature of interest (circle) overlapped by a square of the same size whose center is 10 pixels away from the circle's center. The reconstruction of the circle (Fig 3(c3)) is accomplished with RMSE=0.0503, in agreement with the expected template. We then consider a circle differing in size from the template (1.5 times larger) and whose center is separated in $d = 20$ pixels from the feature of interest's center. The result of the segmentation corresponds to RMSE=0.0501. It is also interesting to see the performance of the method under different degrees of overlapping. Figure 5.5 shows the results of varying distance (d) between centers from the case where centers coincide to circles with no overlap Even when d coincides with the difference of circles' radii and maximum overlapping is attained, reconstruction error is still around 5%.

From the above results it can be clearly seen that our segmentation method is robust against different error sources.

5.3 Experimental results

We experimentally validate the procedure of segmentation previously presented using the setup depicted in Figure 5.6. The template we are looking for is set as pupil (P) of the lens system of our setup and it consists of a binary pattern printed on a glass cover (note that since the GHT is obtained before the in-focus plane, we are in the situation depicted in Figure 3.4(b) and the pupil represents the template

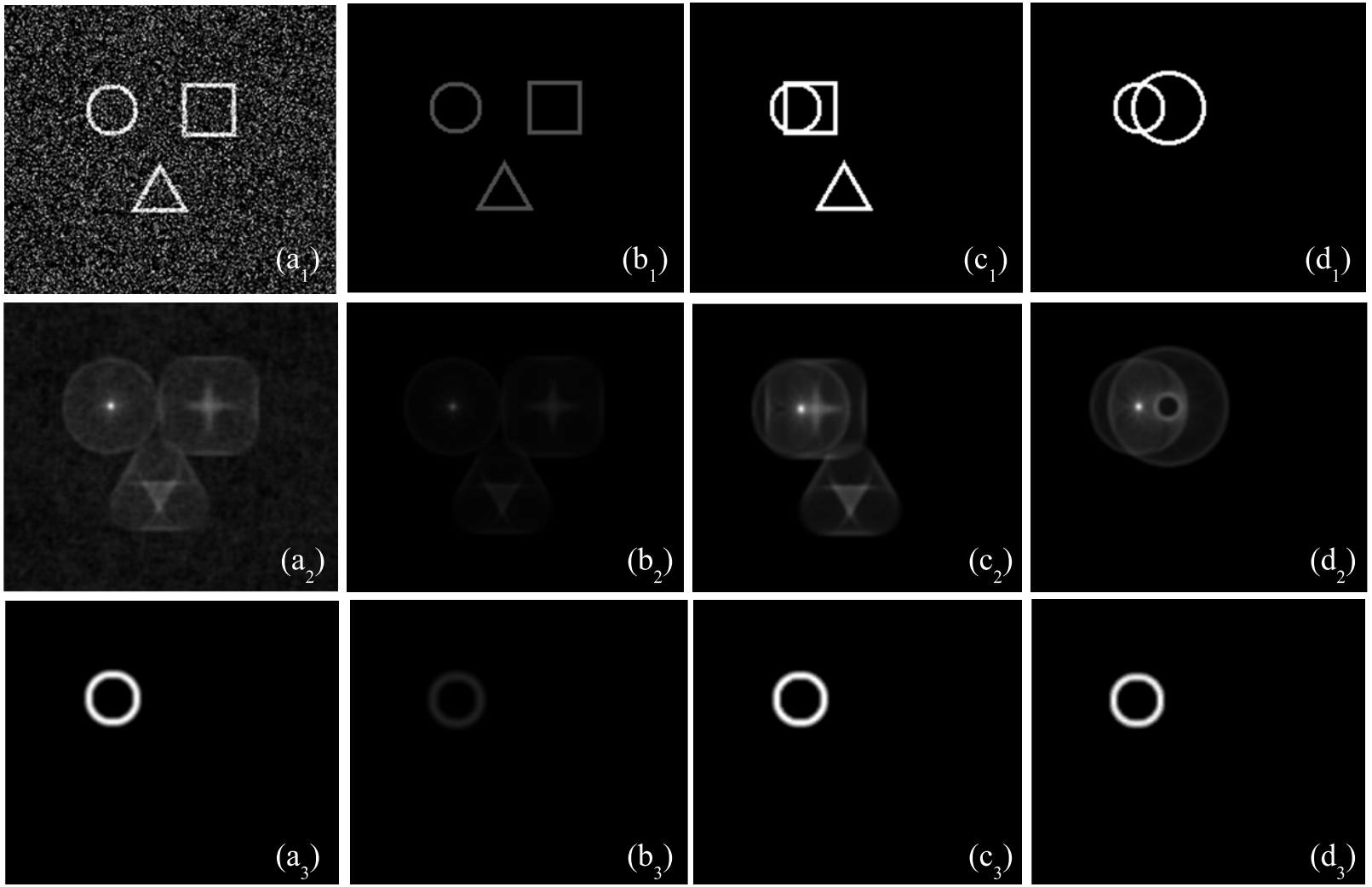

Figure 5.3: Robustness of the segmentation method; row 1: original images; row 2: GHTs of row 1; row 3: segmentation results after thresholding of row 2 and inverse filtering. (a) Severely degraded version of Figure 5.2(a) with Gaussian additive noise of null mean and $\sigma_{noise} = 100$ (RMSE=0.0457); (b) 70% contrast reduced version of Figure 5.2(a) (RMSE=0.0446); (c) Overlapping of the feature of interest (circle) with a different geometrical feature of the same size, $10px$ separation between centers (RMSE=0.0503); (d) Overlapping of the feature of interest with another circle 1.5 times larger, $20px$ separation between centers (RMSE=0.0501).

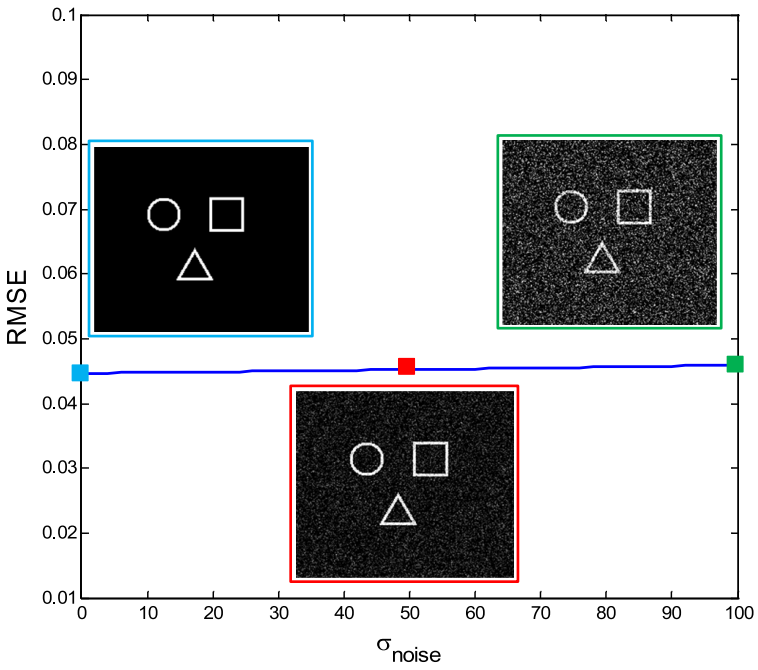

Figure 5.4: Performance under Gaussian additive noise of null mean. RMSE (averaged over 100 realizations) for different values of σ_{noise} (standard deviation of noise) showing an almost uniform performance from weak ($\sigma_{noise} = 0$, RMSE=0.0446) to strong noise ($\sigma_{noise} = 100$, RMSE=0.0459).

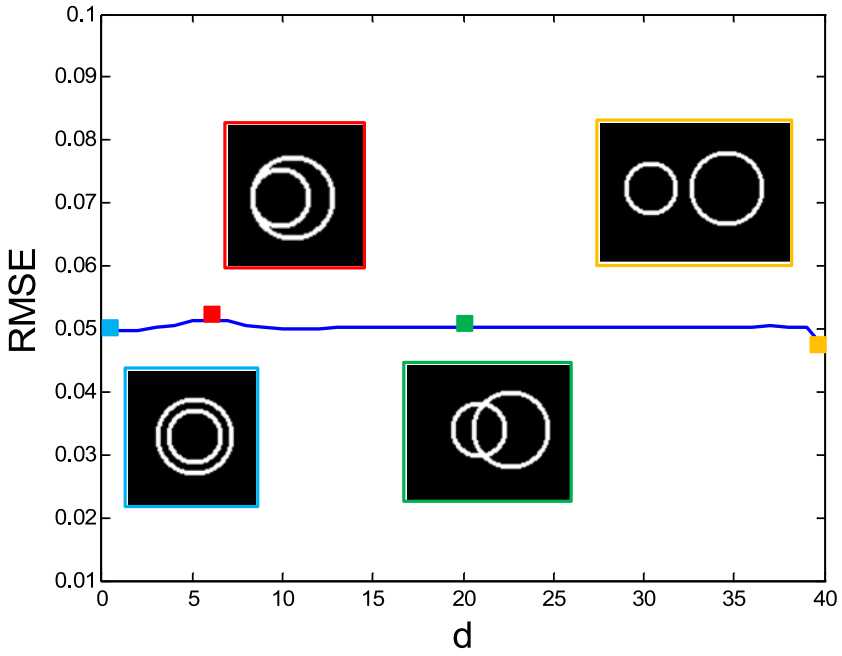

Figure 5.5: Performance under overlapping of the feature of interest (circle) and a 1.5 times bigger circle. RMSE for different degrees of overlapping distance between centers in pixel units (d) is shown and attains a maximum of RMSE=0.0514 when d coincides with the difference of the radii of the circles (red border inset).

without rotation in π). The lens system is an electrically tunable lens (ETL) with controllable focal length in the range $210 - 80mm$ (same as in Section 3.4) which allows to change the scale of the GHT. By means of a beam splitter (BS) the same GHT is simultaneously imaging at C_1 and LCD planes (note that equal length in each path needs to be achieved). In C_1 plane the sensor of a CCD camera (Thorlabs DC310, 1024x768 pixels)is placed and used to acquire a digital image. In order to filter the maxima of the GHT, a binary mask is displayed in the liquid crystal display (LCD)(Holoeye LC2002, 600x800 pixels).

From the image acquired at C_1 we can easily detect the maxima. After a simple step of spatial calibration between the camera and the LCD (see Appendix B), we set unit transmittance for those pixels in the LCD which correspond in the camera C_1 to intensity values above a certain threshold (typically 90-95% of I_{max}) and zero for the rest. According to Equation (5.15) this would let us capture at C_2 only the information corresponding to the template we are looking for in the original image. At object plane O a binary transmittance image is displayed that contains the shape we were looking for -along with other shapes- and it is illuminated with green (in order to maximize the contrast in the LCD) incoherent light (illumination is obtained from an LCD projector, so a rugged dispersive material was placed along with the binary image in order to enhance spatial incoherence of the source). The in-focus image at plane C_2 is captured by means of a digital camera (Pentax $K - \chi$) whose sensor is located at C_2.

5.3.1 Segmentation by shape

In the first experiment series we test the capability of our system to differentiate between patterns that are different in shape and similar in size. Orientation variants of the same shape can be thought as different shapes of the same size so we concentrate in a particular case of detection among simple curves: a circle, a square, and a triangle. Figure 5.7(c_0) shows the image to be processed, as captured at C_2 under full transmittance of the LCD (i.e., before filtering is implemented). Figures 5.7(a_{1-3}) show the GHT (images as captured by the camera at C_1) using a circle, square and triangle as template pupil, respectively. After thresholding the GHT captured at C_1 and displaying the corresponding binary mask on the LCD (Figs. 5.7(b_{1-3})), one obtains the filtered results at C_2 plane. The results are depicted in Figs. 5.7(c_{1-3}) and show that it is possible to extract from the original image those regions matching the template used for the GHT (circle, square and triangle, respectively).

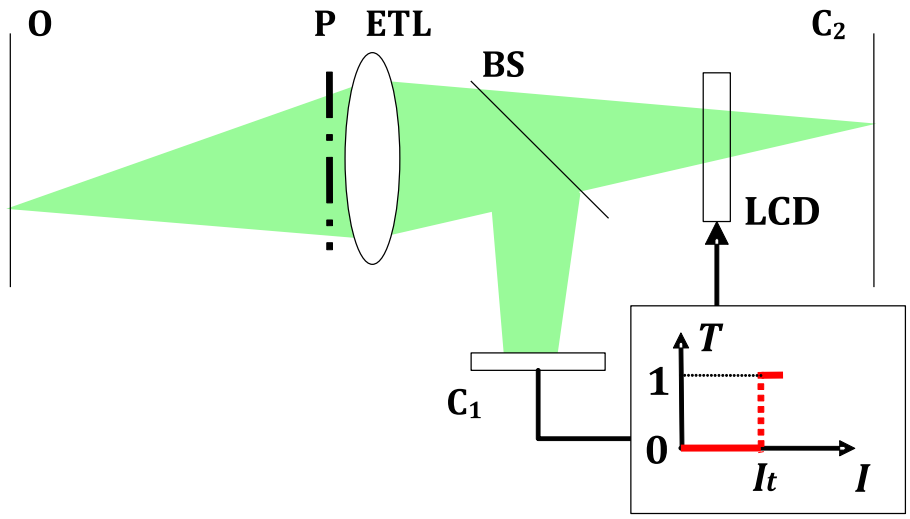

Figure 5.6: Experimental setup for optical GHT with nonlinear filtering. O: object plane; P: pupil; ETL: electrically tunable lens; BS: beam-splitter; LCD: liquid crystal display; $C_{1,2}$: capture planes. Transmittance (T) of the pixels in the LCD is set to one for those corresponding to intensity I above threshold I_t in C_1.

5.3.2 Segmentation by size

We can also consider the segmentation of a pattern of certain size out of a scene that contains replicas which differ in scale from it. Figure 5.8(a) shows the test image as captured at C_2 under full transmittance of LCD (i.e., before the filtering is implemented). It consists of a triangular shape with a given orientation but in three different sizes. Using a triangle as template, we adjust the scale of the GHT (by controlling the ETL) to match the medium size triangle, as shown in Figure 5.8(b) (as captured at C_1). Figure 5.8(d), corresponding to the capture after filtering, shows that our system is capable of extracting a given pattern by size.

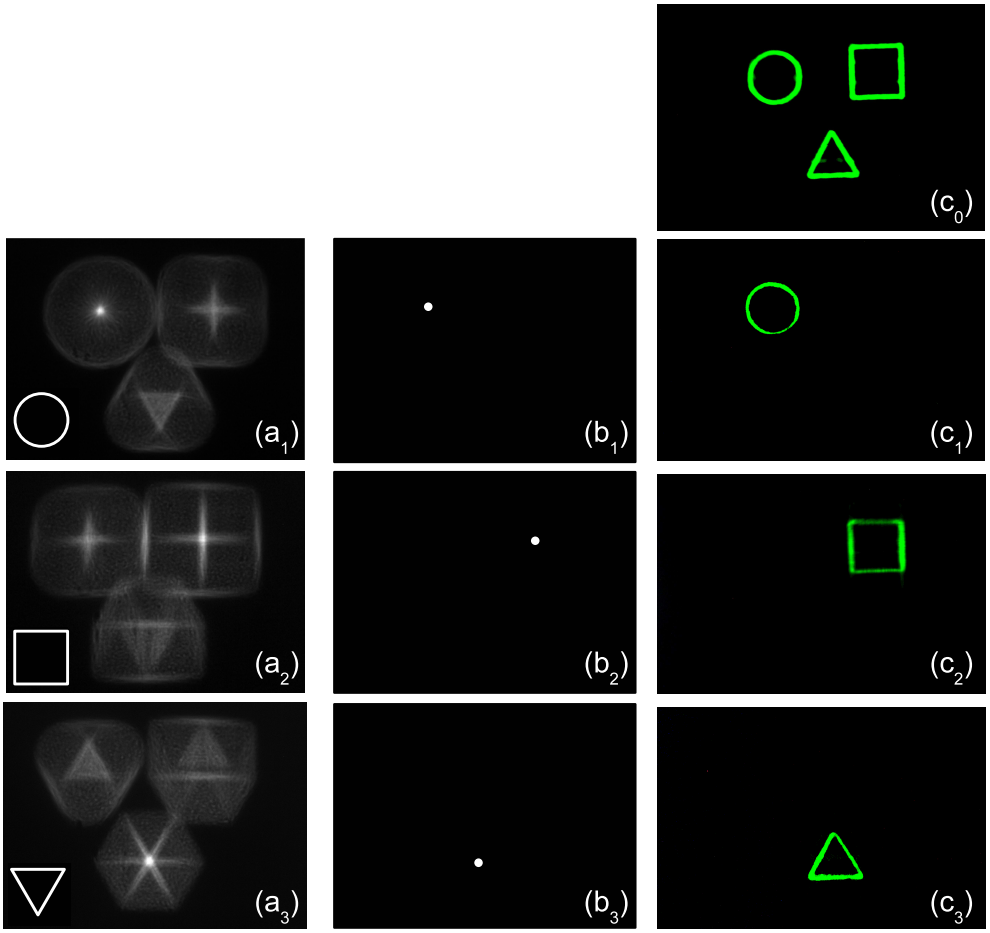

Figure 5.7: Feature extraction by shape. (c_0) Capture at image plane C_2 under full transmittance of LCD; (a_{1-3}) GHT (as obtained on the camera C_1) for pupil resembling a circle, square and triangle, respectively (lower left inset). (b_{1-3}) Binary masks displayed on the LCD. (c_{1-3}) Capture at the image plane C_2 after filtering (same contrast enhancement operation as in (c_0)).

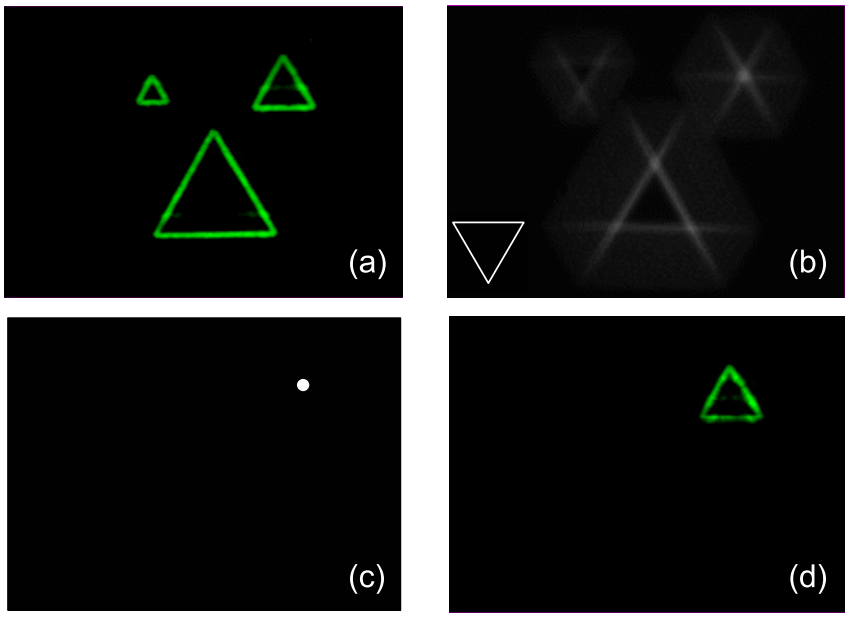

Figure 5.8: Feature extraction by size. (a) Capture on the image plane (C_2) under full transmittance (contrast enhanced); b) GHT as obtained by the camera at C_1, lower left corner showing the pupil template (note the inversion in the GHT of the small triangle with respect to the large one); (c) binary mask at LCD (d) Capture at the image plane (C_2) after filtering (same contrast enhancement operation as in (a)).

Chapter 6

Conclusions

In the present thesis we proposed an optical implementation of the GHT using a setup working under incoherent illumination, which can handle the real-time detection of a given shape in static binary images or video sequences. Unlike computer-based GHT, in principle, our system has no restriction in execution time due to the resolution of the images or frame rate of the videos to be processed.

We demonstrated through a series of experiments the applicability of the optical GHT in pattern recognition tasks. As we worked on a linear invariant system the resulting optical image processing is inherently parallel which resulted extremely useful in the simultaneous detection of targets of a given scale and orientation, which makes the proposed optical implementation of the GHT suitable for real-time applications. We also assessed the robustness of the detection capability of the method against noise and contrast loss.

By temporal multiplexing, we were able to achieve scale and orientation changes and extract the matching results for different parameters from a video sequence that it is only limited by the frame rate of the display and capturing devices. The variations in scale and orientation were achieved by adjusting the focal setting and the angle of the template of our system, respectively.

Through another series of experiments we also demonstrated the capability of the proposed system (with a suitable modification) to perform image segmentation. By applying nonlinear filtering over the generalized optical HT we were able to segment a given pattern from an edge-enhanced binary scene containing different shapes as well as copies of the pattern differing in size. The segmentation scheme resulted robust against the presence of noise in the input, low contrast of the binary image, and possible overlapping between the feature of interest and other features in the image.

6.1 Future lines of work

The optical implementation of the GHT offers the possibility for different direct applications or improvements of the existing setups for pattern recognition.

6.1.1 Pattern recognition in scattering media

Based on the robustness of the GHT under noise (see **??**) it is feasible to consider the detection of given targets in noisy or turbid environments, e.g. scattering media where, for example, polarization-difference imaging has proven useful [Tyo et al., 2006, Tyo et al., 1996].

6.1.2 Pattern recognition of phase objects

An unique feature (as compared with purely digital) of optical processing is the possibility of operating on the light wave previous to digital capture. In many microscopy applications the specimens of interest only modify the phase of light and different techniques like Differential Interference Constrast [Chen et al., 2013, Trattner et al., 2014], Differential Phase Constrast [Mehta and Sheppard, 2009, Tian et al., 2014] or Transport of Intensity Equation [Martinez-Carranza et al., 2015, Zuo et al., 2015] need to be applied in order to visualize and retrieve the phase perturbation. The combination of the previous techniques with GHT would expand the horizon of pattern recognition into phase objects.

6.1.3 All-optical processing

An interesting future line of work would be exploring the implementation of the segmentation method in an all-optical architecture, replacing the digital thresholding with the use of a nonlinear optical material like Bacteriorhodopsin [Thoma et al., 1991, Downie, 1995]. This may allow us to reduce the bulk of the segmentation device to a single imaging and thresholding plane where the nonlinear material would be placed.

6.1.4 Space multiplexing and template-variant detection

Parallel feature extraction has been explored in [Shin and Jang, 2000, Mori and Ohba, 1994]. An interesting future line of work would be considering space multiplexed scale and orientation-invariant pattern recognition by means of a mask (template matrix with variable scale and orientation) in front of a micro-lens array. Each elemental image would correspond to the GHT for different combinations of orientation and scale of the same or different templates, i.e. we exchange the time-multiplexing where

the different combinations are recorded in a video sequence for a single-shot spatially multiplexed transformation at lower resolution.

Publications

Publications related to the thesis topic:

Journal articles

- Fernández, A., Alonso, J. R., Ayubi, G. A., Osorio, M., and Ferrari, J. A. (2015a). Optical implementation of the generalized Hough transform with totally incoherent light. *Optics Letters*, 40(16):3901–3904
- Fernández, A., Flores, J. L., Alonso, J. R., and Ferrari, J. A. (2015b). Real-time pattern recognition using an optical generalized Hough transform. *Applied Optics*, 54(36):10586–10591
- Fernández, A., Flores, J. L., Alonso, J. R., and Ferrari, J. A. (2016). Image segmentation by nonlinear filtering of optical Hough transform. *Applied Optics*, 55(13):3632–3638

Conference papers

- Fernández, A. and Ferrari, J. (2015). Real-time Optical Realization of Circle Hough Transform with Incoherent Light. In *Frontiers in Optics*, pages JTu4A–57. Optical Society of America
- Fernández, A. (2016a). Pattern recognition and feature extraction with an optical Hough transform. In *SPIE Optical Engineering + Applications*, pages 99700N–99700N. International Society for Optics and Photonics
- Fernández, A. (2016b). Robust Pattern Recognition with Optical Generalized Hough Transform. In *Imaging Systems and Applications*, pages JTu3A–58. Optical Society of America

Appendix A

Defocus aberration in geometric optics.

Let us start by considering an object like the arrow in Figure A.1 whose intensity distribution in the object plane is given by $g(x_o, y_o)$. An ideal image of this object is to be obtained through a lens of focal length f at an image plane conjugated with the object plane, i.e. z_o and z_i satisfy the Gaussian imaging Equation (3.13):

$$\frac{1}{z_o} + \frac{1}{z_i} = \frac{1}{f}. \tag{A.1}$$

In this ideal case we obtain at the image plane a scaled replica of the object's intensity distribution $g(x, y)$

$$u(x_i, y_i) = \left(\frac{1}{M}\right)^2 g\left(\frac{x_i}{M}, \frac{y_i}{M}\right) \tag{A.2}$$

where the lateral magnification factor M is given by

$$M = -\frac{z_i}{z_o}. \tag{A.3}$$

From now on we will simply absorb the scale change and note by $g(x_i, y_i)$ the object's intensity distribution as seen in the image plane so Equation (A.2) reads

$$u(x_i, y_i) = g(x_i, y_i), \tag{A.4}$$

which compared with the convolution form of the response of a shift-invariant linear system Equation (3.11)

$$u(x_i, y_i) = g(x_i, y_i) * h(x_i, y_i), \tag{A.5}$$

shows that the (normalized) intensity PSF $h(x_i, y_i)$ of the ideal optical system corresponds to a Dirac delta function $\delta(x_i, y_i)$. Thus, the Fourier transform of the PSF is constant and equal to unity at all spatial frequencies. In this way, all spatial frequencies of the original object would be reproduced with the same weight and any detail of the object clearly imaged.

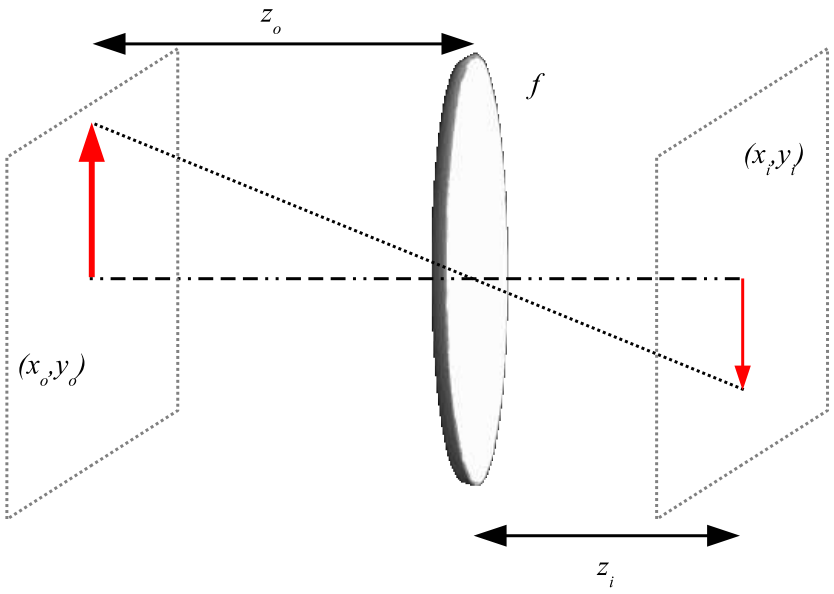

Figure A.1: Ideal image formation for object and image planes conjugated through Gauss imaging equation.

A.1 Optical Transfer Function

In order to proceed into the non ideal cases let us consider the Fourier transform ($\mathcal{F}$) of (A.5)

$$\mathcal{F}(u(x_i, y_i)) = \mathcal{F}(g(x_i, y_i) * h(x_i, y_i)) \tag{A.6}$$

which by means of the convolution theorem [Goodman, 1996] can be written as:

$$\mathcal{F}\{u(x_i, y_i)\} = \mathcal{F}\{g(x_i, y_i)\}\mathcal{F}\{h(x_i, y_i)\}, \tag{A.7}$$

where each Fourier transform is a function of the frequency pair (f_X, f_Y). Defining $\mathcal{U}/\mathcal{G}/\mathcal{H}(f_X, f_Y) = \mathcal{F}\{u/g/h(x_i, y_i)\}$, Equation (A.7) takes this form

$$\mathcal{U}(f_X, f_Y) = \mathcal{G}(f_X, f_Y)\mathcal{H}(f_X, f_Y) \tag{A.8}$$

where $\mathcal{H}(f_X, f_Y)$ is the *Optical Transfer Function* (OTF). As a very simple case, from the Fourier transform of Equation (A.4) we can identify $\mathcal{H}(f_X, f_Y) = 1$ which is the Geometrical OTF (GOTF) $\mathcal{H}_g(f_X, f_Y)$ for ideal imaging (see [Mahajan and Díaz, 2016] and references therein). In image formation under geometrical ideal conditions we are not taking into account the diffractive effects due to the finite aperture of the lens.

If we instead consider a diffraction-limited optical system (i.e. a system free from aberrations under Gauss imaging condition) the ideal image (scaled replica of the object) is convolved with the *Fraunhofer* diffraction pattern of the lens pupil [Goodman, 1996]. The smoothing operation in the image formation process will be reflected in the loss of details of the object which can be much easily analyzed in the frequency domain of the system by means of the Diffraction OTF (DOTF).

The DOTF for an incoherent, diffraction-limited system is given by the normalized autocorrelation of the *Pupil Function* P (unity inside the aperture of the lens, zero outside)

$$\mathcal{H}_d(f_X, f_Y) = \frac{\iint_{-\infty}^{+\infty} P(\xi, \eta) P(\xi - \lambda z_i f_X, \eta - \lambda z_i f_Y) d\xi d\eta}{\iint_{-\infty}^{+\infty} P(\xi, \eta) d\xi d\eta}. \tag{A.9}$$

The DOTF for a given frequency (f_X, f_Y) can also be interpreted as the fractional area of overlap of two pupils whose centers are located at $(0, 0)$ and $(\lambda z_i f_X, \lambda z_i f_Y)$, respectively. For a circular pupil of radius R we can exploit the revolution symmetry of the system and work with the frequency radial distance $\rho = \sqrt{f_X^2 + f_Y^2}$.

As it can be clearly seen in Figure A.2 there exists a cutoff frequency ρ_{co} (absent in the geometrical case) satisfying $\rho_{co} \lambda z_i = 2R$ (limit case of non-zero overlapping) above which $\mathcal{H}_d(\rho)$ vanishes:

$$\rho_{co} = \frac{2R}{\lambda z_i}, \tag{A.10}$$

which represents the maximum resolvable spatial frequency in the output image under incoherent illumination. For $\rho \leq \rho_{co}$, the radially symmetric DOTF satisfies [Goodman, 1996]:

$$\mathcal{H}_d(\rho) = \frac{2}{\pi} \left(arccos\left(\frac{\rho}{\rho_{co}}\right) - \frac{\rho}{\rho_{co}} \sqrt{1 - \left(\frac{\rho}{\rho_{co}}\right)^2} \right). \tag{A.11}$$

The dependence of $\mathcal{H}_d$ with normalized frequency $\frac{\rho}{\rho_{co}}$ is depicted in black in Fig. A.4.

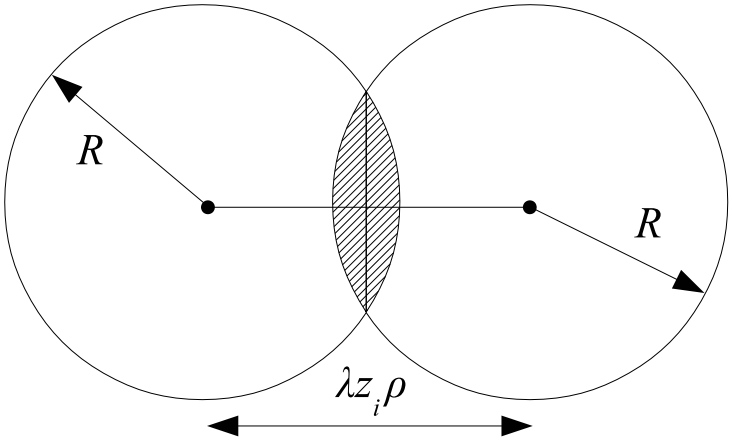

Figure A.2: Area of overlap (shaded) of two displaced circles.

A.2 Defocus aberration

A.2.1 Aberrated DOTF

Let us now treat with a system subject to a wave aberration by considering a phase error $\frac{2\pi}{\lambda}W(x,y)$ introduced in the aperture plane by means of an effective path-length error function $W(x,y)$ (see [Mahajan, 1998, Mahajan, 2011] for further details). We can then define a *generalized pupil function* $\mathcal{P}$ [Goodman, 1996]:

$$\mathcal{P}(x,y) = P(x,y)exp\left(j\frac{2\pi}{\lambda}W(x,y)\right) \tag{A.12}$$

which will give rise to a DOTF given by

$$\mathcal{H}_d(f_X,f_Y) = \frac{\iint_{-\infty}^{+\infty} \mathcal{P}(\xi,\eta)\mathcal{P}(\xi-\lambda z_i f_X, \eta-\lambda z_i f_Y)^* d\xi d\eta}{\iint_{-\infty}^{+\infty} |\mathcal{P}(\xi,\eta)|^2 \, d\xi d\eta} \tag{A.13}$$

which is a generalization of (A.9) for phase variation in the pupil.

For a defocus aberration, which is introduced when the image is observed in an image plane other than that conjugated to the object plane, $W(x,y)$ takes the form:

$$W(r) = W_m\left(\frac{r}{R}\right)^2, \tag{A.14}$$

where W_m is the maximum path-length error (attained at the edge of the aperture

$r = R$)

$$W_m = \frac{1}{2}\left|\frac{1}{z_i} - \frac{1}{z_a}\right| R^2, \tag{A.15}$$

and z_a (Fig. A.3) is conjugated to z_o through the Gaussian imaging equation (3.13):

$$\frac{1}{z_o} + \frac{1}{z_a} = \frac{1}{f}. \tag{A.16}$$

Considering the form of (A.14) in (A.12) and then substituting the generalized pupil $\mathcal{P}$ in (A.13), the results of $\mathcal{H}_d(\rho)$ for different values of $\frac{W_m}{\lambda}$ are the ones depicted in Fig. A.4.

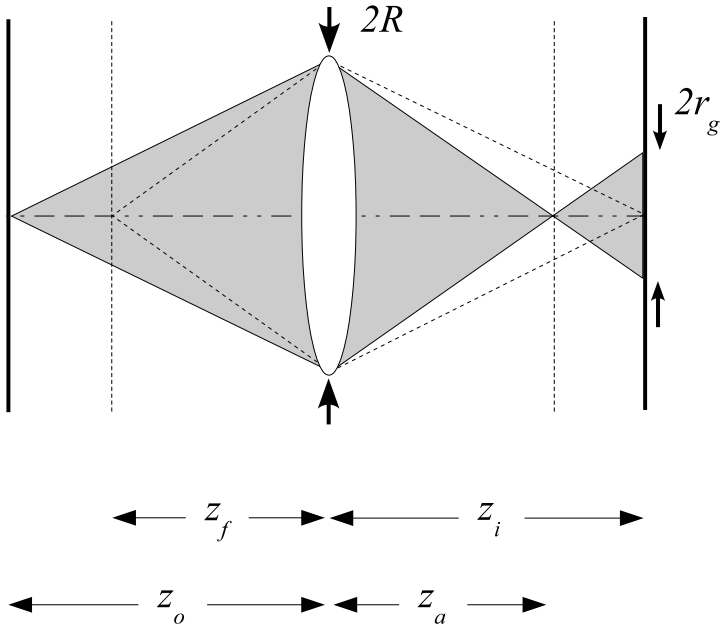

Figure A.3: Geometrical PSF for defocus aberration.

A.2.2 Aberrated GOTF

On the other hand, defocus also affects the geometrical OTF (GOTF). The response for a given point of the object corresponds to the projection of the pupil on the imaging plane, which for a circular pupil is a uniformly illuminated disk of radius r_g. The radius of this disk can be determined following the construction of Fig. A.3 (for similar construction and details see [Alonso et al., 2015] and references therein). For a point in the object plane we obtain a circle of radius r_g in the imaging plane

whenever $z_f \neq z_o$. Similarity between triangles gives:

$$\frac{r_g}{z_i - z_a} = \frac{R}{z_a}, \tag{A.17}$$

which can be rearranged as

$$r_g = R\left|\frac{z_i - z_a}{z_a}\right| = Rz_i\left|\frac{1}{z_a} - \frac{1}{z_i}\right|, \tag{A.18}$$

where we include the case $z_i < z_a$ by taking the absolute value.

A.2.2.1 Blurring radius for the optical GHT

Alternatively to (A.18) we can equate the left hand sides of (A.1) and (A.16)

$$\frac{1}{z_o} + \frac{1}{z_a} = \frac{1}{z_f} + \frac{1}{z_i}. \tag{A.19}$$

Substituting in (A.18) we finally obtain

$$r_g = Rz_i\left|\frac{1}{z_f} - \frac{1}{z_o}\right|, \tag{A.20}$$

which according to the parameters of the optical implementation of the GHT (Fig. 3.4) takes the form

$$r_g = Rd_C\left|\frac{1}{f} - \frac{1}{d_1}\right|. \tag{A.21}$$

Returning to (A.18), we can compare now the geometric radius with the maximum path-length error (A.15), resulting by the use of (A.10) in

$$r_g = 4\frac{W_m}{\lambda}\frac{1}{\rho_{co}}. \tag{A.22}$$

The corresponding (normalized) intensity PSF associated to this blurring disk is given by:

$$h_g(r_i) = \frac{1}{\pi r_g^2} circ\left(\frac{r_i}{r_g}\right), \tag{A.23}$$

where the circle function is given by:

$$circ\left(\frac{r_i}{r_g}\right) = \begin{cases} 1, & r_i = \sqrt{x_i^2 + y_i^2} \leq r_g \\ \\ 0, & r_i > r_g \end{cases} \tag{A.24}$$

The GOTF is so given by the Fourier transform of (A.23):

$$\mathcal{H}_g(\rho) = \mathcal{F}\{h_g(r_i)\} = \frac{2J_1\left(8\pi\frac{W_m}{\lambda}\frac{\rho}{\rho_{co}}\right)}{8\pi\frac{W_m}{\lambda}\frac{\rho}{\rho_{co}}}, \tag{A.25}$$

where $J_1(.)$ is the first-order Bessel function of the first kind and we made use of (A.22). Comparison between the diffractive and geometric OTFs is shown in the inset of Fig. A.4 where is clear that better agreement is achieved for increasing blurring degree.

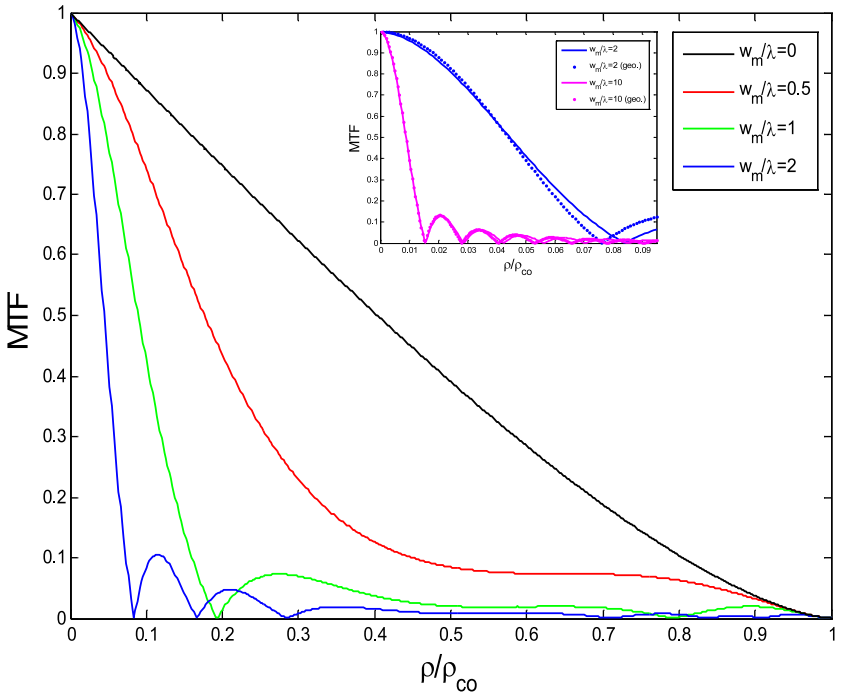

Figure A.4: Modulation Transfer Function (MTF=|OTF|) for circular pupil against defocus for $w_m/\lambda = 0, 0.5, 1, 2$. In the inset, the cases $w_m/\lambda = 2, 10$ and the comparison against the geometric optics aproximation.

According to the comparison in [Mahajan and Díaz, 2016] there is a threshold value $\frac{W_m}{\lambda} \sim 1.4$ above which GOTF differs from the corresponding DOTF within 5% for the normalized frequency in the range $0 \leq \frac{\rho}{\rho_{co}} < 0.11$. Since for our system $R = 6mm$, $\lambda \approx 550nm$ and $z_i = d_C \sim 16mm$: $\rho_{co} \approx 1400 lines/mm$. However, the finite size p of the pixel of the capture system imposes an effective cutoff frequency $\rho_{eff} = \frac{1}{p}$ which for a pixel size of $4.7\mu m$ gives $\rho_{eff} \approx 200 lines/mm$. That is, our effective range of normalized frequencies of interest lies below $\frac{\rho_{eff}}{\rho_{co}} \approx 0.14$ so the approximation of the response of the system by the geometric PSF is good for high

blurring.

Appendix B

Affine transformation.

For the calibration between the camera and the LCD in 5.3 we need to consider the geometric transformation [Gonzalez et al., 2009] between image pixels in each device. Let (x, y) be the coordinate points in the first image and (x', y') in the second one. The transformation of the coordinates can be expressed as

$$(x', y') = T\{(x, y)\} \tag{B.1}$$

A common spatial transformation is the so called *affine transform* (Fig. B.1) which preserves parallelism, ratio of areas and ratio of lengths on collinear or parallel lines (e.g. midpoints).

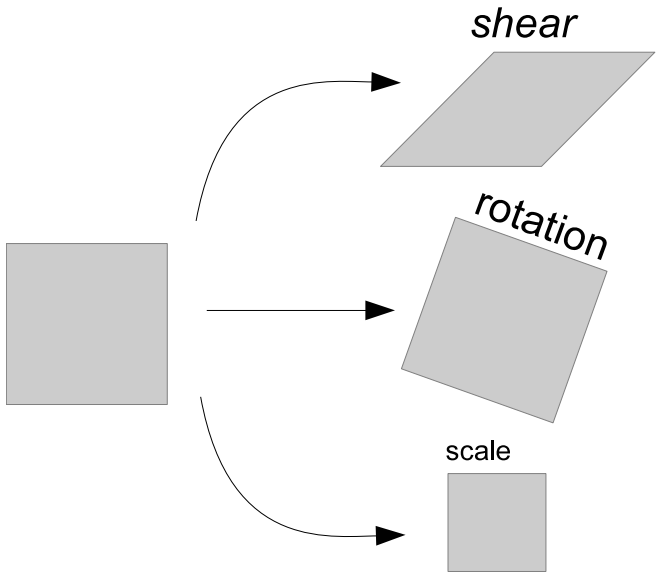

Figure B.1: Examples of affine transformations over a square: shear, rotation and scaling.

The affine transformation equation can be written in matrix form as

$$\begin{pmatrix} x' \\ y' \\ 1 \end{pmatrix} = \mathbf{T} \begin{pmatrix} x \\ y \\ 1 \end{pmatrix}, \mathbf{T} = \begin{pmatrix} t_{11} & t_{12} & t_{13} \\ t_{21} & t_{22} & t_{23} \\ 0 & 0 & 1 \end{pmatrix}. \tag{B.2}$$

For the special case of scale change, matrix $\mathbf{T}$ takes the form

$$\mathbf{T}_{scale} = \begin{pmatrix} s_x & 0 & 0 \\ 0 & s_y & 0 \\ 0 & 0 & 1 \end{pmatrix}, \tag{B.3}$$

whereas for a translation the matrix reads

$$\mathbf{T}_{translation} = \begin{pmatrix} 0 & 0 & \delta_x \\ 0 & 0 & \delta_y \\ 0 & 0 & 1 \end{pmatrix}. \tag{B.4}$$

The combination of these transformations can be put in matrix form considering for the transformation matrix the product of (B.3) and (B.4)

$$\begin{pmatrix} x' \\ y' \\ 1 \end{pmatrix} = \begin{pmatrix} s_x & 0 & \delta_x \\ 0 & s_y & \delta_y \\ 0 & 0 & 1 \end{pmatrix} \begin{pmatrix} x \\ y \\ 1 \end{pmatrix}. \tag{B.5}$$

Assuming this type of transformation between the displays, $\{s_x, s_y, \delta_x, \delta_y\}$ need to be determined. Let us start by considering the correspondence [Hartley and Zisserman, 2003] between coordinates (x_i, y_i) and (x'_i, y'_i) of a given point i known to be the same in each display (e.g. a maximum in the GHT in the camera and full transmittance in the LCD) and rewrite (B.5) as

$$\begin{pmatrix} x'_i \\ y'_i \end{pmatrix} = \begin{pmatrix} x_i & 0 & 1 & 0 \\ 0 & y_i & 0 & 1 \end{pmatrix} \begin{pmatrix} s_x \\ s_y \\ \delta_x \\ \delta_y \end{pmatrix}. \tag{B.6}$$

For (at least) $n = 2$ correspondences, (B.7) reads

$$\begin{pmatrix} x'_1 \\ y'_1 \\ x'_2 \\ y'_2 \end{pmatrix} = \begin{pmatrix} x_1 & 0 & 1 & 0 \\ 0 & y_1 & 0 & 1 \\ x_2 & 0 & 1 & 0 \\ 0 & y_2 & 0 & 1 \end{pmatrix} \begin{pmatrix} s_x \\ s_y \\ \delta_x \\ \delta_y \end{pmatrix}, \tag{B.7}$$

and $\{s_x, s_y, \delta_x, \delta_y\}$ can be found by inversion of the previous system. These parameters give the affine transformation that needs to be applied to every image in the first display to be correctly shown in the second, in particular to the maximum in the GHT shown in the camera C_1.

Bibliography

[Alfalou and Brosseau, 2009] Alfalou, A. and Brosseau, C. (2009). Optical image compression and encryption methods. *Advances in Optics and Photonics*, 1(3):589–636.

[Alieva, 2008] Alieva, T. (2008). First-order optical systems for information processing. In *Advances in Information Optics and Photonics*, volume 1, page 1. SPIE Press.

[Alonso et al., 2015] Alonso, J. R., Fernández, A., Ayubi, G. A., and Ferrari, J. A. (2015). All-in-focus image reconstruction under severe defocus. *Optics Letters*, 40(8):1671–1674.

[Alsamman, 2010] Alsamman, A. (2010). Spatially efficient reference phase-encrypted joint transform correlator. *Applied Optics*, 49(10):B104–B110.

[Ambs, 2010] Ambs, P. (2010). Optical computing: a 60-year adventure. *Advances in Optical Technologies*, 2010.

[Ambs et al., 2004] Ambs, P., Hueber, E., Matwyschuk, A., Bigue, L., and Christnacher, F. (2004). Two approaches, coherent and incoherent, for the optical implementation of active contours. In *Optical Science and Technology, the SPIE 49th Annual Meeting*, pages 203–215. International Society for Optics and Photonics.

[Ambs et al., 1986] Ambs, P., Lee, S. H., Tian, Q., and Fainman, Y. (1986). Optical implementation of the Hough transform by a matrix of holograms. *Applied Optics*, 25(22):4039–4045.

[Armitage and Lohmann, 1965] Armitage, J. and Lohmann, A. (1965). Character recognition by incoherent spatial filtering. *Applied Optics*, 4(4):461–467.

[Asghari and Jalali, 2013] Asghari, M. H. and Jalali, B. (2013). Anamorphic transformation and its application to time–bandwidth compression. *Applied Optics*, 52(27):6735–6743.

[Atherton and Kerbyson, 1999] Atherton, T. J. and Kerbyson, D. J. (1999). Size invariant circle detection. *Image and Vision computing*, 17(11):795–803.

[Awwal et al., 2010] Awwal, A., Iftekharuddin, K., Karim, M., Neifeld, M., and Stork, D. (2010). Convergence in Optical and Digital Pattern Recognition: introduction to the feature issue. *Applied Optics*, 49:DPR1–DPR2.

[Awwal, 2010] Awwal, A. A. S. (2010). What can we learn from the shape of a correlation peak for position estimation? *Applied Optics*, 49(10):B40–B50.

[Ballard, 1981] Ballard, D. H. (1981). Generalizing the Hough transform to detect arbitrary shapes. *Pattern recognition*, 13(2):111–122.

[Bartelt et al., 1982] Bartelt, H., Case, S., and Hauck, R. (1982). Incoherent optical processing. In *Applications of Optical Fourier Transforms*, pages 499–536. Academic, New York.

[Blake and Isard, 2012] Blake, A. and Isard, M. (2012). *Active contours: the application of techniques from graphics, vision, control theory and statistics to visual tracking of shapes in motion*. Springer Science & Business Media.

[Blanco et al., 2006] Blanco, M., Penedo, M. G., Barreira, N., Penas, M., and Carreira, M. J. (2006). Localization and extraction of the optic disc using the fuzzy circular Hough transform. In *Artificial Intelligence and Soft Computing–ICAISC 2006*, pages 712–721. Springer.

[Bone et al., 2006] Bone, P., Young, R., and Chatwin, C. (2006). Position-, rotation-, scale-, and orientation-invariant multiple object recognition from cluttered scenes. *Optical Engineering*, 45(7):077203–077203.

[Born and Wolf, 2000] Born, M. and Wolf, E. (2000). *Principles of optics: electromagnetic theory of propagation, interference and diffraction of light*. CUP Archive.

[Bouchal and Bouchal, 2012] Bouchal, P. and Bouchal, Z. (2012). Selective edge enhancement in three-dimensional vortex imaging with incoherent light. *Optics Letters*, 37(14):2949–2951.

[Bouchal et al., 2014] Bouchal, Z., Chlup, V., Čelechovskỳ, R., Bouchal, P., and Nistor, I. C. (2014). Achromatic correction of diffractive dispersion in white light SLM imaging. *Optics Express*, 22(10):12046–12059.

[Bracewell, 2004] Bracewell, R. (2004). *Fourier analysis and imaging*. Springer Science & Business Media.

[Bykov et al., 2014] Bykov, D. A., Doskolovich, L. L., Bezus, E. A., and Soifer, V. A. (2014). Optical computation of the Laplace operator using phase-shifted Bragg grating. *Optics Express*, 22(21):25084–25092.

[Canny, 1986] Canny, J. (1986). A computational approach to edge detection. *IEEE Transactions on pattern analysis and machine intelligence*, (6):679–698.

[Casasent and Krishnapuram, 1987] Casasent, D. and Krishnapuram, R. (1987). Curved object location by Hough transformations and inversions. *Pattern Recognition*, 20(2):181–188.

[Casasent and Psaltis, 1976] Casasent, D. and Psaltis, D. (1976). Position, rotation, and scale invariant optical correlation. *Applied Optics*, 15(7):1795–1799.

[Casasent and Richards, 1993] Casasent, D. and Richards, J. (1993). High-speed acousto-optic mapping modulator for the generalized Hough transform. *Applied Optics*, 32(35):7217–7224.

[Cauchie et al., 2008] Cauchie, J., Fiolet, V., and Villers, D. (2008). Optimization of an Hough transform algorithm for the search of a center. *Pattern Recognition*, 41(2):567–574.

[Caulfield, 1998] Caulfield, H. J. (1998). Perspectives in optical computing. *Computer*, 31(2):22–25.

[Cha et al., 2006] Cha, J., Cofer, R., and Kozaitis, S. (2006). Extended Hough transform for linear feature detection. *Pattern Recognition*, 39(6):1034–1043.

[Chan and Vese, 2001] Chan, T. F. and Vese, L. A. (2001). Active contours without edges. *IEEE transactions on Image processing*, 10(2):266–277.

[Chen and Deng, 2015] Chen, B. and Deng, X. (2015). A landmark matching algorithm using the improved generalised Hough transform. In *SPIE Remote Sensing*, pages 96431V–96431V. International Society for Optics and Photonics.

[Chen et al., 2013] Chen, J., Xu, Y., Lv, X., Lai, X., and Zeng, S. (2013). Super-resolution differential interference contrast microscopy by structured illumination. *Optics Express*, 21(1):112–121.

[Chen et al., 2002] Chen, Y., Tagare, H. D., Thiruvenkadam, S., Huang, F., Wilson, D., Gopinath, K. S., Briggs, R. W., and Geiser, E. A. (2002). Using prior shapes in geometric active contours in a variational framework. *International Journal of Computer Vision*, 50(3):315–328.

[Chia et al., 2016] Chia, C.-M., Huang, K.-Y., and Chang, E. (2016). Hough transform used on the spot-centroiding algorithm for the Shack-Hartmann wavefront sensor. *Optical Engineering*, 55(1):013105–013105.

[Climent and Hexsel, 2012] Climent, J. and Hexsel, R. A. (2012). Particle filtering in the Hough space for instrument tracking. *Computers in biology and medicine*, 42(5):614–623.

[Coffey, 2015] Coffey, V. C. (2015). Hyperspectral Imaging for Safety and Security. *Optics and Photonics News*, 26(10):26–33.

[Crabtree et al., 2004] Crabtree, K., Davis, J. A., and Moreno, I. (2004). Optical processing with vortex-producing lenses. *Applied Optics*, 43(6):1360–1367.

[Das, 2012] Das, P. K. (2012). *Optical signal processing: fundamentals*. Springer Science & Business Media.

[Davis et al., 2000] Davis, J. A., McNamara, D. E., Cottrell, D. M., and Campos, J. (2000). Image processing with the radial Hilbert transform: theory and experiments. *Optics Letters*, 25(2):99–101.

[Deans, 1981] Deans, S. R. (1981). Hough transform from the Radon transform. *IEEE Transactions on Pattern Analysis and Machine Intelligence*, (2):185–188.

[Dobson et al., 2016] Dobson, K. K., Jia, W., and Poon, T.-C. (2016). Anisotropic edge enhancement in optical scanning holography with spiral phase filtering. *Chinese Optics Letters*, 14(1):010006.

[Doskolovich et al., 2014] Doskolovich, L. L., Bykov, D. A., Bezus, E. A., and Soifer, V. A. (2014). Spatial differentiation of optical beams using phase-shifted Bragg grating. *Optics Letters*, 39(5):1278–1281.

[Downie, 1995] Downie, J. D. (1995). Nonlinear coherent optical image processing using logarithmic transmittance of bacteriorhodopsin films. *Applied Optics*, 34(23):5210–5217.

[Duda and Hart, 1972] Duda, R. O. and Hart, P. E. (1972). Use of the Hough transformation to detect lines and curves in pictures. *Communications of the ACM*, 15(1):11–15.

[Eguchi and Carlson, 1970] Eguchi, R. and Carlson, F. (1970). Linear vector operations in coherent optical data processing systems. *Applied Optics*, 9(3):687–694.

[Eichmann and Dong, 1983] Eichmann, G. and Dong, B. (1983). Coherent optical production of the Hough transform. *Applied Optics*, 22(6):830–834.

[Farber et al., 2013] Farber, V., August, Y., and Stern, A. (2013). Super-resolution compressive imaging with anamorphic optics. *Optics Express*, 21(22):25851–25863.

[Feng and Fainman, 1992] Feng, L. and Fainman, Y. (1992). Detection of a general ellipse by an optical Hough transform. *Applied Optics*, 31(17):3259–3262.

[Fernandes and Oliveira, 2008] Fernandes, L. A. and Oliveira, M. M. (2008). Real-time line detection through an improved Hough transform voting scheme. *Pattern Recognition*, 41(1):299–314.

[Fernández et al., 2011] Fernández, A., Alonso, J. R., Flores, J. L., Ayubi, G. A., Di Martino, J. M., and Ferrari, J. A. (2011). Optical processing of color images with incoherent illumination: orientation-selective edge enhancement using a modified liquid-crystal display. *Optics Express*, 19(21):21091–21097.

[Fernández, 2016a] Fernández, A. (2016a). Pattern recognition and feature extraction with an optical Hough transform. In *SPIE Optical Engineering + Applications*, pages 99700N–99700N. International Society for Optics and Photonics.

[Fernández, 2016b] Fernández, A. (2016b). Robust Pattern Recognition with Optical Generalized Hough Transform. In *Imaging Systems and Applications*, pages JTu3A–58. Optical Society of America.

[Fernández et al., 2015a] Fernández, A., Alonso, J. R., Ayubi, G. A., Osorio, M., and Ferrari, J. A. (2015a). Optical implementation of the generalized Hough transform with totally incoherent light. *Optics Letters*, 40(16):3901–3904.

[Fernández and Ferrari, 2015] Fernández, A. and Ferrari, J. (2015). Real-time Optical Realization of Circle Hough Transform with Incoherent Light. In *Frontiers in Optics*, pages JTu4A–57. Optical Society of America.

[Fernández et al., 2015b] Fernández, A., Flores, J. L., Alonso, J. R., and Ferrari, J. A. (2015b). Real-time pattern recognition using an optical generalized Hough transform. *Applied Optics*, 54(36):10586–10591.

[Fernández et al., 2016] Fernández, A., Flores, J. L., Alonso, J. R., and Ferrari, J. A. (2016). Image segmentation by nonlinear filtering of optical Hough transform. *Applied Optics*, 55(13):3632–3638.

[Flores et al., 2011] Flores, J. L., Ayubi, G. A., Alonso, J. R., Fernández, A., Di Martino, J. M., and Ferrari, J. A. (2011). Incoherent optical processor for nondirectional edge enhancement of color images. *Optics Letters*, 36(23):4596–4598.

[Flores et al., 2010] Flores, J. L., Ferrari, J. A., Ramos, J. A., Alonso, J. R., and Fernández, A. (2010). Analog image contouring using a twisted-nematic liquid-crystal display. *Optics Express*, 18(18):19163–19168.

[Fürhapter et al., 2005] Fürhapter, S., Jesacher, A., Bernet, S., and Ritsch-Marte, M. (2005). Spiral phase contrast imaging in microscopy. *Optics Express*, 13(3):689–694.

[Gindi and Gmitro, 1984] Gindi, G. R. and Gmitro, A. F. (1984). Optical feature extraction via the Radon transform. *Optical Engineering*, 23(5):235499–235499.

[Gonzalez and Woods, 2002] Gonzalez, R. C. and Woods, R. E. (2002). *Digital image processing*. Prentice Hall.

[Gonzalez et al., 2009] Gonzalez, R. C., Woods, R. E., and Eddins, S. L. (2009). *Digital image processing using MATLAB*. Pearson Prentice Hall.

[Goodman, 1985] Goodman, J. W. (1985). *Statistical optics*. John Wiley & Sons.

[Goodman, 1996] Goodman, J. W. (1996). *Introduction to Fourier optics*. Roberts and Company Publishers.

[Hart, 2009] Hart, P. E. (2009). How the Hough transform was invented. *IEEE Signal Processing Magazine*, 26(6):18–22.

[Hartley and Zisserman, 2003] Hartley, R. and Zisserman, A. (2003). *Multiple view geometry in computer vision*. Cambridge university press.

[Hendriks et al., 2005] Hendriks, C. L. L., Van Ginkel, M., Verbeek, P. W., and Van Vliet, L. J. (2005). The generalized radon transform: Sampling, accuracy and memory considerations. *Pattern Recognition*, 38(12):2494–2505.

[Herman, 2009] Herman, G. T. (2009). *Fundamentals of computerized tomography: image reconstruction from projections*. Springer Science & Business Media.

[Hollitt, 2013] Hollitt, C. (2013). A convolution approach to the circle Hough transform for arbitrary radius. *Machine vision and applications*, 24(4):683–694.

[Hough, 1962] Hough, P. V. (1962). Method and means for recognizing complex patterns. US Patent 3,069,654.

[Hueber et al., 2003] Hueber, E., Bigue, L., and Ambs, P. (2003). Active contour segmentation by use of a multichannel incoherent optical correlator. *Applied Optics*, 42(23):4681–4687.

[Hueber et al., 2001] Hueber, E., Bigué, L., Réfrégier, P., and Ambs, P. (2001). Optical snake-based segmentation processor with a shadow-casting incoherent correlator. *Optics Letters*, 26(23):1852–1854.

[Iizuka, 2008] Iizuka, K. (2008). *Engineering optics*, volume 35. Springer Science & Business Media.

[Illingworth and Kittler, 1988] Illingworth, J. and Kittler, J. (1988). A survey of the Hough transform. *Computer vision, graphics, and image processing*, 44(1):87–116.

[Ilovitsh et al., 2014] Ilovitsh, T., Ilovitsh, A., Sheridan, J., and Zalevsky, Z. (2014). Optical realization of the radon transform. *Optics Express*, 22(26):32301–32307.

[Jang and Shin, 1996] Jang, J.-S. and Shin, D.-H. (1996). Parallel optical-feature extraction by use of rotationally multiplexed holograms. *Optics Letters*, 21(19):1612–1614.

[Javadpour and Keating, 2000] Javadpour, Z. and Keating, J. G. (2000). Connectionist model of the generalized Hough transform for optical implementation. *Optical Engineering*, 39(6):1717–1722.

[Javidi, 2005] Javidi, B. (2005). *Optical and digital techniques for information security*, volume 1. Springer Science & Business Media.

[Jenkins and White, 1957] Jenkins, F. A. and White, H. E. (1957). *Fundamentals of optics*. Tata McGraw-Hill Education.

[Jesacher et al., 2005] Jesacher, A., Fürhapter, S., Bernet, S., and Ritsch-Marte, M. (2005). Shadow effects in spiral phase contrast microscopy. *Physical Review Letters*, 94(23):233902.

[Johnson, 2012] Johnson, S. (2012). Phase constrast microscopy. In *Biomedical optical phase microscopy and nanoscopy*, pages 3–17. Academic Press.

[Jose and Cubaud, 2012] Jose, B. M. and Cubaud, T. (2012). Droplet arrangement and coalescence in diverging/converging microchannels. *Microfluidics and nanofluidics*, 12(5):687–696.

[Kashter et al., 2012] Kashter, Y., Levi, O., and Stern, A. (2012). Optical compressive change and motion detection. *Applied Optics*, 51(13):2491–2496.

[Kelly, 1961] Kelly, D. (1961). Image-processing experiments. *JOSA*, 51(10):1095–1101.

[Kesidis and Papamarkos, 1999] Kesidis, A. L. and Papamarkos, N. (1999). On the inverse Hough transform. *IEEE Transactions on Pattern Analysis and Machine Intelligence*, 21(12):1329–1343.

[Knopp and Becker, 1978] Knopp, J. and Becker, M. F. (1978). Generalized model for noncoherent optical convolvers and correlators. *Applied Optics*, 17(7):984–985.

[Koppelhuber and Bimber, 2015] Koppelhuber, A. and Bimber, O. (2015). A classification sensor based on compressed optical Radon transform. *Optics Express*, 23(7):9397–9406.

[Kovasznay and Arman, 1957] Kovasznay, L. S. and Arman, A. (1957). Optical Autocorrelation Measurement of Two-Dimensional Random Patterns. *Review of Scientific Instruments*, 28(10):793–797.

[Kumar and Hassebrook, 1990] Kumar, B. V. and Hassebrook, L. (1990). Performance measures for correlation filters. *Applied Optics*, 29(20):2997–3006.

[Leavers, 1993] Leavers, V. (1993). Which hough transform? *CVGIP: Image understanding*, 58(2):250–264.

[Leith, 2000] Leith, E. N. (2000). The evolution of information optics. *IEEE Journal of Selected Topics in Quantum Electronics*, 6(6):1297–1304.

[Lipson, 2015] Lipson, M. (2015). Computing at the Speed of Light. In *Frontiers in Optics 2015*, page FM4A.4. Optical Society of America.

[Loce et al., 2013] Loce, R. P., Bernal, E. A., Wu, W., and Bala, R. (2013). Computer vision in roadway transportation systems: a survey. *Journal of Electronic Imaging*, 22(4):041121–041121.

[Lohmann, 1968] Lohmann, A. (1968). Matched filtering with self-luminous objects. *Applied Optics*, 7(3):561–563.

[Lohmann et al., 1996] Lohmann, A. W., Dorsch, R. G., Mendlovic, D., Ferreira, C., and Zalevsky, Z. (1996). Space–bandwidth product of optical signals and systems. *JOSA A*, 13(3):470–473.

[Lu et al., 2015] Lu, H., Zhao, K., You, Z., and Huang, K. (2015). Angle algorithm based on Hough transform for imaging polarization navigation sensor. *Optics Express*, 23(6):7248–7262.

[Lu and Tan, 2008] Lu, W. and Tan, J. (2008). Detection of incomplete ellipse in images with strong noise by iterative randomized Hough transform (IRHT). *Pattern Recognition*, 41(4):1268–1279.

[Mahajan, 2011] Mahajan, V. (2011). Optical Imaging and Aberrations, Part II. Wave Diffraction Optics. SPIE.

[Mahajan, 1998] Mahajan, V. N. (1998). *Optical Imaging and Aberrations, Part I. Ray Geometrical Optics*. SPIE.

[Mahajan and Díaz, 2016] Mahajan, V. N. and Díaz, J. A. (2016). Comparison of geometrical and diffraction imaging in the space and frequency domains. *Applied Optics*, 55(12):3241–3250.

[Maréchal and Croce, 1953] Maréchal, A. and Croce, P. (1953). Un filtre de fréquences spatiales pour lamélioration du contraste des images optiques. *Comptes rendus hebdomadaires des seances de l academie des sciences*, 237(12):607–609.

[Marr and Hildreth, 1980] Marr, D. and Hildreth, E. (1980). Theory of edge detection. *Proceedings of the Royal Society of London B: Biological Sciences*, 207(1167):187–217.

[Martinez-Carranza et al., 2015] Martinez-Carranza, J., Falaggis, K., and Kozacki, T. (2015). Multi-filter transport of intensity equation solver with equalized noise sensitivity. *Optics Express*, 23(18):23092–23107.

[Mazzaferri et al., 2010] Mazzaferri, J., Campos, J., Escalera, J. C., Sheppard, C. J., and Ledesma, S. (2010). Edge detector tolerant to object defocusing. *Optics Communications*, 283(19):3639–3645.

[Mazzaferri and Ledesma, 2007] Mazzaferri, J. and Ledesma, S. (2007). Rotation invariant real-time optical edge detector. *Optics Communications*, 272(2):367–376.

[Mazzaferri et al., 2003] Mazzaferri, J., Ledesma, S., and Iemmi, C. (2003). Multiple feature extraction by using simultaneous wavelet transforms. *Journal of Optics A: Pure and Applied Optics*, 5(4):425.

[McKenzie and Protheroe, 1990] McKenzie, D. and Protheroe, S. R. (1990). Curve description using the inverse Hough transform. *Pattern Recognition*, 23(3):283–290.

[McLachlan Jr, 1962] McLachlan Jr, D. (1962). The role of optics in applying correlation functions to pattern recognition. *JOSA*, 52(4):454–459.

[Mehta and Sheppard, 2009] Mehta, S. B. and Sheppard, C. J. (2009). Quantitative phase-gradient imaging at high resolution with asymmetric illumination-based differential phase contrast. *Optics Letters*, 34(13):1924–1926.

[Mendlovic and Ozaktas, 1993] Mendlovic, D. and Ozaktas, H. M. (1993). Fractional Fourier transforms and their optical implementation: I. *JOSA A*, 10(9):1875–1881.

[Merlin and Farber, 1975] Merlin, P. M. and Farber, D. J. (1975). A parallel mechanism for detecting curves in pictures. *IEEE Transactions on Computers*, (1):96–98.

[Mitiche and Ayed, 2010] Mitiche, A. and Ayed, I. B. (2010). *Variational and level set methods in image segmentation*, volume 5. Springer Science & Business Media.

[Monahan et al., 1977] Monahan, M. A., Bromley, K., and Bocker, R. P. (1977). Incoherent optical correlators. *Proceedings of the IEEE*, 65(1):121–129.

[Mori and Ohba, 1994] Mori, K. and Ohba, R. (1994). Optical Hough-transform processor with a two-dimensional array of computer-generated holograms. *Applied Optics*, 33(14):3111–3117.

[Morris and Zweig, 1987] Morris, G. M. and Zweig, D. A. (1987). White-light Fourier transformations. In *Optical Signal Processing*, pages 23–71. Academic, San Diego, Calif.

[Mukhopadhyay and Chaudhuri, 2015] Mukhopadhyay, P. and Chaudhuri, B. B. (2015). A survey of Hough Transform. *Pattern Recognition*, 48(3):993–1010.

[Nishimura et al., 1978] Nishimura, M., Casasent, D., and Caimi, F. (1978). Optical inverse Radon transform. *Optics Communications*, 24(3):276–280.

[Niu et al., 2015] Niu, J., Lu, J., Xu, M., Lv, P., and Zhao, X. (2015). Robust lane detection using two-stage feature extraction with curve fitting. *Pattern Recognition*.

[Nixon et al., 2012] Nixon, M., Nixon, M. S., and Aguado, A. S. (2012). *Feature extraction & image processing for computer vision*. Academic Press.

[O'Neill, 1956] O'Neill, E. (1956). Spatial filtering in optics. *IRE Transactions on Information Theory*, 2(2):56–65.

[Ozaktas and Mendlovic, 1993] Ozaktas, H. M. and Mendlovic, D. (1993). Fractional Fourier transforms and their optical implementation. II. *JOSA A*, 10(12):2522–2531.

[Pan et al., 2014] Pan, Y., Jia, W., Yu, J., Dobson, K., Zhou, C., Wang, Y., and Poon, T.-C. (2014). Edge extraction using a time-varying vortex beam in incoherent digital holography. *Optics Letters*, 39(14):4176–4179.

[Pe'er et al., 1999] Pe'er, A., Wang, D., Lohmann, A. W., and Friesem, A. A. (1999). Optical correlation with totally incoherent light. *Optics Letters*, 24(21):1469–1471.

[Qi et al., 2004] Qi, J., Shi, Z., Zhao, X., and Wang, Y. (2004). A novel fingerprint matching method based on the Hough transform without quantization of the Hough space. In *Third International Conference on Image and Graphics (ICIG'04)*, pages 262–265. IEEE.

[Radon, 1986] Radon, J. (1986). On the determination of functions from their integral values along certain manifolds. *IEEE Transactions on Medical Imaging*, 5(4):170–176.

[Rhodes and Sawchuk, 1981] Rhodes, W. and Sawchuk, A. (1981). Incoherent optical processing. In *Optical Information Processing*, pages 69–110. Springer.

[Ricca et al., 2015] Ricca, G., Beltrametti, M. C., and Massone, A. M. (2015). Piecewise recognition of bone skeleton profiles via an iterative Hough transform approach without re-voting. In *SPIE Medical Imaging*, pages 94132M–94132M. International Society for Optics and Photonics.

[Russ, 2011] Russ, J. C. (2011). *The image processing handbook*. CRC press.

[Schmid et al., 1998] Schmid, V. R., Bader, G., and Lueder, E. H. (1998). Shift-, rotation-, and scale-invariant shape recognition system using an optical Hough transform. In *Photonics West'98 Electronic Imaging*, pages 102–112. International Society for Optics and Photonics.

[Seth and Datta, 1996] Seth, M. and Datta, A. K. (1996). Optical implementation of a connectionist model of Hough transform. *Optical Engineering*, 35(6):1779–1784.

[Sheng et al., 1992] Sheng, Y., Roberge, D., and Szu, H. H. (1992). Optical wavelet transform. *Optical Engineering*, 31(9):1840–1845.

[Shih et al., 2001] Shih, M., Shishido, A., and Khoo, I. (2001). All-optical image processing by means of a photosensitive nonlinear liquid-crystal film: edge enhancement and image addition–subtraction. *Optics Letters*, 26(15):1140–1142.

[Shin and Jang, 1998] Shin, D.-H. and Jang, J.-S. (1998). Optical implementation of the Hough transform by use of rotationally multiplexed holograms. *Applied Optics*, 37(2):329–333.

[Shin and Jang, 2000] Shin, D.-H. and Jang, J.-S. (2000). Optical implementation of the generalized Hough transform by use of multiplexed holograms. *Optical Engineering*, 39(9):2431–2438.

[Shivakumar et al., 2005] Shivakumar, P., Kumar, G. H., Guru, D., and Nagabhushan, P. (2005). A new boundary growing and Hough Transform based approach for accurate skew detection in binary document images. In *Proceedings of 2005 International Conference on Intelligent Sensing and Information Processing, 2005.*, pages 140–146. IEEE.

[Situ et al., 2009] Situ, G., Pedrini, G., and Osten, W. (2009). Spiral phase filtering and orientation-selective edge detection/enhancement. *JOSA A*, 26(8):1788–1797.

[Sklansky, 1978] Sklansky, J. (1978). On the Hough technique for curve detection. *IEEE Transactions on computers*, (10):923–926.

[Sobel and Feldman, 1968] Sobel, I. and Feldman, G. (1968). A 3x3 isotropic gradient operator for image processing. *in a talk at the Stanford Artificial Project*, pages 271–272.

[Solli and Jalali, 2015] Solli, D. R. and Jalali, B. (2015). Analog optical computing. *Nature Photonics*, 9(11):704–706.

[Song and Lyu, 2005] Song, J. and Lyu, M. R. (2005). A hough transform based line recognition method utilizing both parameter space and image space. *Pattern recognition*, 38(4):539–552.

[Stark, 2012] Stark, H. (2012). *Application of optical Fourier transforms*. Elsevier.

[Steier and Shori, 1986] Steier, W. H. and Shori, R. K. (1986). Optical Hough transform. *Applied Optics*, 25(16):2734–2738.

[Stern, 2007] Stern, A. (2007). Compressed imaging system with linear sensors. *Optics Letters*, 32(21):3077–3079.

[Stoner, 1978] Stoner, W. (1978). Incoherent optical processing via spatially offset pupil masks. *Applied Optics*, 17(15):2454–2467.

[Tai and Chen, 2014] Tai, K.-C. and Chen, C.-H. (2014). Symbol Detection in Low-Resolution Images using a Novel Method. *International Journal of Control and Automation*, 7(12):143–154.

[Tajahuerce et al., 2005] Tajahuerce, E., Lancis, J., Andrés, P., Climent, V., and Javidi, B. (2005). Optoelectronic information encryption with incoherent light. In *Optical and Digital Techniques for Information Security*, pages 95–112. Springer.

[Tajahuerce et al., 2001] Tajahuerce, E., Lancis, J., Javidi, B., and Andrés, P. (2001). Optical security and encryption with totally incoherent light. *Optics Letters*, 26(10):678–680.

[Tanida and Ichioka, 1983] Tanida, J. and Ichioka, Y. (1983). Optical logic array processor using shadowgrams. *JOSA*, 73(6):800–809.

[Thoma et al., 1991] Thoma, R., Oesterhelt, D., Hampp, N., and Bräuchle, C. (1991). Bacteriorhodopsin films as spatial light modulators for nonlinear-optical filtering. *Optics Letters*, 16(9):651–653.

[Tian et al., 2014] Tian, L., Wang, J., and Waller, L. (2014). 3d differential phase-contrast microscopy with computational illumination using an LED array. *Optics Letters*, 39(5):1326–1329.

[Tomari et al., 2014] Tomari, R., Zakaria, W. N. W., Jamil, M. M. A., Nor, F. M., and Fuad, N. F. N. (2014). Computer aided system for red blood cell classification in blood smear image. *Procedia Computer Science*, 42:206–213.

[Trabka and Roetling, 1964] Trabka, E. A. and Roetling, P. G. (1964). Image transformations for pattern recognition using incoherent illumination and bipolar aperture masks. *JOSA*, 54(10):1242–1251.

[Trattner et al., 2014] Trattner, S., Kashdan, E., Feigin, M., and Sochen, N. (2014). Image formation of thick three-dimensional objects in differential-interference-contrast microscopy. *JOSA A*, 31(5):968–980.

[Tyo et al., 2006] Tyo, J. S., Goldstein, D. L., Chenault, D. B., and Shaw, J. A. (2006). Review of passive imaging polarimetry for remote sensing applications. *Applied Optics*, 45(22):5453–5469.

[Tyo et al., 1996] Tyo, J. S., Rowe, M., Pugh, E., and Engheta, N. (1996). Target detection in optically scattering media by polarization-difference imaging. *Applied Optics*, 35(11):1855–1870.

[Tyson, 2011] Tyson, R. K. (2011). *Principles of adaptive optics*. CRC press.

[Ujaldón et al., 2008] Ujaldón, M., Ruiz, A., and Guil, N. (2008). On the computation of the Circle Hough Transform by a GPU rasterizer. *Pattern Recognition Letters*, 29(3):309–318.

[Ulrich et al., 2003] Ulrich, M., Steger, C., and Baumgartner, A. (2003). Real-time object recognition using a modified generalized Hough transform. *Pattern Recognition*, 36(11):2557–2570.

[van den Braak et al., 2011] van den Braak, G.-J., Nugteren, C., Mesman, B., and Corporaal, H. (2011). Fast hough transform on GPUs: Exploration of algorithm trade-offs. In *Advanced Concepts for Intelligent Vision Systems*, pages 611–622. Springer.

[van der Lugt, 1964] van der Lugt, A. (1964). Signal detection by complex spatial filtering. *IEEE Transactions on Information Theory*, 10(2):139–145.

[Wang et al., 2009] Wang, Y., Shi, M., and Wu, T. (2009). A method of fast and robust for traffic sign recognition. In *Fifth International Conference on Image and Graphics, 2009. ICIG'09.*, pages 891–895. IEEE.

[Weaver and Goodman, 1966] Weaver, C. and Goodman, J. W. (1966). A technique for optically convolving two functions. *Applied Optics*, 5(7):1248–1249.

[Yang et al., 2016] Yang, H., Zheng, S., Lu, J., and Yin, Z. (2016). Polygon-invariant generalized hough transform for high-speed vision-based positioning. *IEEE Transactions on Automation Science and Engineering*, 13(3):1367–1384.

[Yelleswarapu et al., 2006] Yelleswarapu, C., Wu, P., Kothapalli, S.-R., Rao, D., Kimball, B., Sai, S., Gowrishankar, R., and Sivaramakrishnan, S. (2006). All-optical spatial filtering with power limiting materials. *Optics Express*, 14(4):1451–1457.

[Youssefi et al., 2016] Youssefi, A., Zangeneh-Nejad, F., Abdollahramezani, S., and Khavasi, A. (2016). Analog computing by Brewster effect. *Optics Letters*, 41(15):3467–3470.

[Yu, 1987] Yu, F. T. (1987). Color image processing. In *Optical signal processing*, pages 3–22. Elsevier.

[Zhong et al., 2014] Zhong, Z., Gao, P., Shan, M., Wang, Y., and Zhang, Y. (2014). Real-time image edge enhancement with a spiral phase filter and graphic processing unit. *Applied Optics*, 53(19):4297–4300.

[Zhou et al., 2014] Zhou, X., Ito, Y., and Nakano, K. (2014). An Efficient Implementation of the One-Dimensional Hough Transform Algorithm for Circle Detection on the FPGA. In *Computing and Networking (CANDAR), 2014 Second International Symposium on*, pages 447–452. IEEE.

[Zuo et al., 2015] Zuo, C., Sun, J., Zhang, J., Hu, Y., and Chen, Q. (2015). Lensless phase microscopy and diffraction tomography with multi-angle and multi-wavelength illuminations using a LED matrix. *Optics Express*, 23(11):14314–14328.